



HAL
open science

A sterol-PI(4)P exchanger modulates the Tel1/ATM axis of the DNA damage response

Sara Ovejero, Sylvain Kumanski, Caroline Soulet, Julie Azarli, Benjamin Pardo, Olivier Santt, Angelos Constantinou, Philippe Pasero, María Moriel-Carretero

► To cite this version:

Sara Ovejero, Sylvain Kumanski, Caroline Soulet, Julie Azarli, Benjamin Pardo, et al.. A sterol-PI(4)P exchanger modulates the Tel1/ATM axis of the DNA damage response. *EMBO Journal*, 2023, 10.15252/embj.2022112684 . hal-04135707

HAL Id: hal-04135707

<https://hal.science/hal-04135707>

Submitted on 21 Jun 2023






HAL is a multi-disciplinary open access archive for the deposit and dissemination of scientific research documents, whether they are published or not. The documents may come from teaching and research institutions in France or abroad, or from public or private research centers.

L'archive ouverte pluridisciplinaire **HAL**, est destinée au dépôt et à la diffusion de documents scientifiques de niveau recherche, publiés ou non, émanant des établissements d'enseignement et de recherche français ou étrangers, des laboratoires publics ou privés.



Distributed under a Creative Commons Attribution - NonCommercial - NoDerivatives 4.0 International License

A sterol-PI(4)P exchanger modulates the Tel1/ATM axis of the DNA damage response

Sara Ovejero^{1,2,†}, Sylvain Kumanski^{3,†}, Caroline Soulet³, Julie Azarli³, Benjamin Pardo¹ ,
Olivier Santt³ , Angelos Constantinou¹ , Philippe Pasero¹  & María Moriel-Carretero^{3,*} 

Abstract

Upon DNA damage, cells activate the DNA damage response (DDR) to coordinate proliferation and DNA repair. Dietary, metabolic, and environmental inputs are emerging as modulators of how DNA surveillance and repair take place. Lipids hold potential to convey these cues, although little is known about how. We observed that lipid droplet (LD) number specifically increased in response to DNA breaks. Using *Saccharomyces cerevisiae* and cultured human cells, we show that the selective storage of sterols into these LD concomitantly stabilizes phosphatidylinositol-4-phosphate (PI(4)P) at the Golgi, where it binds the DDR kinase ATM. In turn, this titration attenuates the initial nuclear ATM-driven response to DNA breaks, thus allowing processive repair. Furthermore, manipulating this loop impacts the kinetics of DNA damage signaling and repair in a predictable manner. Thus, our findings have major implications for tackling genetic instability pathologies through dietary and pharmacological interventions.

Keywords lipid droplets; OSBP1; PI(4)P; sterols; Tel1/ATM

Subject Categories DNA Replication, Recombination & Repair; Membranes & Trafficking

DOI 10.15252/emboj.2022112684 | Received 26 September 2022 | Revised 15 May 2023 | Accepted 26 May 2023

The EMBO Journal (2023) e112684

Introduction

The integrity of the genetic information needs to be preserved to warrant cell and organism fitness. The cell therefore possesses surveillance and repair strategies to accomplish this task. Cells challenged with DNA damage or other sources of genotoxic stress activate the DNA damage response (DDR) to arrest the cell cycle for DNA repair to take place. This occurs upon lesion detection by dedicated sensors, which engage the upstream kinases of this response, namely Tel1/ATM (as known in *Saccharomyces cerevisiae* and humans, respectively) and Mec1/ATR. Kinase activity promotes effector phosphorylation, among which Rad53/CHK1-CHK2, which in turn drive cell

protection and recruit repair factors. Successful repair coupled to subsequent checkpoint inactivation is named recovery. However, if the damage cannot be repaired, different scenarios may emerge: cells can remain in a permanent cell cycle arrest, which, from a developmental point of view, compromises future lineages. Alternatively, an exacerbated activation of the DDR triggers apoptosis, leading to cell death and tissue loss in many degenerative diseases (Kruman *et al*, 2004; Tomashevski *et al*, 2010). Last, cells could resume cycling in the presence of the damage. This latter phenomenon is called adaptation and permits cell survival while propagating genome instability. Adaptation is achieved by downregulation of the DDR and is reported as a cell survival strategy under chronic DNA damage conditions in unicellular organisms (Pelliccioli *et al*, 2001; Clémenson & Marsolier-Kergoat, 2009). In multicellular organisms, adaptation is generally prevented through the engagement of apoptosis or senescence, which limit unrestrained proliferation (Halazonetis *et al*, 2008). Overall, the intensity and the context of the DDR activation dictates repair, apoptosis, or uncontrolled proliferation.

Another important aspect ruling cell fate relies on lipids. This is clearly illustrated during cancer development, in which lipids act as energy sources and signaling nodes, promoting progression and even metastasis (Currie *et al*, 2013; Pascual *et al*, 2017). Saturated fatty acids also make cells less permeable to exogenous toxins, oxidative damage, and chemotherapeutic agents (Röhrig & Schulze, 2016). A specific player in the metabolism of lipids is lipid droplets (LD), the sole organelle to be delimited by a monolayer of phospholipids. LD are classically known as the cell storage for fats and were long seen as a static, almost inert bag of lipids. They are mainly filled with apolar lipids such as esterified fatty acids in the form of triacylglycerols (TAGs) and esterified sterols in the shape of steryl esters (STEs). They are born from the endoplasmic reticulum (ER) into the cytoplasm, where their half-life is regulated by an intricate interplay of esterifying enzymes, LD-ER contact factors, and lipases (Beller *et al*, 2010). Their relevance is illustrated by the wide spectrum of diseases that derive from their mishandling (Krahmer *et al*, 2013). Yet, even if in cancer the presence of LD is a hallmark of bad prognosis, relapse, and resistance to chemotherapy (Yue *et al*, 2014; de Gonzalo-Calvo *et al*, 2015; Qiu *et al*, 2015), the specific relevance of LD in cell fate decisions is less understood. Last, a

1 Institut de Génétique Humaine (IGH), Université de Montpellier-Centre National de la Recherche Scientifique, Montpellier Cedex 5, France

2 Department of Biological Haematology, CHU Montpellier, Montpellier Cedex 5, France

3 Centre de Recherche en Biologie cellulaire de Montpellier (CRBM), Université de Montpellier-Centre National de la Recherche Scientifique, Montpellier Cedex 5, France

*Corresponding author. Tel: +33 434359564; E-mail: maria.moriel@crbm.cnrs.fr

†These authors contributed equally to this work

further important aspect of lipid regulation occurs at membrane contact sites. These are locations where membranes from two (or more) different organelles approach, being no longer than 80 nm apart, and where specific protein machines execute the transfer of lipids from one membrane to another, creating fluxes of functional importance (Lahiri *et al*, 2015). Among them, the interface between the trans-Golgi and the ER hosts the OSBP1 exchanger: sterol moieties present in the ER are extracted from this location and inserted in the trans-Golgi in exchange of phosphatidylinositol-4-phosphate (PI(4)P) molecules, which are in turn extracted from the Golgi and inserted in the ER. Once in the ER, these PI(4)P molecules are fast hydrolyzed by the phosphatase SAC1, which boosts this way the activity of this lipid exchange machinery (Antonny *et al*, 2018). Thus, the low sterol content of the ER is warranted by the fine regulation of the activity of OSBP1.

Observations from the last 10 years suggest links between nutrient sensing, lipid programs, and DNA damage handling (Zeng *et al*, 2008; Klermund *et al*, 2014; Ahmad *et al*, 2017; Edifizi *et al*, 2017; Ferrari *et al*, 2017; Moriel-Carretero, 2021), yet a deep mechanistic understanding is still missing. In this work, we explore whether the response of the cell to DNA damage can be modulated by the metabolism of lipids. We found that human ATM and *S. cerevisiae* Tel1, upstream kinases of the DDR and ancestral phosphatidylinositol kinases (Hunter, 1995), can bind PI(4)P. In response to DSBs, the formation of LD that specifically store sterols is promoted, thus decreasing sterol levels at the ER. In turn, this limits the extraction of PI(4)P from the Golgi. The PI(4)P moieties stabilized this way keep ATM/Tel1 locked away from the nucleus, a titration that is key to permit efficient DNA repair. Last, we provide proof-of-concept that the manipulation of sterol metabolism at the interface between the trans-Golgi and the ER permits an unanticipated modulation of ATM/Tel1, for example, in the dampening of the DDR. Our data support the existence of an evolutionarily conserved mechanism whose control in response to DSBs can be tailored genetically and pharmacologically by manipulating the metabolism of lipids, thus bearing an exciting potential both in basic and applied research on genome stability.

Results

Lipid droplets accumulate in response to DNA double-strand breaks

To determine whether genotoxic stress impacts the accumulation of LD in cells, we performed kinetic studies by exposing asynchronous cultures of wild-type (WT) *Saccharomyces cerevisiae* cells to genotoxic agents that induce DNA breakage (Fig 1A–C). We used zeocin, a radiomimetic agent that creates DNA single-stranded and double-stranded DNA breaks (DSBs) and camptothecin (CPT), which covalently traps topoisomerase-I to DNA and leads to the accumulation of DSBs during DNA replication. DSB induction with zeocin or CPT triggered an increase of Rad52 foci formation, which promotes DSB repair by homologous recombination (HR; Appendix Fig S1A and B; Lisby *et al*, 2001). The presence of DSBs is expected to activate the DNA damage response (DDR), which drives the accumulation of cells in the G₂ phase of the cell cycle (2C DNA content in Fig 1B and C; Weinert & Hartwell, 1988). We then monitored the presence of

LD using the vital dye Nile Red and observed that these agents triggered a significant increase of LD in the cell population (Fig 1A–C) in a reproducible manner (Fig 1F). We also exposed the cells to the genotoxic agent hydroxyurea (HU), which does not induce DSBs but blocks DNA replication by decreasing dNTP pools. Short time exposure to HU blocks cells in S phase (Fig 1D, right) and activates the DDR, but does not lead to the formation of Rad52 foci (Appendix Fig S1B; Alabert *et al*, 2009). In response to HU, LD did not accumulate in a significant manner (Fig 1D, left and F), suggesting that they specifically accumulate in response to DSBs. We excluded that LD increase related to cells accumulation in G₂, because treatment with nocodazole, which forces G₂/M cell arrest (Fig 1E, right) due to microtubule depolymerization without creating DNA damage, failed to induce LD accumulation to the same extent (Fig 1E, left and F). To rule out the possibility that LD accumulation stems from a collateral effect of the genotoxins, we took advantage of a CRISPR-Cas9-based system targeting 59 genomic positions thanks to one guide RNA directed against transposon sequences (preprint: Coiffard *et al*, 2021). In this system, we express Cas9 from a galactose-inducible promoter. To ensure subsequent robust induction of Cas9 expression, cells were grown either in glycerol medium (Fig 1H, experiment 1) or in raffinose medium (Fig 1I and J, experiments 2 & 3), in which basal levels of LD in the cell differ. Irrespective of LD basal levels in the noninduced condition, galactose addition repetitively raised LD levels in a time-dependent manner (Fig 1G–J). This was not a galactose-associated effect, as the same medium change in cells which do not possess any targeting gRNA did not increase LD numbers (Fig 1K). We therefore conclude that LD formation is stimulated in the event of DSBs.

Inability to esterify sterols exacerbates DNA double-strand break signaling

To assess whether the accumulation of LD in response to DSBs was of functional relevance and to ascertain which type of LD contents could be implicated, we explored the sensitivity to DSB-making agents of cells in which the storage of different LD constituents was compromised. LD store two different types of apolar lipids, namely triacylglycerol (TAGs) and steryl esters (STEs), deriving from the esterification of fatty acids and sterols, respectively (Beller *et al*, 2010). We used isogenic strains lacking TAGs (*tro1Δ dga1Δ*, designated *tagΔ* hereafter) or STEs (*are1Δ are2Δ*, designated *steΔ* hereafter; Shpilka *et al*, 2015). As expected, *tagΔ* and *steΔ* cells have a low basal level of LD (Appendix Fig S1C), (Shpilka *et al*, 2015). We observed that only *steΔ* cells were more sensitive to zeocin and CPT than WT cells, yet not to HU (Fig 2A). This suggests that only the esterification of sterols into steryl esters then their storage in LD is important to cope with the induction of DSBs.

To gain understanding about the role of STEs in DSB tolerance, we first monitored the progressive phosphorylation of the DDR effector kinase Rad53 upon zeocin treatment as a readout of the DDR activation. *steΔ* cells displayed a modestly faster phosphorylation of Rad53 compared with *tagΔ* and WT cells (Fig 2B), which was unrelated to changes in cell cycle distribution (Appendix Fig S1D). This phenotype was specific to the DSB-inducing agent zeocin, as HU treatment did not accelerate the pattern of phosphorylation of Rad53 in *steΔ* cells (Fig EV1A). To independently validate that this was related to the inability of the cells to esterify sterols, we repeated the

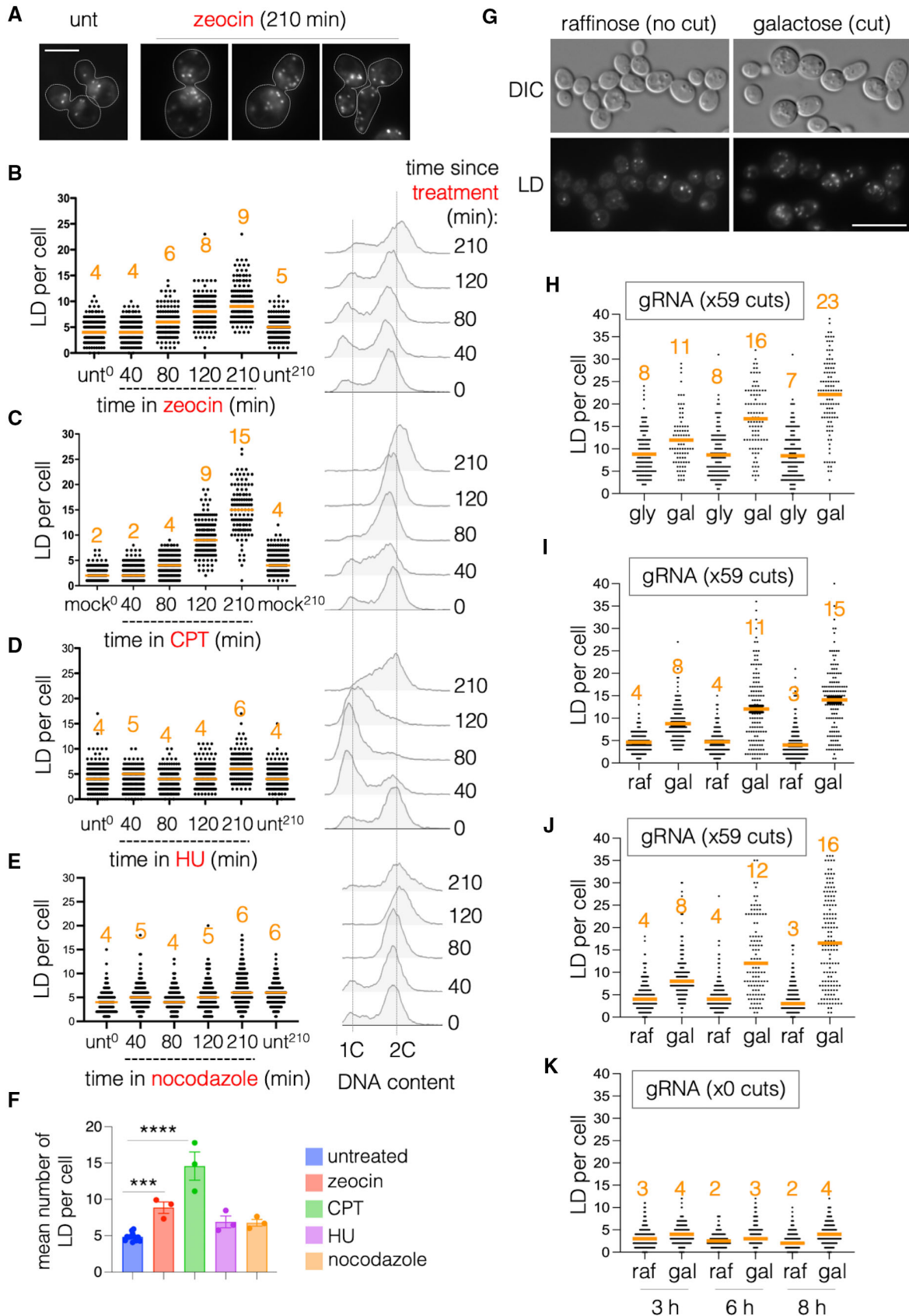


Figure 1.

Figure 1. DNA double-strand breaks induce lipid droplet accumulation.

- A *S. cerevisiae* cells growing exponentially were treated (or not) with 100 µg/ml zeocin for the indicated times and stained using the vital dye Nile Red just prior to imaging to visualize LD. Scale bar is 6 µm.
- B–E **Left:** At least 150 cells were counted per time point and the number of LD per cell was inspected visually and plotted. The median value of each time point is indicated by an orange bar and number. Each panel corresponds to a representative time-course experiment in response to each indicated DNA-damaging agent (out of at least 3 per agent). “unt” = untreated condition. “mock” refers to the culture being treated with DMSO, the dissolving agent for CPT. The used concentrations were 100 µg/ml zeocin, 100 µM CPT, 100 mM HU, and 15 µg/ml nocodazole. **Right:** the same cultures were analyzed by cytometry to assess DNA content (1C = unreplicated DNA, 2C = fully replicated DNA) during the time course to confirm that the used agents were causing cell arrest at the expected phases of the cell cycle.
- F The mean value of LD per cell at time 210 min of treatment (or associated untreated controls) as counted from each of the independent experiments done to build Fig 1B–E as well as their replicates were plotted as individual dots. The bar height is the mean of those means and the error bars correspond to the Standard Error of the Mean (SEM). A statistical analysis of the potential difference among the means of the means was derived by unpaired one-way ANOVA. Only significant differences are displayed: *** $P < 0.001$; **** $P < 0.0001$.
- G *Saccharomyces cerevisiae* cells harboring a galactose-inducible gRNA-expressing plasmid capable of driving 59 cuts in the genome were grown exponentially in rich medium with raffinose as the carbon source (left, no cut expected) or upon addition of 2% galactose for 8 h (right, cuts expected) then stained using the vital dye Nile Red prior to imaging to visualize LD. Scale bar is 8 µm.
- H–K Cells as described in (G) in which the noninduced condition varied between glycerol (H) or raffinose (I–K), and the cells harbored either a plasmid driving 59 cuts in the genome (H–J) or none (K).

experiment in cells preloaded with oleate, because this unsaturated fatty acid is firmly characterized to directly inhibit sterol esterification in *S. cerevisiae* (Connerth *et al*, 2010) and outcompetes esterified sterol storage in cultured human cells (Rohwedder *et al*, 2014; Nakajima *et al*, 2019). Addition of oleate readily filled LD (Appendix Fig S1C). Cells preloaded with oleate also showed a faster Rad53 phosphorylation compared with mock-treated cells (Fig 2C) in the absence of any apparent cell cycle alteration that could explain this difference (Appendix Fig S1D), or any alterations in total Rad53 protein levels due to oleate load (Appendix Fig S2A).

We also explored whether this phenomenon was observable in two different human cell lines, RPE-1 (hTERT-immortalized cells from retinal pigmented epithelium of nontumoral origin) and Huh-7 (derived from hepatocarcinoma). We induced DSBs with zeocin or the DNA alkylating agent methyl methanesulfonate (MMS; Appendix Fig S2B, upper panels). As a readout for the DDR activation, we monitored the phosphorylation on Thr68 of the downstream effector CHK2. As expected, incubation of RPE-1 and Huh-7 cells with MMS or zeocin led to the phosphorylation of CHK2, while total CHK2 levels remained constant (Fig 2D). Pretreatment of both RPE-1 and Huh-7 cells with oleate to prevent sterol esterification within LD led to an increased amount of TAG-containing LD (Appendix Fig S2C). We observed a stronger P-CHK2 signal in oleate preloaded cells compared with mock-treated cells in response to both MMS (Fig 2D, more variable) and zeocin (Fig 2D, more robust), suggesting a stronger DDR activation. Moreover, specific inhibition of sterol esterification using the drug avasimibe (Appendix Fig S2D) also led to an increased DDR (Fig 2E). It was relevant that the same exacerbation in the activation of the other downstream DDR effector, namely CHK1, was not observed when scoring its phosphorylation either on serine 317 or 345 (Fig EV1B). Importantly, these phenomena were again unlikely related to cells being in different cell cycle stages, since the short duration of the treatments did not trigger major differences in cell cycle distribution (Fig EV1C). Last, in Huh-7 cells, in which zeocin delayed proliferation without abolishing it, preincubation with oleate further sensitized them to zeocin (Fig EV1D, right panel).

Altogether, our results show that the inability to esterify sterols and subsequently store STEs in LD leads to an accelerated or exacerbated activation of the response to DSBs in both *S. cerevisiae* and human cells, which consequently impacts cell proliferation.

Lack of sterol esterification inhibits long-range resection, compromising downstream DSB repair

The esterification of sterols is the consequence of removing free sterols from their previous location, the membrane. To evaluate whether removal of free sterols from membranes was important to control the activation kinetics of the DDR, we used a mutant strain of *S. cerevisiae* deficient for the protein Yeh2 (Müllner *et al*, 2005). Yeh2 is a steryl ester lipase located at the plasma membrane. Its active site being oriented toward the extracellular space, thus with no access to the intracellular pool of esterified sterols, it is purported to replenish the free sterol pool of the plasma membrane by hydrolyzing extracellular steryl esters (Köffel *et al*, 2005). In this context, the incapability for maintaining the pool of free sterols at the plasma membrane forces intracellular pools of steryl esters to be hydrolyzed, and the released steryl moieties transported from the lipid droplets and the endoplasmic reticulum to the plasma membrane (Leber *et al*, 1995). In agreement, we quantified that *yeh2Δ* cells display less LD per cell than a WT under basal conditions (Appendix Fig S2E). As this phenocopies the inability to esterify and store sterols within LD of the *steΔ* strain, we monitored the activation kinetics of the DDR in response to zeocin in isogenic WT and *yeh2Δ* cells and found that, similar to lack of sterol esterification (Fig 2B and C), Rad53 became phosphorylated more rapidly in the absence of Yeh2 (Fig 3A; Garcia *et al*, 2022) in a cell cycle-unrelated manner (Fig EV2A). Again, this was related to DSBs, since the kinetics of Rad53 phosphorylation in response to HU was not accelerated in *yeh2Δ* cells with respect to the WT (Fig EV2B). Moreover, and as for *steΔ* cells, *yeh2Δ* cells were hypersensitive to zeocin (Fig 3B). Thus, sterol removal from membranes and their subsequent esterification and storage within LD tone down the speed and intensity of the DDR activation upon DSBs.

We next hypothesized that this exacerbated DDR was indicative of alterations somewhere in the cascade ranging from DSB detection to downstream DNA repair. We set to study different steps from the signaling to the repair events occurring in response to a DSB (Fig EV2C; Gobbini *et al*, 2013). We first monitored the resection of DSB ends, an early event of DSB processing required for repair by HR. DSB end resection consists of the degradation of the 5' DNA strand, generating 3' single-stranded DNA (ssDNA) tails. These

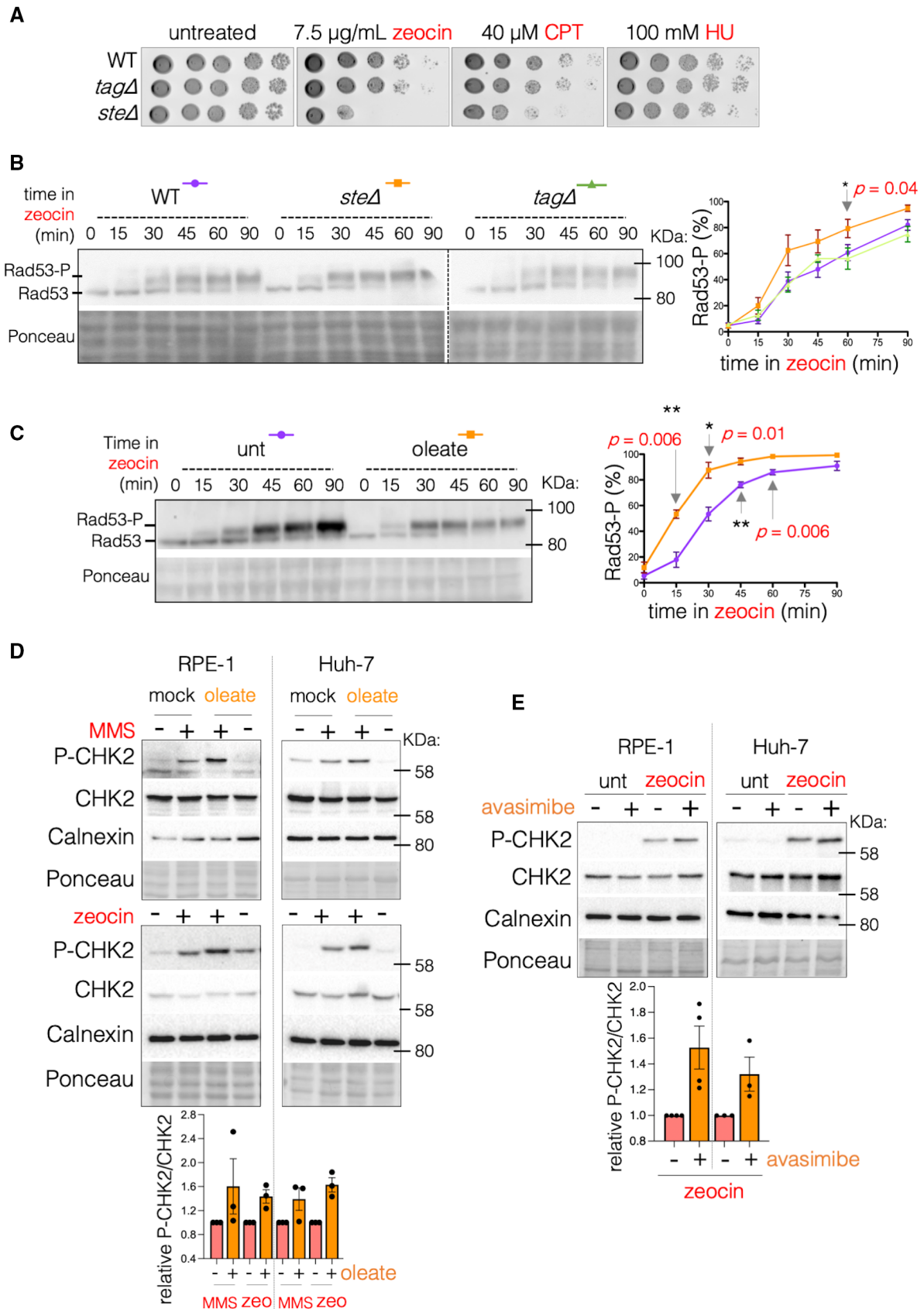


Figure 2.

Figure 2. Lack of sterol storage or esterification exacerbates the DDR.

- A Sensitivity of *S. cerevisiae* WT, *steΔ* and *tagΔ* cells to the indicated genotoxic agents as assayed by 10-fold serial dilutions of exponentially growing cultures spotted onto YPD plates supplemented with the indicated agents. Plates were incubated at 30°C from 2 to 5 days.
- B Exponentially growing *S. cerevisiae* WT, *steΔ* and *tagΔ* cells were treated with 100 μg/ml zeocin and samples collected at the indicated time points for western blot analysis and cytometry (Appendix Fig S1D). The activation of the DDR was monitored following the progressive phosphorylation of its downstream effector kinase Rad53. The unphosphorylated and phosphorylated isoforms of Rad53 are indicated (Rad53 and Rad53-P, respectively). Ponceau staining is shown as a loading control. The percentage of Rad53-P was quantified at each point by dividing the raw signal of the upper band by the total signal in that lane, thus plotted in the graph shown on the right. The plotted values represent the mean value of at least 3 independent experiments and the variation is represented by the SEM. Unpaired t-tests were used to compare the potential differences of the means at each time point. Only the P-value(s) for those being significantly different are indicated.
- C Identical to (B) but comparing unloaded WT and WT preloaded for 2 h with 0.05% oleate in order to inhibit sterol esterification.
- D Nonconfluent RPE-1 and Huh-7 human cell lines were either left untreated or treated for 2 h with the DNA-damaging agents MMS (0.005%) or zeocin (10 μg/ml). Prior to that, cells were preloaded with oleate (4 h at 60 μM) to inhibit sterol esterification or treated with 30 μM BSA (mock) as a control. The downstream effector kinase of the DDR CHK2 was monitored by western blot for its activation using a specific antibody against its phosphorylation at Thr68 (P-CHK2). The western blot signal for total CHK2, calnexin and the Ponceau staining are used as loading controls. The bars in the graph show the mean value of the P-CHK2 to CHK2 signals ratio for genotoxins-treated cells while the dots correspond to the individual values out of 3 independent experiments.
- E Identical to (D) though only in response to zeocin and by inhibiting sterols with the specific inhibitor avasimibe (5 μM for 2 h). Plot details as in (D).

structures are covered by the ssDNA-binding heterotrimeric complex RPA, conformed by Rfa1-Rfa2-Rfa3 in *S. cerevisiae*, which forms nuclear foci (Lisby *et al*, 2004; Ivanova *et al*, 2020; Ramonaxo & Moriel-Carretero, 2021). WT cells displayed less than one CFP-tagged Rfa1 focus per cell (0.42, mean value) basally. Foci number per cell progressively increased during exposure to zeocin, having tripled at 210 min after treatment onset (1.56, Figs 3C and EV2D). In contrast, zeocin treatment increased by more than 10-fold the mean number of Rfa1 foci in *steΔ* cells (2.33 versus 0.2, Figs 3C and EV2D). In the same line, Rad52, the homology search factor that replaces RPA onto the resected filament, greatly accumulated in the form of foci in *steΔ* cells in response to zeocin (Fig EV2E). These results suggest that cells unable to remove sterols from membranes either accumulate longer ssDNA tracts or, on the contrary, accumulate unproductive events because they are unable to implement processive resection. To discern between these two possibilities, we monitored DSB end resection at the molecular level using a genetically engineered strain in which one single DSB can be induced by the controlled expression of the HO endonuclease (Lee *et al*, 2000). We observed DSBs after 30 min of HO induction. Resection products, detected by the progressive disappearance of restriction sites close to DSB ends (Fig EV2F), started to accumulate shortly after (Fig 3D). Importantly, *yeh2Δ* cells displayed a decrease in long resection tracks at late time points (Fig 3D, 15.8 kb product). We interpret that this modest defect stems from the fact that only one DSB is being induced in this experiment, in contrast to the greater RPA accumulation seen upon zeocin treatment (Figs 3C and EV2D). We also treated human RPE-1 cells with MMS and physically monitored ssDNA by extracting genomic DNA, spotting it on a membrane, and blotting it with an anti-ssDNA antibody. This way, we detected a progressive accumulation of ssDNA upon MMS addition (Fig 3E). Preloading cells with oleate to prevent sterol esterification led to less ssDNA accumulation in response to MMS (Fig 3E). Overall, data point toward a defect in implementing long-range resection in response to DSBs if sterols cannot be removed from membranes or esterified.

If long-range resection is compromised when sterols remain within membranes, thus, the efficiency of downstream DNA repair by HR is expected to decrease. We assessed this possibility using a genetic system in which the number of HR repair products, mostly single-strand annealing reactions (dependent on Rad52 upon DSB formation), can be measured. The system, integrated in the genome of *S. cerevisiae*, consists of two directly repeated sequences of a

leu2-k allele that flank one *ADE2* and one *URA3* copy. Whenever a break occurs in between the two *leu2-k* sequences, the recombination process between the two direct repeats will end up with the loss of the intermediate sequences. Cells having lost the intervening *URA3* marker in such a process can be selected in plates containing 5-fluoroorotic acid (5-FOA, for the presence of the enzyme encoded by *URA3* will convert 5-FOA to the toxic compound 5-fluorouracil), and thus, the frequency of recombinants calculated (Aguilera & Klein, 1990). When WT cells were exposed to zeocin, the induction of DSBs led to an expected increase in the frequency of recombination of up to 15-fold (Fig 4A). Importantly, preventing the esterification of sterols either genetically (*steΔ*) or pharmacologically (with oleate) limited the formation of recombination products up to threefold (Fig 4A). Likewise, recombination was induced sevenfold in the DSB-prone mutant *rad3-102* (Moriel-Carretero & Aguilera, 2010), but the additional *steΔ* mutation restricted this increase to less than twofold (Fig 4B). Thus, the decrease in the frequency of HR products suggests that impairment in sterol esterification is hampering DSB repair. To validate this hypothesis in yet another system, we monitored the accumulation of zeocin-induced DSB in RPE-1 and Huh-7 cells using pulsed-field gel electrophoresis (PFGE). In both cell types, zeocin led to a prominent and similar accumulation of in-gel (i.e., broken) molecules (Fig 4C and D total in-gel molecules and bottom quantifications). Yet, when sterol esterification was inhibited by oleate, the intensity of the shorter fragments increased (Fig 4C and D, lateral orange vs pink curves). To gain a more kinetic insight supporting this view, we monitored break formation and repair at the single-cell level using comet assays (Fig 4E). Three independent experiments showed a robust induction of breaks upon zeocin treatment for 1 h and then progressive repair in the 4 h following zeocin withdrawal from the medium (Fig 4F, mock panel), with a repair kinetics slope of -6.275 ± -0.57 (Fig 4F, right). Probably due to variations in the efficiency of oleate loading in the population, the variability associated with the same three experiments in cells preloaded with oleate was higher (Fig 4F, oleate panel). Still, while damage induction occurred comparably to mock conditions, the repair kinetics upon zeocin removal was either delayed (Fig 4F, oleate, violet and blue points) or stalled (Fig 4F, oleate, orange points), with a smaller repair kinetics slope than in the mock condition (-4.362 ± -0.99 , Fig 4F, right). Taken together, results confirm that, while the same number of lesions is induced, repair is less efficient in oleate-treated cells.

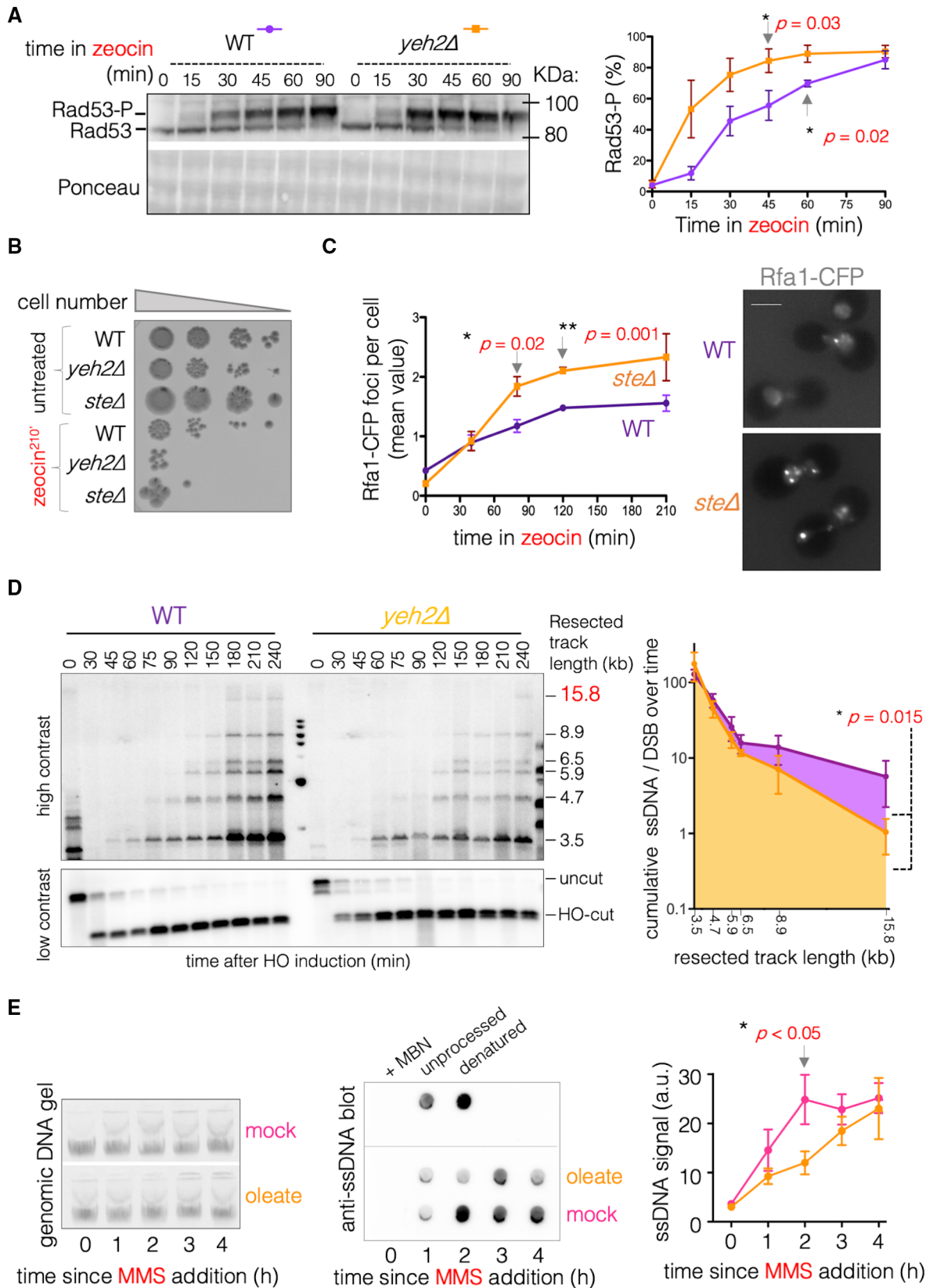


Figure 3.

Figure 3. Impairment in sterol esterification blocks processive (long-range) resection.

- A Exponentially growing *Saccharomyces cerevisiae* WT and *yeh2Δ* cells were treated with 100 μg/ml zeocin and samples retrieved at the indicated time points for western blot analysis and cytometry (see Fig EV2A). The activation of the DDR was monitored following the progressive phosphorylation of its downstream effector kinase Rad53. The unphosphorylated and phosphorylated isoforms of Rad53 are indicated (Rad53 and Rad53-P, respectively). Ponceau staining is shown as a loading control. The percentage of Rad53-P was quantified at each time point and plotted in the graph shown on the right. The plotted values represent the mean value of at least 3 independent experiments and the variation is represented as the SEM. Unpaired *t*-tests were used to compare the potential differences of the means at each time point. Only the *P*-value(s) for those being significantly different are indicated.
- B Sensitivity of *S. cerevisiae* WT, *yeh2Δ* and *steΔ* cells to zeocin as assayed by 10-fold serial dilutions growth assays. Exponentially YPD-growing cultures were split in two and either treated with 100 μg/ml zeocin for 210 min or not, washed if treated, and then seeded onto nonsupplemented YPD plates. Plates were incubated at 30°C from 2 to 5 days.
- C Exponentially growing *S. cerevisiae* WT and *steΔ* cells were treated with 100 μg/ml zeocin and samples retrieved at the indicated time points for inspection by fluorescence microscopy. The establishment of DNA resection factories was assessed by counting the number of Rfa1-CFP foci per cell. Scale bar is 4 μm. Left: the mean values of each time point (as calculated in Fig EV2D) of three independent experiments were used to obtain this graph (mean and SEM). Unpaired *t*-tests were used to compare the potential differences of the means at each time point. Only the *P*-value(s) for those being significantly different are indicated. Right: representative images of both strains at time point 120 min. Scale bar is 4 μm.
- D WT and *yeh2Δ* cells carrying a plasmid bearing the HO nuclease gene under a galactose-inducible promoter were exposed to 2% galactose to trigger the expression of the HO nuclease to cut at the *MAT* locus, and samples were retrieved at the indicated time points for genomic DNA extraction. Subsequent *SspI* digestion, in combination with the use of a probe targeted to *MAT*, allows defining the fate of the cut fragment by Southern blot analysis. As resection progresses on DNA, *SspI* restriction sites are lost, leading to progressively longer ssDNA fragments (whose sizes are indicated at the right of the gel) that can be separated on an agarose gel under denaturing conditions. Given the much stronger signal of the “cut” fragments with respect to the “resected” fragments, the gel has been split into low- and high-contrast halves, respectively. The ssDNA over cut yet unresected DSB molecules was calculated for each shown resection intermediate. The graph on the right plots the sum of all these values (cumulative ssDNA/DSB) for a given resected intermediate during the interval from 90 to 240 min. The error bar is the SEM of three independent experiments. * derives from applying a *t*-test that compares the two populations of values.
- E Cells were preloaded with 60 μM oleate 30 μM BSA (mock) for 4 h, and then exposed to 0.005% MMS for the indicated times. Total genomic DNA was extracted (left panel), and 1,500 ng of each condition was spotted onto a nylon membrane directly. The DNA, after being cross-linked to the membrane, was subjected to detection using an anti-ssDNA antibody (middle panel). The raw ssDNA signals obtained this way were quantified for three independent kinetics. The graph (right panel) shows the mean raw ssDNA signal value and the error bars are the SEM. Unpaired *t*-tests were used to compare the potential differences of the means at each time point. Only the *P*-value(s) for those being significantly different are indicated. As a control for the specificity of the anti-ssDNA antibody, we used the sample “MMS 3 h” for treatment with Mung Bean Nuclease (MBN), in order to digest single-stranded DNA (ssDNA), or for denaturation, by the addition of NaOH to a final 0.4 N concentration. These three samples are shown in the top part of the membrane.

Last, we reasoned that lack of DNA repair would prevent DDR signal extinction even if DSBs are not continuously produced. To test this prediction, we activated the DDR by exposing the cells to zeocin for 90 min, removed it from the medium, and monitored the deactivation of the DDR over time. WT and *tagΔ* cells showed progressive dephosphorylation of Rad53 (Fig 5A and B) and resumed cell cycle progression (Fig 5C). On the contrary, *steΔ* and *yeh2Δ* cells, respectively, unable to esterify sterols or to remove them from membranes, were incapable of Rad53 dephosphorylation (Fig 5A and B) and displayed a delay or a complete halt in cell cycle progression resumption (Fig 5C, red asterisks). Re-migration of protein extracts in more resolutive gels (Fig 5A, bottom panels) allowed specific quantification of Rad53 phosphorylation isoforms. We confirmed that *steΔ* and *yeh2Δ* cells maintained a higher proportion of the two most phosphorylated isoforms of Rad53 4 h after zeocin withdrawal (Fig 5D).

Altogether, the inability to process sterols in response to DSBs leads to an exacerbated DDR and prevents DNA repair and the subsequent deactivation of such a DDR, probably out of a defect in transitioning from short- to long-range resection.

Lack of sterol processing in response to DSBs concurs with an exacerbated activity of the DDR kinase Tel1/ATM

Tel1/ATM acts at the very first steps of DSB recognition and “short-range” DSB end resection, upon which Mec1/ATR takes over Tel1 in the DDR to activate Rad53 (Fig EV2C). But Tel1 participates in the reaction later on by signaling a transient arrest that prevents further “long range” resection (Fig EV2C). After this step, Tel1 is displaced by an unknown mechanism, thus ending DNA repair

and cell cycle resumption (Geuting *et al.*, 2013; Beyer & Weinert, 2014; Clerici *et al.*, 2014). Given that we observed both an acceleration in the detection of breaks (Fig 2) and a defect in the transition from short to long-range resection (Fig 3), we evaluated whether sterol esterification could play a role in the regulation of Tel1 at DSBs. For this purpose, we used a recently created, functional GFP-tagged Tel1 (preprint: Coiffard *et al.*, 2021) to monitor its accumulation in nuclear foci as a readout for its activity at DSBs. In about 40% of the WT cells, 1–5 Tel1 foci per nucleus formed after 40 min of DSB induction with zeocin, a value that declined down to 20% at 210 min (Fig 6A). In contrast, the percentage of *yeh2Δ* cells forming GFP-Tel1 foci doubled that of the WT strain, and *steΔ* cells displaying Tel1 foci reached 70% at the final time point (Fig 6A, right), thus suggesting a higher activity of Tel1 in these mutants. In agreement with a link with Tel1 role at the transition from short to long resection, lack of Yeh2 and absence of the resection factor Sae2 (Clerici *et al.*, 2005) resulted in an epistatic accumulation of Tel1 foci in response to zeocin (Fig 6B).

We also evaluated whether the level of ATM activation related to the metabolism of sterols in human cells. We performed immunofluorescence of ATM phosphorylated at Serine 1981, a marker of its commitment to DNA damage signaling (Bakkenist & Kastan, 2003). When exposing both RPE-1 and Huh-7 cells to MMS, the inhibition of sterol esterification with oleate increased the number of P-ATM-positive cells relative to cells treated with MMS alone, albeit this was not statistically significant (Fig 6C, MMS). However, inducing DSBs with zeocin led to a significant increase in P-ATM-positive cells upon inhibition of sterol esterification with oleate (Fig 6C, zeocin). Importantly, the increase in the phosphorylation of CHK2 observed when preloading the cells with oleate (Figs 2D and 6D)

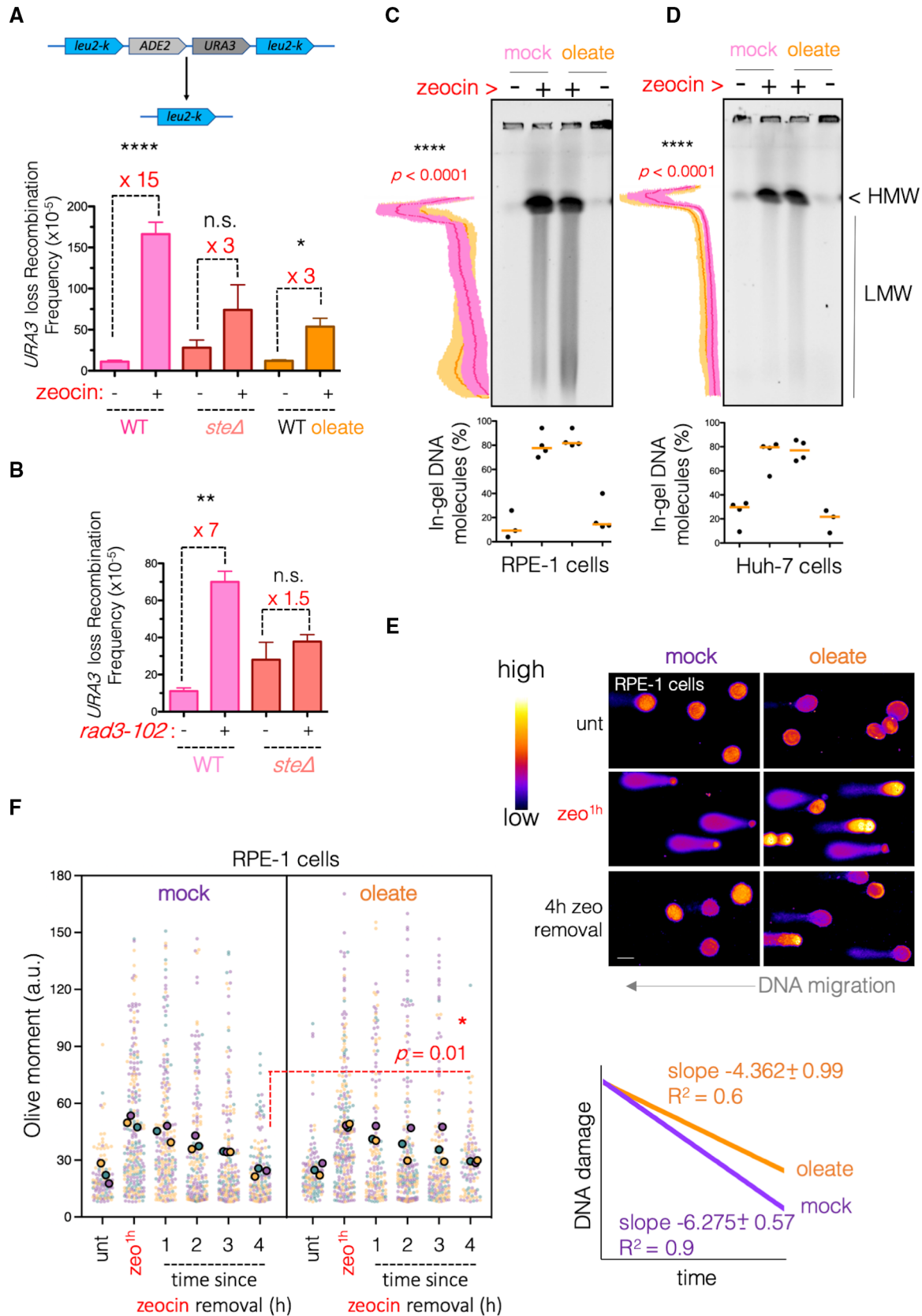


Figure 4.

Figure 4. Impairment in sterol esterification prevents DSB repair.

- A Top:** scheme of the genome-integrated system allowing the analysis of homologous recombination frequency, mostly through single-strand annealing. In brief, two direct repeats of a *leu2-k* allele flank one *ADE2* and one *URA3* copy. Whenever a break occurs in between the two *leu2-k* sequences, concomitant recombination will end up with the loss of the intervening sequences. This loss of the *URA3* marker can be selected for in plates containing 5-FOA, and the frequency of recombinants calculated. **Bottom:** for each recombination test, WT and *steΔ* cells (for which colonies arousal in +zeocin plates took longer given their sensitivity) streaked onto plates containing 7.5 μg/ml zeocin or not, and/or 0.05% oleate or not, as indicated, were grown and 6 isolated colonies out of each plate used to measure the number of recombinant and total cells, thus yielding the shown recombination frequencies. For every six frequencies derived from 6 colonies, one median frequency would be calculated (= 1 experiment). Each bar represents the mean frequency of the median of at least three independent experiments. Zeocin-induced recombination is indicated as a fold change. Statistical evaluation of the differences between the recombination frequencies was evaluated using a t-test: n.s., nonsignificant; **P*-value < 0.01; *****P*-value < 0.0001.
- B** Recombination assay details as in (A) using WT, *rad3-102*, *steΔ* and *rad3-102 steΔ* strains.
- C, D** Pulsed-field gel electrophoresis (PFGE) performed on DNA samples prepared from RPE-1 or Huh-7 cells that had been treated (or not) with zeocin and/or oleate (2 h at 10 μg/ml zeocin; pretreatments for 4 h with 60 μM oleate) to evaluate the presence of DSBs under such treatments. Intact DNA molecules remain in the well, while broken molecules migrate into the gel. Given the action of zeocin, in-gel molecules can be subdivided in high-molecular-weight fragments (indicated by "HMW") and low-molecular-weight ones (LMW). Plugs were prepared at 37°C to prevent artefactual breaking of DNA molecules (Lundin *et al*, 2005). The bottom graphs provide the percentage of total broken molecules per lane with respect to all molecules in that lane. 3–4 independent experiments are plotted, and their median value indicated by an orange bar. The lateral graphs provide the relative intensity (arbitrary units) of signals associated with in-gel broken molecules. The values corresponding to zeocin-treated samples are displayed in pink and those corresponding to oleate + zeocin-treated samples in orange. For pink and orange curves, the mean value of 3–4 independent experiments is displayed in dark color, while the SEM is indicated in light colors. Statistical analyses of the difference between treatments were assessed using a t-test.
- E** Representative images of the comet assays used to evaluate, in a kinetic manner, DNA breaks induction and repair in RPE-1 cells exposed to 100 μg/ml zeocin for 1 h, then washed from zeocin and monitored every hour for 4 h, in the presence or absence of oleate preload. Images have been pseudocoloured using the ImageJ LUT "fire," for which the color code is displayed on the left. Scale bar is 40 μm.
- F Left:** Superplots out of the quantification of 3 independent comet assay experiments. RPE-1 cells were either mock-treated or loaded with 60 μM oleate for 24 h, then exposed to 100 μg/ml zeocin for 1 h, then washed from zeocin and monitored every hour for 4 h. Samples for comet assay were retrieved at each of these time points. The Olive moment for each assessed nucleoid is plotted as an individual light-colored dot. Each experiment can be recognized by a color. The mean value of all Olive moments from a single experiment at every given time point is highlighted as a big, filled dot. The *P*-value expresses the significant difference between the mean of the final time point after applying a t-test. **Right:** The three Olive moment mean values for each time point were used to derive a line for both mock and oleate conditions, whose slopes and *R*² values were calculated, in order to provide a rough estimate of the respective repair kinetics. The graph is a scheme to illustrate both slopes.

was dependent on ATM activity, as it could be abolished by the addition of the ATM inhibitor AZD0156 to both cell types (Fig 6D). Of note, the increase in P-ATM did not translate into more extensively phosphorylated H2AX (Fig 6E), again reinforcing the idea that the exacerbation of Tel1/ATM activation is more of a temporal than of a spatial nature. Thus, preventing the storage of sterols into LD in response to DSBs leads to an exacerbated activation of the DDR upstream kinase Tel1/ATM.

Tel1/ATM binds phosphatidylinositol-4-phosphate

Sterols modulate proteins through their transmembrane segments, yet Tel1 and ATM are soluble proteins. We reasoned that sterol presence in membranes could indirectly affect other lipids with regulatory potential, in turn impacting Tel1/ATM activity. Tel1 and ATM are phosphatidylinositol-3-kinases-like kinases (PI3KKs), thus ancestrally related to phosphatidylinositol-3-kinases (Hunter, 1995). We asked whether Tel1 kept the potential of a physical interaction with phosphoinositides (PIPs). We immunopurified a functional FLAG-tagged Tel1 (Fig EV3A and B) from *S. cerevisiae* (Hirano *et al*, 2009) and incubated the eluate with a commercially available membrane on which phosphatidylinositol (PI) and its six phosphorylated PIP variants are spotted. Additional, unrelated lipid species are also spotted on that membrane. We observed robust anti-FLAG signals specifically against the three monophosphate PIPs, namely PI(3)P, PI(4)P, and PI(5)P (Fig EV3C), while FLAG-Tel1 affinity for the di- and tri-PIP species was low or absent. In our particular interest, PI(4)P is related to the metabolism of sterols at the interface between the trans-Golgi and the endoplasmic reticulum (ER). There, the OSBP1 exchanger promotes the extraction of sterol moieties

from the ER and their insertion in the trans-Golgi in exchange of PI(4)P, which then follows a reciprocal fate (Fig 7A; Mesmin & Antony, 2016; Mesmin *et al*, 2017; Antony *et al*, 2018). Thus, if Tel1/ATM were to bind PI(4)P, this could explain why high level of unesterified sterols affects this kinase. We incubated again purified FLAG-Tel1 with a membrane in which only the three variants of PI(4)P were spotted, and observed again a clear preference for the monophosphate species, while no signal at all was obtained if a similar membrane was incubated with 3XFLAG peptides only (Fig 7B). To probe for the interaction in a more physiological context, we incubated purified FLAG-Tel1 with liposomes (spheres composed of a phospholipid bilayer) in which PI(4)P was inserted. While we observed FLAG-Tel1 binding, residual FLAG-Tel1 signals appeared in the no-liposome control, indicating that the protein mildly precipitates in this experimental setup (Fig EV3D). Thus, we performed floatation assays, in which a discontinuous sucrose gradient is poured onto the FLAG-Tel1 + liposome mix previously deposited in the bottom of the tube. Upon ultracentrifugation, the liposomes float up to the top gradient fractions, where FLAG-Tel1 would be found only if it can bind the liposomes. While FLAG-Tel1 remains in the bottom fraction in the absence of liposomes, it can be found in the top fraction only when incubated with liposomes harboring PI(4)P (Fig 7C), thus confirming the FLAG-Tel1/PI(4)P interaction.

In both human RPE-1 and Huh-7 cells, we assayed the interaction of ATM with PI(4)P by proximity ligation assay (PLA) using a well-documented anti-PI(4)P antibody (Hammond *et al*, 2009) and an antitotal ATM antibody. The PLA assay yielded specific signals in the cytoplasm (Fig 7D), as demonstrated by loss of signals in technical controls (absence of one primary antibody at a time; Fig 7D, bottom left), or biological controls (siRNA-mediated depletion of ATM,

Figs EV3E and 7D, bottom right). Yet, basal levels detected in Huh-7 cells were low, close to the one-antibody-only control levels, probably indicating a less frequent basal association in these cells (Fig 7D). Importantly, these cytoplasmic PLA signals co-localized with the trans-Golgi marker TGN46 (Fig EV3F, left panel,

arrowheads) and, even when some of them visually overlapped with the nucleus, careful assessment revealed co-localization with perinuclear Golgi stacks (Fig EV3F, right panel). From all these experiments, we conclude that Tel1/ATM interacts with cytoplasmic PI(4)P in the absence of DNA damage.

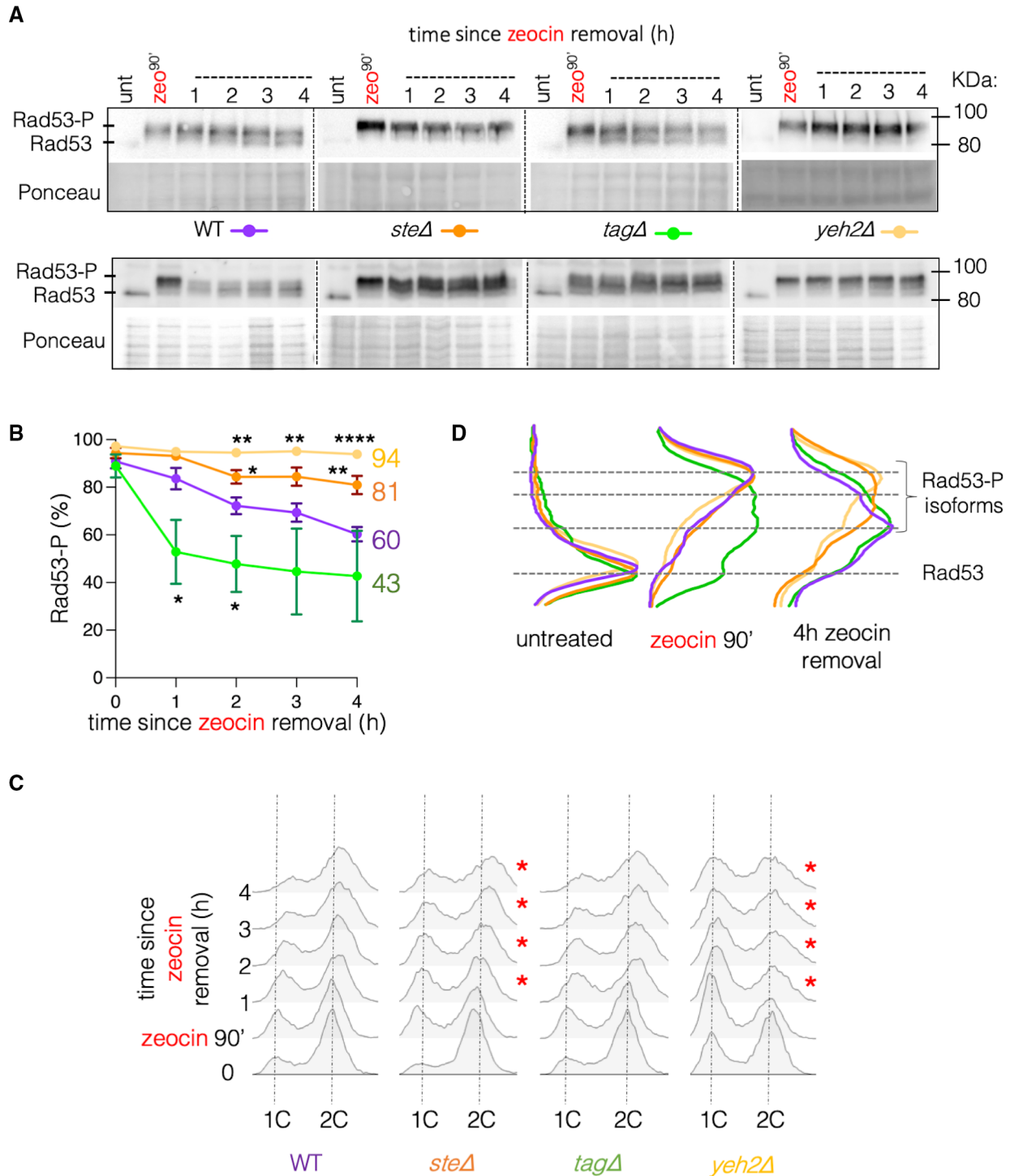


Figure 5.

Figure 5. Impairment in sterol esterification prevents DDR deactivation.

- A Exponentially growing *Saccharomyces cerevisiae* WT, *steΔ*, *tagΔ* and *yeh2Δ* cells were treated with 100 μg/ml zeocin for 90 min. This treatment duration recurrently results in more cells accumulating in the G₁ phase of the cell cycle (Figs 1B and 5C and EV2A; Appendix Fig S1D). After 90 min, cells were washed to remove zeocin and resuspended in fresh, zeocin-free medium, and samples were retrieved every hour, as indicated. All samples were processed for western blot analysis and cytometry. The deactivation of the DDR was monitored following the progressive dephosphorylation of Rad53. The unphosphorylated and phosphorylated isoforms of Rad53 are indicated (Rad53 and Rad53-P, respectively). Ponceau staining is shown as a loading control. Top: samples were migrated using commercial 3–8% gradient gels. Bottom: samples were migrated in home-made resolutive gels (see M&M).
- B The percentage of Rad53-P was quantified at each time point as in Fig 2B. The plotted values represent the mean value of at least 3 independent experiments and the variability is represented by the SEM. Unpaired one-way ANOVA tests were conducted to compare the potential differences of the means of the four conditions at each time point. Only the *P*-value(s) for the comparisons being significantly different are indicated, where **P* < 0.05; ***P* < 0.01; *****P* < 0.0001.
- C Cytometry profiles corresponding to the samples described in (A). Red asterisks indicate cytometry time points where cell cycle progression was delayed in comparison with the WT strain.
- D The relative intensity of the fine bands corresponding to each Rad53-P isoform (A, bottom gels) from the indicated time points were plotted to better illustrate the deactivation status of the DDR in each strain.

ATM/Tel1 nuclear availability is conditioned by the OSBP1 exchanger

The OSBP1 exchanger activity is driven forward thanks to the activity of the SAC1 phosphatase, which continuously hydrolyzes the translocated PI(4)P moieties that reach the ER (Fig 7A; Mesmin & Antony, 2016; Mesmin et al., 2017; Antony et al., 2018). Considering that (i) Tel1/ATM binds PI(4)P in its basal state (Fig 7) and that (ii) high level of sterols in ER membranes, which promotes PI(4)P exchange and hydrolysis (Von Filseck et al., 2015; Mesmin et al., 2017), promotes an exacerbated Tel1/ATM activity (Fig 6), we hypothesized that nontranslocated PI(4)P present at the Golgi may act as a lock that limits Tel1/ATM availability in the nucleus.

To test this hypothesis, we first reasoned that DNA damage, which causes ATM relocation to the nucleus, would decrease the ATM-PI(4)P proximity signals obtained in PLA experiments. In RPE-1 cells, where basal signals were elevated enough (Fig 7D) as to assess a putative decrease, zeocin or MMS treatments significantly led to a loss of ATM-PI(4)P PLA signals (Fig 8A). In a complementary approach, we found upon cell fractionation that a basal pool of cytoplasmic ATM indeed exists in RPE-1 cells and that part of it translocates to the nucleus upon zeocin treatment (Fig 8B). Reciprocally, treating cells with the specific ATM inhibitor AZD0156, which is predicted to stabilize the ATM/PI(4)P interaction, increased the number of PLA signals (Fig EV4A).

Our hypothesis also implies that ATM release into the nucleus stems from a consumption of Golgi-associated PI(4)P. Detection by two different strategies of Golgi-associated PI(4)P molecules demonstrated a reduction in the area occupied by these signals, suggestive of PI(4)P consumption in response to these agents: first, transfecting a fluorescent biosensor derived from OSBP1 PI(4)P-binding site illuminated deployed PI(4)P signals whose extension and number decreased upon zeocin or MMS treatments (Fig EV4B). Second, directly monitoring PI(4)P with a specific antibody showed its marked basal co-localization with the Golgi marker GOLPH3 and how these PI(4)P signals decreased following zeocin or MMS treatments. The signal disappearance was comparable to a control in which in PI(4)P synthesis was prevented using the specific inhibitor PIK93 (Fig 8C). Together, it appeared that the association of ATM with PI(4)P inversely correlates with the need for ATM within the nucleus.

Next, we surmised that, since boosting the activity of the OSBP1 exchanger consumes PI(4)P more readily, this should render more

ATM/Tel1 available for the nucleus. We overexpressed the OSBP1 counterpart in *S. cerevisiae*, Osh4 (Beh et al., 2012; Mesmin et al., 2017), then exposed cells to zeocin and monitored their ability to form nuclear Tel1 foci in comparison with cells expressing an empty plasmid. While the kinetics of Tel1 foci formation remained unchanged, the percentage of cells displaying nuclear Tel1 foci was increased from 20 to 30% throughout the whole kinetics when Osh4 was overexpressed (Fig 8D), in agreement with the prediction.

In a reciprocal approach, we reasoned that, if cells could not hydrolyze PI(4)P, such as in the absence of SAC1, PI(4)P is expected to accumulate thus sequestering Tel1 away from the nucleus. In agreement, 80% of *sac1Δ* cells displayed cytoplasmic GFP-Tel1 foci that, moreover, were irresponsive to zeocin treatment (Fig EV4C). Additionally, as the absence of Tel1 leads to shortened telomeres (Greenwell et al., 1995), we used a terminal transferase-assisted PCR (Forstemann et al., 2000; Teixeira et al., 2004) to assess the length of telomeres in a strain deleted for SAC1. Indeed, we observed that both X and Y' telomeres display an intermediate length in *sac1Δ* compared with WT and *tel1Δ* cells (Fig 8E). Altogether, we conclude that ATM/Tel1 availability in the nucleus is influenced by its binding to cytoplasmic PI(4)P.

The OSBP1 exchanger conditions ATM activation and activity

We then wanted to ascertain whether the reduced availability of ATM in the nucleus as shown above translated into functional consequences when cells were exposed to different types of agents creating DSBs. To assess this, we treated cells with different ATM-activating genotoxins and then monitored whether phosphorylated ATM signals could be switched off by adding the specific OSBP1 inhibitor schweinfurthin G (SWG; Péresse et al., 2020). As a control, we did the same experiments using the ATM inhibitor AZD0156 instead of SWG. First, we recurrently observed that genotoxic treatments led to the stabilization of ATM protein (Fig EV4D). As such, we turned to use calnexin as a loading control (Figs 9A and EV4D). Although there were subtle differences when comparing the various genotoxins, inhibiting OSBP1 had the ability to reduce phosphorylated ATM levels in RPE-1 cells in all instances (Fig 9A). To provide genetic proof of this same notion, we also silenced OSBP1 using siRNAs and monitored the specific ATM activity on chromatin by following the phosphorylation of its target KAP-1 (Ziv et al., 2006). We found decreased KAP-1 phosphorylation in OSBP1-depleted cells (Fig 9B). Thus, the predicted decrease in ATM availability in the

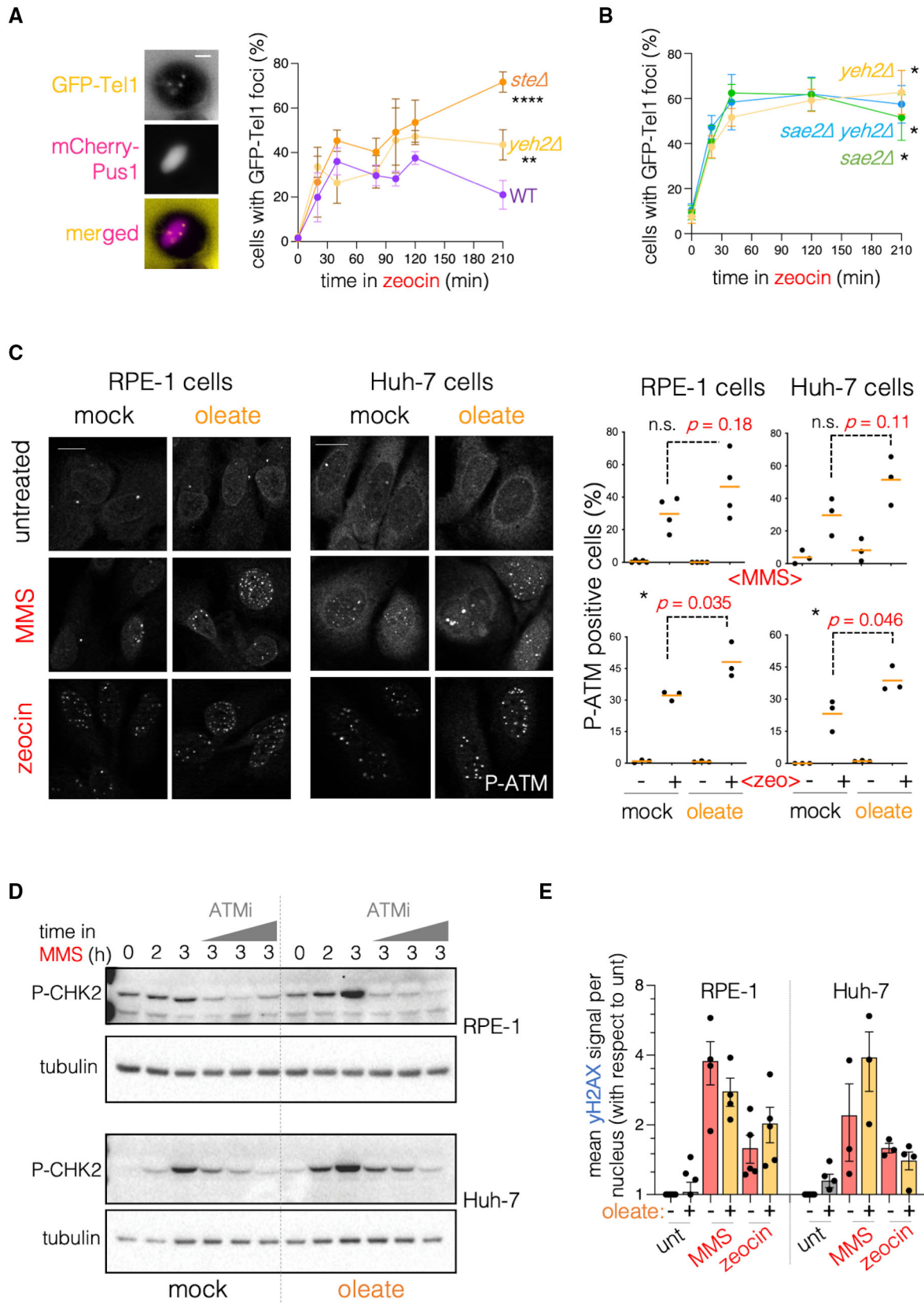


Figure 6.

Figure 6. Tel1/ATM displays excessive activation in sterol removal-deficient contexts.

- A Exponentially growing *S. cerevisiae* WT, *steΔ* and *yeh2Δ* cells were treated with 100 μg/ml zeocin and samples retrieved at the indicated time points for inspection by fluorescence microscopy. The involvement of Tel1 in the response to zeocin was evaluated by its ability to form GFP-Tel1 foci. Left: an illustrative image of the WT strain forming GFP-Tel1 foci in response to 100 μg/ml zeocin after 80 min. mCherry-Pus1 was used to define the nucleus boundaries. Scale bar is 3 μm. Right: graph displaying the mean value of the percentage of cells forming GFP-Tel1 foci and the SEM of 3 independent experiments for the indicated strains. A one-way ANOVA for multiple comparisons was applied to evaluate whether there were significant differences between the means of the 210 time point and the obtained *P*-values are indicated by asterisks. ***P* < 0.01; *****P* < 0.0001.
- B Details as in (A) but for the indicated strains. A one-way ANOVA for multiple comparisons against the WT values (not plotted) was applied to evaluate whether there were significant differences between the means of the 210 time point. *P*-values are indicated by asterisks. **P* < 0.05.
- C Left: Representative images obtained after immunofluorescence to detect P-ATM (ATM phosphorylation at Serine 1981) signal in RPE-1 and Huh-7 fixed cells that had been treated (or not) with 0.005% MMS or 10 μg/ml zeocin for 2 h; pretreatments were done for 4 h with 60 μM oleate. Size bars are 10 μm. Right: Quantification of the percentage of P-ATM-positive cells. The values obtained from 3 to 4 independent experiments are plotted as black spots, and the mean of them is shown as an orange bar. At least 200 cells were counted per condition and experiment. The *P*-values obtained after performing an unpaired *t*-test are shown.
- D RPE-1 and Huh-7 cells were treated or not with MMS 0.005% for 2 h. Thereafter, the ATM inhibitor AZD0156 was added at a final concentration of 1, 10 or 50 nM for 1 h. Cells were collected and phosphorylation on Thr68 of CHK2 and tubulin levels were analyzed by western blot.
- E Details as in (C) but to detect phosphorylated H2AX (γH2AX). The graph shows the mean fold change in signal per nucleus out of at least 300 nuclei counted per condition and experiment. 3 to 4 independent experiments were performed. The bar height indicates the value of the mean of the means and, the error bars, the associated SEM.

nucleus matched a decreased level of activated ATM. We further reinforced this notion by performing synergy matrices, in which the combination of increasing doses of two drugs is evaluated for their ability to synergistically impair cell growth. ATM and ATR act as parallel branches ensuring cell fitness, which underlies the basis of the lethality observed when combining ATM and ATR inhibitors (Reaper *et al.*, 2011). If OSBP1 inhibition leads to ATM retention away from the nucleus, then simultaneous ATR and OSBP1 inhibition should partly mimic the aforementioned genetic interaction. In agreement, four independent synergy matrices revealed a synergistic lethal interaction between the ATR inhibitor VE-821 and the OSBP1 inhibitor SWG (Fig 9C, bright magenta).

Last, and as a readout for events downstream of ATM signaling, we evaluated whether prior inhibition of OSBP1 with SWG had an impact on the onset of DNA resection, as expected if ATM activation (and activity) are delayed or reduced. We incubated cells with the thymidine analog BrdU for 16 h. BrdU incorporated in double-stranded DNA can only be detected by an anti-BrdU antibody if resection starts, thus exposing it (Mukherjee *et al.*, 2015). Since the kinetics of BrdU exposure is well established in response to camptothecin (CPT; Kousholt *et al.*, 2012), we exploited this framework in our experimental setting. In RPE-1 cells, nuclei displaying resection could readily be detected at 30 min and their number peaked 60 min after CPT addition, remaining stable from that moment on (Fig 9D). In marked contrast, specific ATM inhibition by AZD0156 sharply diminished (yet without abolishing) both the kinetics and the maximum number of nuclei engaged in resection (Fig 9D). OSBP1 inhibition by SWG similarly slowed down the kinetics with which cells engaged in resection (Fig 9D). Thus, the availability and, concomitantly, the activity of ATM/Tel1 in the nucleus is modulated by the activity of the OSBP1 exchanger.

Discussion

In this work, we report that the physical and functional availability of ATM/Tel1 in the nucleus is subordinated to its cytoplasmic binding to the lipid PI(4)P, whose half-life is itself linked to the activity of the OSBP1 exchanger. In response to DNA DSBs, Tel1/ATM accumulates in the nucleus, engaging the activation of the DDR through

effectors such as Rad53/CHK2. Likely as a downstream outcome, we uncover the storage of sterols within LD as a necessary step to promote Tel1/ATM nuclear decline, which is itself mandatory to permit DNA long-range resection and repair (Fig 10A). This titration operates through the binding of Tel1/ATM to Golgi-resident PI(4)P. In situations where sterol removal from membranes is implemented, OSBP1 activity is low, as no sterol moieties are available for exchange against Golgi-resident PI(4)P. PI(4)P stabilized this way titrates ATM from the nucleus (Fig 10B, right). On the contrary, if sterol removal from membranes is prevented, this will boost OSBP1-mediated extraction of Golgi PI(4)P, thus allowing an increased presence of Tel1/ATM in the nucleus and, with it, a more robust DDR whose inability to be dampened will hinder downstream DNA repair steps (Fig 10B, left). These findings highlight the importance of fine-tuning ATM nuclear levels: high Golgi-bound PI(4)P, exacerbated OSBP1 activity or boosted SAC1 hydrolysis of PI(4)P will create a hyper-responsive DDR, yet inability to complete DSB repair. On the contrary, elevated Golgi-bound PI(4)P, low sterol levels in the ER, or decreased OSBP1 activity will lead to a strong Tel1/ATM retention at the Golgi, thus resulting in basal telomere shortening and a less responsive DDR.

PI(4)P is a crucial piece in the puzzle of ATM biology

In its inactive state, ATM displays a dimeric conformation and, upon activation, its autophosphorylation at serine 1981 correlates with its monomerization. While this autophosphorylation is essential *in vivo* to activate ATM (Bakkenist & Kastan, 2003), its function remains elusive because it is completely dispensable *in vitro*. In this case, dimer-to-monomer transition as well as substrate recognition and phosphorylation by ATM still occurs without autophosphorylation (Lee & Paull, 2005). Previously, it was suggested that a yet undiscovered factor may bind ATM *in vivo* basally, thus preventing its monomerization, and thereby inhibiting its kinase activity (Paull & Lee, 2005). Herein, we show that ATM/Tel1 constitutively associates with PI(4)P and that PI(4)P consumption is necessary to promote ATM translocation to the nucleus in response to DNA damage. Furthermore, we show that cell treatments with genotoxic drugs leading to ATM activation elicit the dissociation of ATM and PI(4)P. We therefore propose that PI(4)P is the missing factor that, *in vivo*,

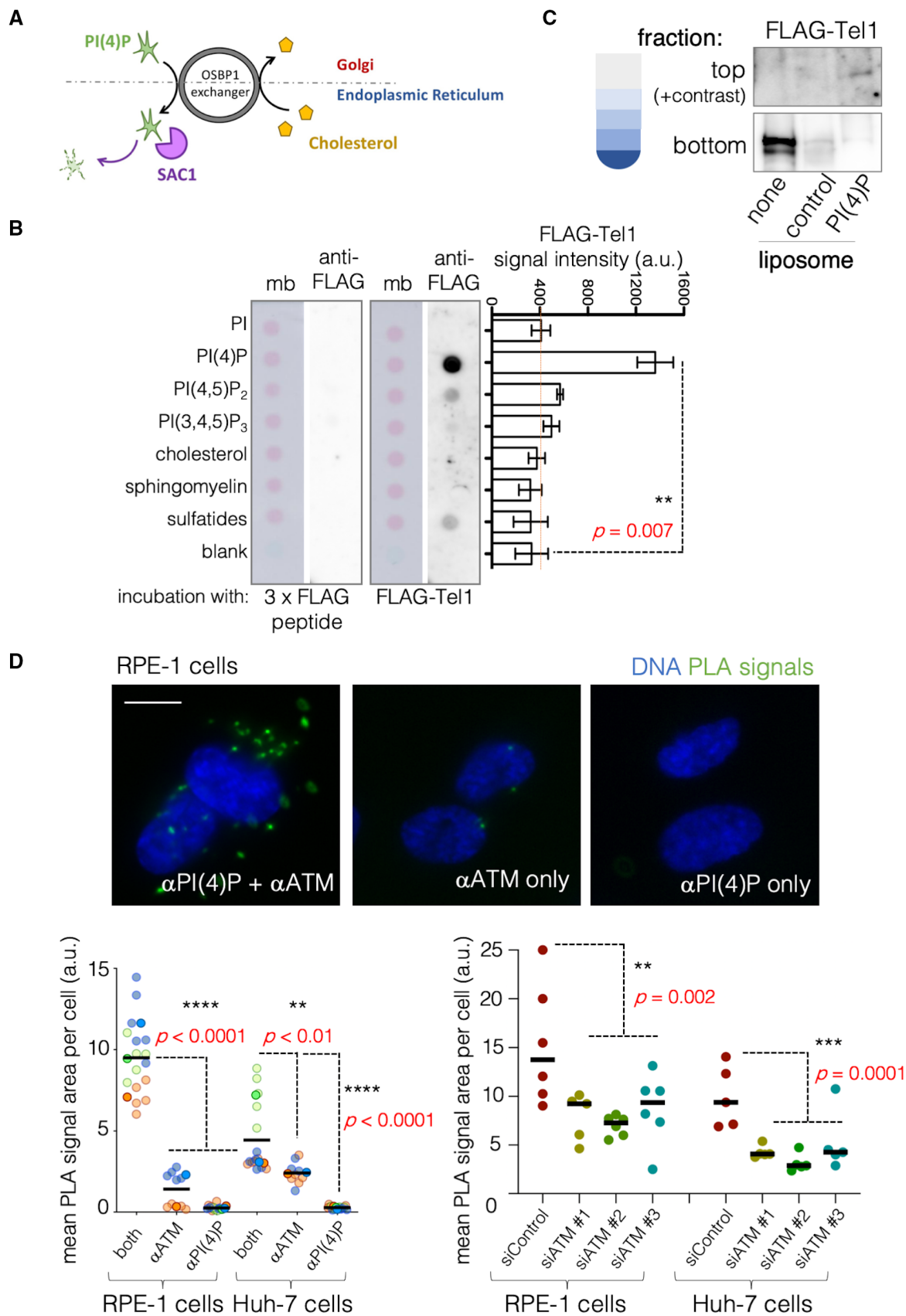


Figure 7. ATM/Tel1 binds PI(4)P.

- A Illustration of how the OSBP1 exchanger works. The distance between the Golgi and the endoplasmic reticulum (ER) is represented by the dashed line and their connection established through OSBP1, whose activity is represented as a wheel whose directionality is given by black arrows. It extracts cholesterol from the ER and sends it to the Golgi in exchange for PI(4)P that is extracted from the Golgi and sent to the ER. In the ER, the phosphatase SAC1 hydrolyses PI(4)P, which releases ATP, further fostering the exchange.
- B A hydrophobic membrane on which 100 pmol of the indicated lipid species were spotted was incubated with immunopurified FLAG-Tel1 and further developed using an anti-FLAG antibody. The bar lengths in the graph represent the mean value of 4 independent experiments and the error bars, the associated SEM. To assess whether the mean values differed significantly, a *t*-test was performed and *P*-values are shown. Additionally, an identical lipid-containing membrane was incubated with 3xFLAG peptide and subsequently developed using an anti-FLAG antibody to control that the observed signals were not due to FLAG peptide binding alone. PI; phosphatidylinositol; PI(4)P, phosphatidylinositol-4-phosphate; PI(4,5)P, phosphatidylinositol-4,5-bisphosphate; PI(3,4,5)P, phosphatidylinositol-3,4,5-triphosphate.
- C Liposome floatation assay. Purified FLAG-Tel1 was incubated with control liposomes, liposomes containing embedded PI(4)P, or nothing, and this mixture deposited in the bottom of an ultracentrifugation tube on top of which was poured a discontinuous sucrose gradient, the whole then being subjected to ultracentrifugation. The blot shows the anti-FLAG signals obtained after retrieving samples from the top and the bottom gradient fractions.
- D Proximity ligation assay (PLA) to assess whether ATM and PI(4)P are in close proximity (< 40 nm). **Top:** representative pictures of RPE-1 cells, in which PLA signals are pictured in green. Size bar is 10 μ m. **Bottom left:** the graph shows the mean PLA signal area occupied per cell when doing the experiment with both antibodies (experiment) or by omitting one primary antibody at a time (technical controls). In practice, each point is the value of having measured all the PLA signals present in one photo (20–40 cells) and divided this value by the number of nuclei. To account for reproducibility, we used SuperPlots to draw the graphs (Lord *et al.*, 2020): each independent experiment is plotted in a different color, where the mean value of each independent experiment is highlighted by a more intense color than the individual values of that experiment, for which the color is more translucent. Last, the solid horizontal line marks the mean of the means. A one-way ANOVA for multiple comparisons was applied to evaluate whether there were significant differences between the means. **Bottom right:** the graph shows the mean PLA signal area occupied per cell when doing the experiment either in cells transfected with an siRNA Control (experiment) or with three different siRNAs targeted against ATM (biological controls). The meaning of each plotted point, of the horizontal line and the statistical analysis is as explained above. ATM depletion efficiency can be seen in the western blots presented in Fig EV3E.

keeps ATM inactive. It would be important to assess, in future work, how ATM autophosphorylation at serine 1981 and PI(4)P binding relate to each other. In this context, we propose that ATM inhibitors, by restricting ATM activation, will consequently exacerbate its Golgi association (Fig EV4A), therefore limiting ATM action not because of lack of activity, but because of lack of nuclear localization. Also, and since PI(4)P is bound by a myriad of interactors, playing crucial roles in Golgi homeostasis (Santiago-Tirado & Bretscher, 2011), our data imply that the extent of ATM binding to PI(4)P may have an indirect impact on Golgi biology.

Our results also shed light on another mystery surrounding Tel1/ATM biology. Tel1 and ATM are both reported to regulate the transition from short- to long-range resection at DNA double-strand breaks, but the mechanism controlling Tel1/ATM unbinding from DNA to promote resection resumption is unknown (Geuting *et al.*, 2013; Clerici *et al.*, 2014). Here, we propose that the removal of sterols from ER membranes via their storage within LD, as induced by DNA breaks, slows down the OSBP1 exchanger activity, thus decreasing PI(4)P hydrolysis. PI(4)P levels increased this way progressively sequester ATM away from the nucleus. The window of action of ATM would therefore depend on the time needed for sterol levels to drop at the ER. This implies that the ER and the Golgi are key organelles in the attenuation of the DDR, thus ruling crucial downstream aspects such as DNA repair, adaptation to DNA damage or apoptosis. Additionally, our model implies that, in response to DNA damage, the specific esterification and storage of sterols within LD needs to be instructed. It will be key in the future to assess whether the DDR itself targets factors involved in this process.

Expanding the link between DNA damage and phosphoinositides

The connection between DNA damage and PIPs is increasingly growing (recently reviewed in Wang & Sheetz, 2022). In this line, the pool of nuclear PI(4,5)P has been recurrently linked to DNA damage (Rana *et al.*, 1994; Wang *et al.*, 2017; Choi *et al.*, 2019).

Functionally, PI(4,5)P is important to prime the activation of the master DDR kinase ATR (Wang *et al.*, 2017) and to form a docking platform with p53 that would lead to PI(4,5)P conversion into PI(3,4,5)P, the whole being key to silence FOXO-associated transcription thus attenuating DNA damage-induced apoptosis (Chen *et al.*, 2022). Furthermore, PARP1, a very early responder to DNA damage, is a PI(3,4,5)P₃-interacting protein (Wang *et al.*, 2022). We find that our sterol/PI(4)P loop is not eliciting effects related to the ATR-CHK1 branch of the DDR (Fig EV1B), suggesting that our findings do not deal with the PI(4,5)P/PI(3,4,5)P-related pathway. This is in agreement with the observation that distinct spatial pools were described for PI(4)P and PI(4,5)P inside the nucleus of human cells under basal conditions (Fáberová *et al.*, 2020) and altogether raises the possibility that different PIPs rule the distinct branches of the DDR. Yet, the pool of PI(4)P we discover as a controller of ATM is not nuclear, but Golgi-resident. This in turn raises additional questions, such as what is the fate of nuclear PI(4)P upon DSBs and, if some of it remains, how it influences ATM once it translocates to the nucleus.

Therapeutic implications of the DDR-lipids connection

Cancer cell proliferation is supported by attenuation of the DDR and increased lipid metabolism. Cancer cells bear an increased number of LD that correlates with tumor aggressiveness, bad prognosis, and chemotherapy resistance (Bozza & Viola, 2010; Yue *et al.*, 2014; Abramczyk *et al.*, 2015; de Gonzalo-Calvo *et al.*, 2015; Qiu *et al.*, 2015). Our work identifies the cholesterol-PI(4)P axis as an unprecedented Tel1/ATM activity modulator, able to influence the kinetics and intensity of the DDR in response to DSBs. We propose that cancer cells may maintain their typically irresponsive DDR through a modification of the sterol-PI(4)P-ATM loop warranting them an attenuation of their DDR. This could happen through an enhanced storage of sterol esters within LD. Reminiscently, an increase in the number and size of LD had already been reported in *mrx* mutants, deficient in DSB sensing and repair (Kanagavijayan

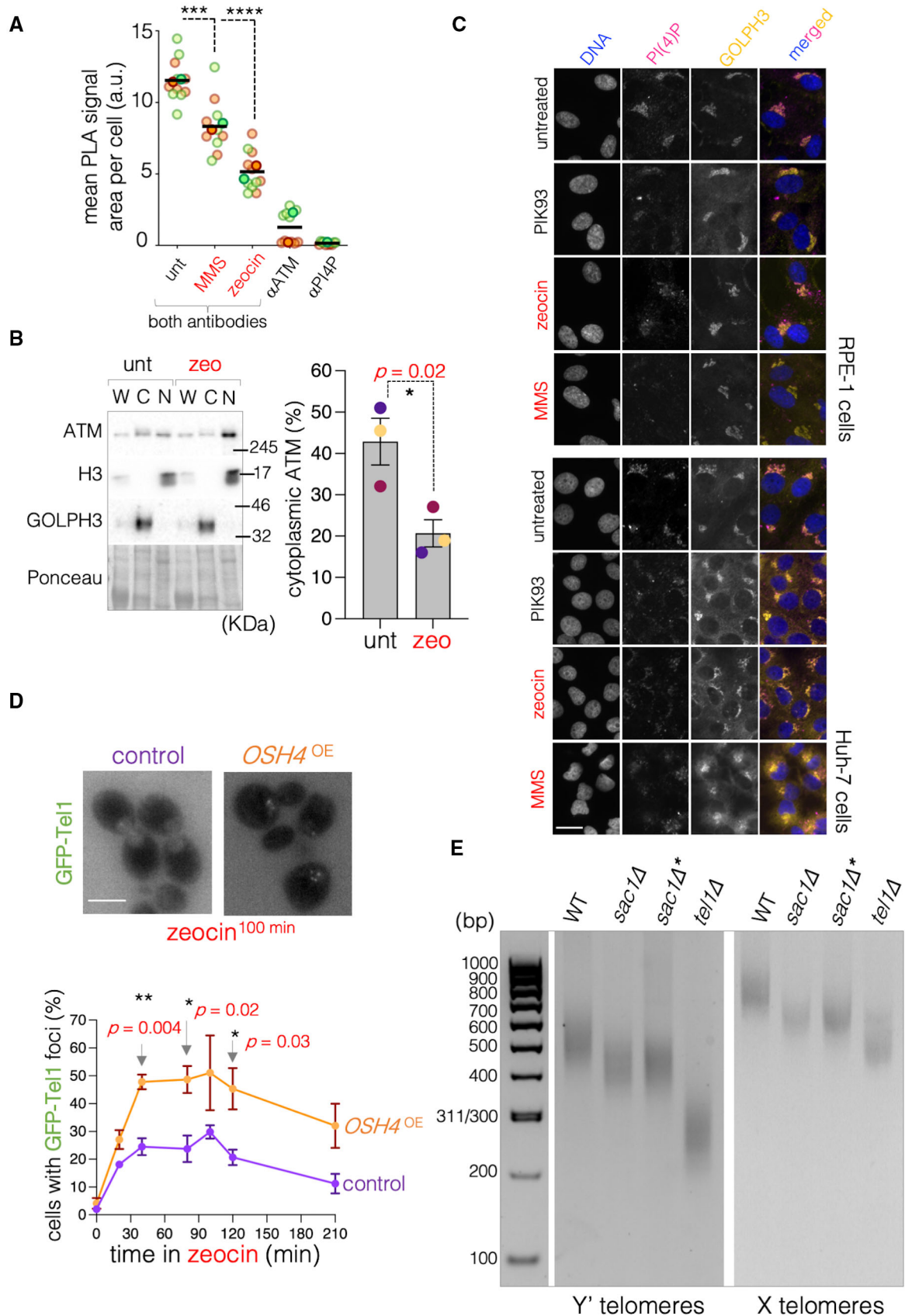


Figure 8.

Figure 8. ATM/Tel1 presence in the nucleus is ruled by OSBP1/Osh4 activity.

- A PLA to assess whether ATM and PI(4)P proximity is altered in response to DNA damage. The graph shows the mean PLA signal area occupied per cell, where each point represents the value of all measured PLA signals in one image (20–40 cells) divided the number of nuclei. Each independent experiment is plotted in a different color. The mean value of each independent experiment is highlighted by a more intense color than the individual values of that experiment, for which the color is more translucent. The solid horizontal line indicates the mean of the means. A one-way ANOVA for multiple comparisons was applied to evaluate whether there were significant differences between the means of the indicated conditions, where $***P < 0.001$; $****P < 0.0001$.
- B **Left:** RPE-1 cells untreated or exposed to 10 $\mu\text{g/ml}$ zeocin for 2 h were used either for whole-cell protein extraction (W) or for fractionation into cytoplasmic (C) and nuclear (N) fractions in order to assess relative ATM distribution. Fractionation quality was assessed by checking for histone 3 (H3) (nucleus) and GOLPH3 (cytoplasm) signals. **Right:** To quantify the relative distribution of total ATM between nucleus and cytoplasm, total ATM signals were normalized to total Ponceau signals from the corresponding fraction. Each dot of a given color belongs to an independent experiment, the bar height shows the mean of those experiments, and the error bars represent the SEM. The *P*-value is derived from an unpaired *t*-test.
- C Immunofluorescence to detect PI(4)P signals using a specific antibody against fixed RPE-1 and Huh-7 cells that had been exposed to the indicated treatments (2 h 0.005% MMS, or 10 $\mu\text{g/ml}$ zeocin, or 4 h 10 μM PIK93 to inhibit PI(4)P synthesis). GOLPH3 detection has been included to confirm the localization of the identified PI(4)P pool with the Golgi. Scale bar is 20 μm .
- D Exponentially growing *S. cerevisiae* WT cells transformed with an empty vector ("control") or with a plasmid overexpressing *OSH4* (Beh & Rine, 2004) were treated with 100 $\mu\text{g/ml}$ zeocin and samples collected at the indicated time points for inspection by fluorescence microscopy to evaluate the percentage of cells displaying GFP-Tel1 foci. **Top:** illustrative images of GFP channel (nuclear Tel1 signals) in the indicated conditions. Note that we systematically monitor mCherry-Pus1 to ascertain whether signals are nuclear or not. Scale bar is 6 μm . **Bottom:** graph displaying the mean value of the percentage of cells forming GFP-Tel1 foci and the SEM of 3 independent experiments for the indicated conditions. Unpaired *t*-tests were used to compare the potential differences of the means at each time point. Only the *P*-value(s) for those being significantly different are indicated.
- E Telomeres (X and Y) length was measured by PCR-mediated amplification (see [Materials and Methods](#)) from genomic DNA extracted from the indicated strains. *tel1Δ* cells were included as a control given their shortened telomere phenotype. The asterisks in some *sac1Δ* lanes refer to these strains harboring the GFP tag at Tel1 N terminus, to denote that this manipulation does not influence telomeres length.

et al., 2015). DDR attenuation could also occur, as recently reported, by an exacerbated synthesis of PI(4)P, to which adenocarcinoma cells are addicted (Shi *et al.*, 2021). In the same line, recent findings highlight the potential of targeting the metabolism of cholesterol for modulating the DDR in gallbladder cancer (Zhang *et al.*, 2019).

Our findings could also be important for nondividing cells, such as postmitotic neurons. In these cells, a low ATM activity drives DSB repair by nonhomologous end joining (Sordet *et al.*, 2009; Tomashevski *et al.*, 2010), and a precise control of this DDR is key (Panier & Durocher, 2013): An excessive activity of ATM decompacts chromatin (Ziv *et al.*, 2006), and open chromatin becomes more prone to repair by HR (Aymard *et al.*, 2017). Consequently, the excessive activity of ATM forces the progression of these cells to S

phase, which triggers apoptotic mechanisms in neurons (Lee & McKinnon, 2000; Yang *et al.*, 2001; Kruman *et al.*, 2004; Alvira *et al.*, 2007). Thus, limiting the extent of ATM activity by the lipid environment in a noncycling cell may be crucial for its survival.

Last, our findings could shed light onto mechanisms underlying lipodystrophy, where a loss of white adipose tissue gives rise to ectopic fat deposition and engenders severe metabolic alterations. The lack of adipose tissue can be ascribed either to incorrect adipocyte development, or lack of TAGs formation/storage within LD. Yet, in the case of some familial partial lipodystrophies, such as Hutchinson–Gilford progeria syndrome (HGPS), the causative molecular defect has remained poorly linked to problems in LD storage. Molecularly, HGPS resembles a genome instability syndrome:

Figure 9. OSBP1 inhibition limits ATM activation.

- A Western blot showing P-ATM (ATM phosphorylation at Serine 1981) detection. Calnexin is used as a loading control (see Fig EV4D for explanation). The experiment assesses the ability of the ATM inhibitor AZD0156 (ATMi) or the OSBP1 inhibitor schweinfurthin G (SWG) to extinguish P-ATM signals triggered by the previous exposure to different genotoxins. Thus, RPE-1 cells were treated either with 0.005% MMS, or 10 $\mu\text{g/ml}$ zeocin, or 120 ng/ml neocarzinostatin (NCZ), or 200 μM camptothecin (CPT, see [Materials and Methods](#)) for 2 h, then 500 nM AZD156 (ATMi) or 10 nM SWG were added in the sustained presence of the genotoxins for 2 additional hours. The images are illustrative of three to four independent experiments whose quantifications are shown in the bottom. Each point illustrates the observed raw P-ATM signal for each condition in each experiment, and similarly colored dots belong to a same experiment. All the signals belonging to a same experiment were obtained from simultaneously run and transferred gels and simultaneously hybridized and exposed membranes. Thick dashed black lines represent the median of the experiments, and their specific value is shown as a red number on top of each violin plot, while thin dashed black lines indicate first and third quartiles.
- B **Top:** RPE-1 cells transfected after 3 days with siRNA control or against OSBP1 (3 different siOSBP1 sequences were assessed independently) were exposed to 0.005% MMS for the indicated times and the phosphorylation status of KAP-1 on Ser 824 was assessed by western blot. Total KAP-1 signals and the Ponceau staining are used as loading controls. **Bottom:** graph displaying the P-KAP-1/KAP-1 ratio. Each plotted value is the mean out of three independent experiments, and the error bars account for the SEM. The displayed *P*-value highlights the significant difference of the concerned means after applying an unpaired *t*-test.
- C Dose–response matrix to evaluate the synergy of VE-821 and SWG co-treatment. Synergy scores are shown using a continuous pseudocolor scale ranging from dark-yellow (= antagonism) to dark-magenta (= synergism). Synergy score values are indicated for each condition. RPE-1 cells were treated for 4 days with the indicated doses of VE-821 and SWG in 96-well plates. Cell viability was assessed using CellTiter-Glo Luminescent Cell Viability Assay and was normalized to untreated conditions. Matrix shows the mean of 4 independent experiments.
- D RPE-1 cells were grown with 10 μM BrdU in the culture medium for the last 16 h prior to further processing. Cells were then either mock-treated, or pretreated for 1 h with 500 nM of the ATM inhibitor (ATMi) AZD0156 or 10 nM of the specific OSBP1 inhibitor schweinfurthin G (SWG). Then, 200 μM CPT was added and cells were processed for BrdU detection (see [Materials and Methods](#)) at the indicated time points. **Left:** an illustrative image of BrdU-positive nuclei, indicated by yellow arrowheads. Scale bar is 15 μm . **Right:** the percentage of cells in the population whose nuclei were positive for BrdU was established by visual inspection of the acquired images. The graph shows the mean percentage out of three independent experiments and the error bars indicate their associated SEM. Unpaired *t*-tests were used to compare the potential differences of the means at each time point. Only the *P*-value for the one being significantly different is indicated.

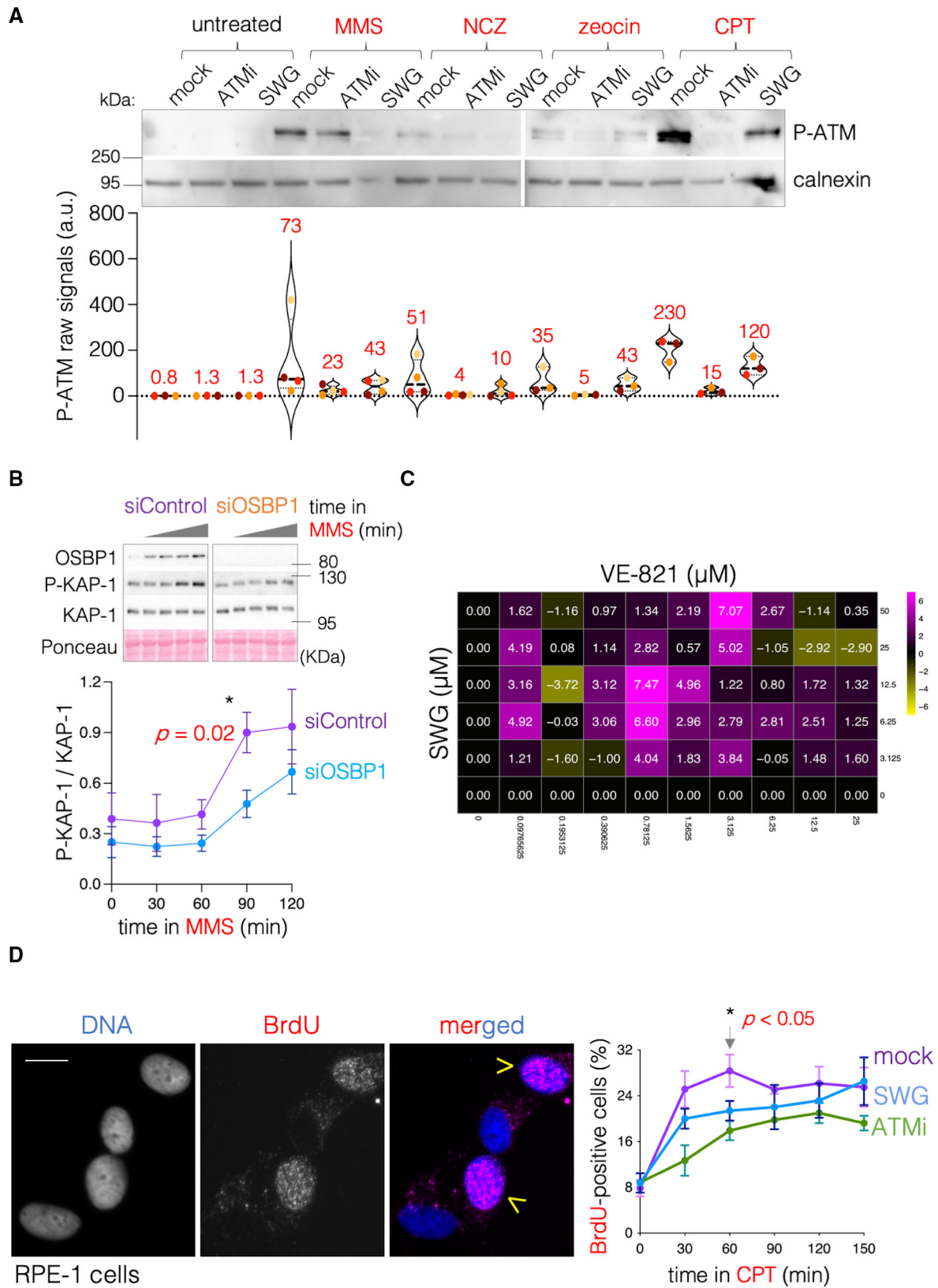
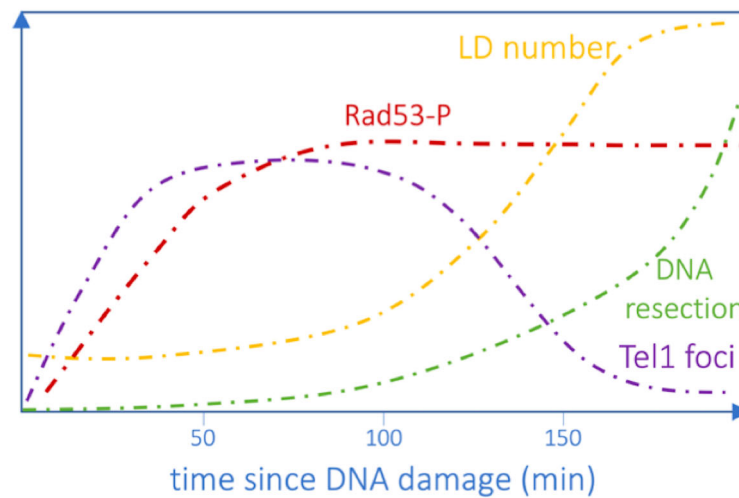


Figure 9.

A



B

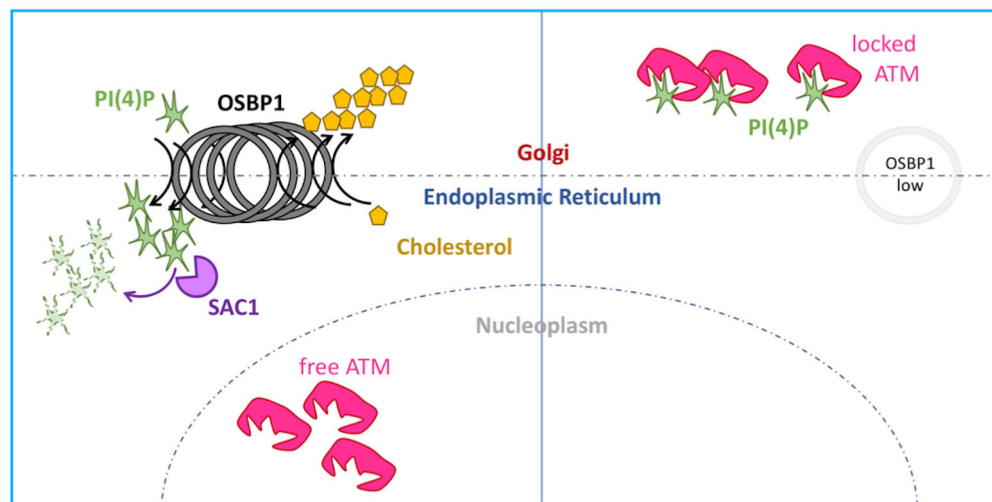


Figure 10. Models for Tel1/ATM regulation by the sterol/PI(4)P loop.

- A The kinetic analyses performed in this work allow us to propose that, in response to DNA DSBs, Tel1 foci (purple line) accumulate early, indicative of damage detection, shortly followed by the phosphorylation of Rad53 (red line), marker of downstream pathway activation. Presumably as an effect of this DDR activation, the storage of sterols within LD (yellow line) occurs at later stages, a process that is necessary to promote Tel1 foci (purple line) decline and subsequent engagement of downstream DNA long-range resection (green line). In situations where sterol removal from membranes is prevented, the higher basal levels of Tel1/ATM in the nucleus support a faster/more intense DDR activation kinetics.
- B The constitutive binding of ATM/Tel1 to PI(4)P takes place at the Golgi and limits the molecules of ATM/Tel1 that are available to operate in the nucleus. **Left:** conditions enhancing the activity of the OSBP1/Osh4 exchanger, such as elevated (chole)sterol levels in the ER or increased activity of the phosphatase SAC1/Sac1, promote PI(4)P extraction from the Golgi and its hydrolysis at the ER. This releases ATM/Tel1, which can then reach the nucleus and act in DNA-related transactions, such as DNA DSB signaling and telomere length maintenance. **Right:** low (chole)sterol availability in the ER, lack of PI(4)P hydrolysis in the absence of SAC1/Sac1, or OSBP1 inactivity cause PI(4)P accumulation in the Golgi, which sequesters ATM away from its nuclear functions.

An irreversibly anchored Lamin A destroys the integrity of the nuclear envelope, further leading to altered gene expression, DNA replication, and telomere maintenance, thus strongly activating the DDR and hampering downstream DNA repair (Gonzalo *et al.* 2017). In view of our work, these features and the lipodystrophic

phenotype become suddenly linked: the strong DDR activation would be permanently paralleled by sterol esterification and storage, which would override TAG storage. Consequently, TAG displacement may lead to their redistribution within the body and loss of adipocyte identity. In support of this idea, mutations in genes

related to genome integrity preservation, and which also elicit a strong DDR, such as in the Werner helicase, or in the SMC5/6 sumo ligase NSE2, also lead to lipodystrophy (Donadille *et al*, 2013; Payne *et al*, 2014), a fact that has remained puzzling since these genes are completely unrelated to the metabolism of lipids.

Concluding remarks

We uncover a link between two previously poorly connected research fields. This raises a myriad of issues. For example, it is generally believed that sterol esterification is activated mostly when transport mechanisms are saturated, thus making the level of free sterols in the ER reach a high concentration (Luo *et al*, 2020). We propose here that this process is actively instructed in response to DSBs, thus raising the need to unveil the DDR effectors in charge of LD formation. It would also be key to assess how and when LD are dismantled in order to respond to new waves of DNA damage.

The overall effects we report are mild given that the metabolism of sterols is finely controlled in a multilayered manner (Luo *et al*, 2020), thus permitting a limited window of experimental manipulation. Yet, our data unveil the existence of an evolutionarily conserved mechanism from yeast to human cells linking lipid biology and the response to DSBs. Crucially, the pharmacological manipulation of this mechanism allows us to explore new therapeutic interventions. Overall, this work paves the road for abundant, novel, and exciting research.

Materials and Methods

Reagents

Filipin (F4767, Sigma-Aldrich), avasimibe (PZ0190, Sigma-Aldrich), Nile Red (HY-D0718, CliniSciences), 5-fluoroorotic acid monohydrate (5-FOA, F595000, Toronto Research), oleic acid for *S. cerevisiae* cells (O1008, Sigma-Aldrich); oleic acid:BSA conjugate for human cells (O3008, Sigma-Aldrich), Hoechst (B2261, Sigma-Aldrich), methyl methanesulfonate (129925, Sigma-Aldrich), zeocin (R25001, ThermoFisher), nocodazole (M1404, Sigma-Aldrich), hydroxyurea (H8627, Sigma-Aldrich), camptothecin (C9911, Sigma-Aldrich), 3xFLAG peptide (F4799, Sigma-Aldrich), Fatty Acid-free BSA (A6003, Sigma-Aldrich), DAPI (D9542, Sigma-Aldrich), cOmplete protease inhibitor cocktail (11836170001, Roche), Halt Phosphatase inhibitor cocktail (78420 ThermoFisher) and ProLong (P36930, ThermoFisher), BrdU (5-Bromo-2'-deoxyuridine, B5002-1G, Sigma-Aldrich), AZD0156 (HY-100016-5 mg, CliniSciences), neocarzinostatin (NCZ, N9162-100UG, Sigma-Aldrich), VE-821 (HY-14731, CliniSciences), PIK93 (HY-12046, CliniSciences), and Crystal violet (V5265-250ML, Sigma-Aldrich). Schweinfurthin G (SWG) was a kind gift from Bruno Mesmin and Bruno Antonny. siControl was the universal negative control siRNA #1 (SIC001, Sigma-Aldrich), and siRNAs against ATM and OSBP1 were also from Sigma-Aldrich: siATM#1 (SASI_Hs01_00093615, 5'-CUUAGCAGGAGGUGUAAAU [dT][dT]-3'); siATM#2 (SASI_Hs01_00093616, 5'-CCCAUUACUAGA CUACGAA[dT][dT]-3'); siATM#3 (SASI_Hs01_00093617, 5'-GUUA CAACCAUACUAGA[dT][dT]-3'); siOSBP1#1 (SASI_Hs01_00068117, 5'-GAUAGAUCAGUCUGGCGAA[dT][dT]-3'); siOSBP1#2 (SASI_Hs01_00068118, 5'-CACAAUCGUACACAACAUU[dT][dT]-3'); siO

SBP1#3 (SASI_Hs01_00068119, 5'-CUUUGAGCUGGACCGAUUA[dT][dT]-3').

Antibodies

Anti-calnexin (610523, BD transduction Laboratories, WB at 1/1,000), anti-Rad53 (gift from C. Santocanele, WB at 1/3,000), anti-P-Thr68-CHK2 (2661S, Cell Signaling, WB at 1/1,000), antitotal CHK2 (05-649, Millipore, WB at 1/1,000), antitotal ATM (GTX132147, GenTex, IF at 1/200, PLA at 1/2,000), anti-P-Ser1981-ATM (4526, Cell Signaling, IF at 1/200, WB at 1/1,000), anti-FLAG (F3165, Sigma-Aldrich, WB at 1/3,000), anti-FLAG M2 affinity gel (A2220, Sigma-Aldrich), anti-ssDNA (Enzo; ALX-804-192-R200, used at 1/500), anti-PI4P (Z-P004; Echelon Biosciences, PLA at 1/2,000; IF at 1/1,000), anti-BrdU (Purified Mouse Anti-BrdU Clone 3D4, 15838318, FisherScientific, IF at 1/100), antitubulin (T5168, Sigma-Aldrich, WB at 1/3,000), anti-KAP-1 (BETA300-274A, Bethyl, WB at 1/2,000), anti-P-Ser824-KAP-1 (BETA300-767A, Bethyl, WB 1/2,000), anti-OSBP1 (HPA039227, Sigma-Aldrich, WB at 1/1,000), anti-CHK1 (SC8408, Santa Cruz, WB 1/500), anti-P-Ser317-CHK1 (2344S, Cell signaling, 1/1,000), anti-P-CHK1-Ser345 (2348S, Cell Signaling, WB at 1/2,000), anti-P-Ser139-H2AX (05-636, Sigma-Aldrich, IF at 1/500), anti-H3 (ab1791, Abcam, WB at 1/5,000), anti-GOLPH3 (SAB4200341, Sigma-Aldrich, IF at 1/300, WB at 1/2,000), and anti-TGN46 (AHP500G, Bio-Rad, IF at 1/100). Secondary antibodies for WB were goat anti-rabbit (A0545, Sigma-Aldrich) at 1/5,000 and rabbit anti-mouse (A9044, Sigma-Aldrich) at 1/5,000; for IF DyLight 488 donkey anti-rabbit (406404, Biolegend) at 1/500 and DyLight 649 goat anti-mouse (405312, Biolegend) at 1/500.

Saccharomyces cerevisiae cell culture and treatments

Cells were grown at 25°C in YEP medium supplemented with 2% glucose unless otherwise indicated. In experiments where a plasmid needed to be maintained, the cells were grown overnight in YNB lacking the relevant amino acid for selection, then diluted in the morning, and left to reach exponential phase in YEP medium supplemented with 2% glucose for approximately 4 h. For expression of constructs under the control of the *GAL1* promoter, cells were grown overnight in the appropriate medium +2% raffinose or +2% glycerol (when specified) and then induction was started by adding 2% galactose. All experiments were performed with asynchronous cultures of cells growing exponentially. For liquid culture time-course experiments, final concentrations of the drugs were as follows: 100 µg/ml zeocin, 0.1 M HU, 100 µM CPT, and 15 µg/ml nocodazole. The pretreatment with oleate in liquid cultures was done using a 0.05% concentration for 2 h. Strains used in this study are either shown in Appendix Table S1, or derived from crosses. Additionally, endogenous *PUS1* was N-terminally tagged with mCherry by *BglII*-linearizing then transforming YIplac211-mCherry-*PUS1* (Karanasios *et al*, 2013). Plasmids used in this study are shown in Appendix Table S2.

Human cell culture and treatments

The RPE-1 or Huh-7 cell lines used in this study were authenticated by ATCC STR profiling. They were seeded on p100 plates (dilution

1:7 from one confluent p100). After 2 days, medium was changed (at 37°C) and treatments were applied. RPE-1 were grown in DMEM (D5796-500ML, Sigma-Aldrich) and Huh-7 in DMEM+GlutaMAX (Gibco, 31966-021) supplemented with 10% FBS (S1810-500, Biowest) and 1% Pen/Strep (P0781, Sigma-Aldrich). At the end of the corresponding treatments, cells were collected for western blot or fixed for immunofluorescence with 4% PFA/PBS (20 min at room temperature) or cold methanol in the case of P-ATM experiments (chilled at -20°C; fixation for 10 min) and then washed once with PBS.

Transfections

Cells were seeded 24 h prior to transfection with XtremeGENE 360 (08724121001, Merck). Following the supplier's protocol, for plasmid transfection, 2 µl of the reagent was added per 1 µg of DNA in a 100 µl solution. For siRNA transfection, 7.5 µl of the reagent was combined with 40 nM siRNA in 6-well plate wells and left 28 or 72 h, respectively, prior to the intended experiment.

Treatments

DNA-damaging treatments were always applied for 2 h at a final concentration of 0.005% MMS, 10 µg/ml zeocin, and 120 ng/ml neocarzinostatin (NCZ). Also, due to a calculation mistake, we did our experiments with 200 µM camptothecin (CPT), which is a 100-fold higher dose than usually seen in the literature. Yet, at this high dose, cells were fit in the time frame of our experiments, probably because once CPT has trapped all topoisomerase-I molecules in the cell, further addition of the drug does not have any additional impact. We have repeated once more the experiments presented in Fig 9A and B with 2 µM CPT, and we have confirmed that the conclusions do not change. Pretreatments were done for 4 or 24 h with 60 µM oleate, as indicated, 2 h with 5 µM avasimibe, 4 h with 10 µM PIK93.

BrdU immunofluorescence detection

Cells were seeded on coverslips at a 50–60% confluency, and the next day BrdU was directly added at a final concentration of 10 µg/ml and incubated for 16 h. Cells were then pretreated with 500 nM AZD0156 for 1 h or 10 nM SWG for 2 h, or mock-treated, and then exposed to 200 µM CPT and coverslips retrieved at 0, 30, 60, 90, 120, or 150 min. Cells were then pre-extracted, fixed, and immunostained exactly as previously described (Mukherjee et al, 2015).

Dot blot to detect ssDNA

RPE-1 cells were seeded in p100 plates to reach 90% confluency the next day and then were incubated with 60 µM oleate (BSA) or 30 µM BSA (mock) for 2 h. 0.005% MMS was added, and cells were trypsinized and collected at the indicated times. Cell pellets were stored at -20°C. To extract genomic DNA (gDNA), cell pellets were incubated with lysis buffer (10 mM Tris pH 8; 1 mM EDTA; 0.5% SDS; 60 µg/ml Proteinase K (EU0090-C, Euromedex) overnight at 37°C). One volume of Phenol:Chloroform:Isoamyl Alcohol (25:24:1; P2069-400ML, Sigma-Aldrich) was added to the lysates, then transferred to Phase Lock Gel Tubes (733-2477, VWR), and centrifuged at

12,000 g for 5 min. The top layer was retrieved and incubated with 1 mg/ml (11508686, FisherScientific) 1 h at 37°C. gDNA phase was isolated using again 1 volume of Phenol:Chloroform:Isoamyl Alcohol (25:24:1) in Phase Lock Gel Tubes and centrifuged at 12,000 g for 5 min. gDNA was precipitated using 0.3 M NaOAc pH 5 and 2.4 volumes of ethanol 100% and centrifugation at 17,000 g for 15 min. gDNA was washed with 70% ethanol and resuspended in TE buffer (10 mM Tris pH 8; 1 mM EDTA). A Hybond-N+ membrane (GERPN203B, Sigma-Aldrich) was prehydrated with 6× SSC (0.9 M NaCl; 90 mM Trisodium citrate), and wells were washed with TE buffer. 1.5 µg of gDNA was dissolved in 250 µl TE buffer and loaded onto the membrane with the help of a Bio-Dot apparatus (Bio-Rad, 1706545) and a vacuum pump and then washed with 2× SSC. DNA was cross-linked to the membrane using 12 µJoules/cm² UV-C. The membrane was next blocked with 3% BSA/TBS-T for 1 h, incubated with anti-ssDNA at 1:500 in TBS-T/1% BSA/0.01% sodium azide overnight at 4°C, washed and further incubated with anti-mouse antibody at 1:5,000 in 5% milk/TBS-T for 45 min, and then developed using SuperSignal™ West Pico PLUS (ThermoScientific).

Proximity ligation assay

Cells were seeded on coverslips and, after the pertinent treatment, fixed with 4% PFA/PBS during 20 min at room temperature. Subsequently, every step took place in a humid chamber using the PLA reagents from Sigma-Aldrich. Cells were permeabilized with 0.5% Triton/PBS for 10 min and incubated with Blocking Solution from the Duolink *in situ* PLA kit (DUO92013) for 1 h. Primary antibodies (anti-PI(4)P and anti-ATM) were diluted at 1:2,000 in the Antibodies Diluent from the kit and incubated overnight at 4°C onto the coverslips. For technical controls, one of these primary antibodies was omitted at a time. PLA minus and plus probes (DUO92004 and DUO92002, Sigma-Aldrich) were next mixed and incubated in the Blocking Solution for 20 min as specified by the supplier, then added onto the coverslips, and incubated for 1 h at 37°C. Coverslips were washed twice with Buffer A (150 mM NaCl; 10 mM Tris; 0.05% Tween-20; pH 7.4), then incubated with Ligation Mix (1:40 ligase; 1:5 ligase buffer) 30 min at 37°C, washed again twice with Buffer A, and then incubated with Polymerization Mix (1:80 polymerase; 1:5 polymerase buffer) 1 h at 37°C. Last, coverslips were washed with Buffer B (100 mM NaCl; 200 mM Tris; pH 7.5) and then with 0.01× Buffer B. The coverslips were finally mounted with Duolink *in situ* Mounting Medium with DAPI (DUO82040) and then sealed with nail polish.

Crystal violet proliferation assay

RPE-1 and Huh-7 cells were seeded in 96-well plates at an initial number of 1,000, 2,000, or 4,000 cells per well (4 wells per initial seeding number). One independent plate was seeded per time point. Once cells were adhered, the specified treatments were applied and incubated for 1–6 days. Medium was changed, and all treatments were renewed at day 3. Every 24 h, one plate was washed twice with PBS, fixed with 50 µl of 4% PFA-PBS for 10 min at room temperature, stained with 80 µl of 0.1% crystal violet in water for 30 min at room temperature, and extensively washed with distilled water to eliminate the excess of dye. The water was removed, and cells were allowed to dry before solubilization with 200 µl of 10%

acetic acid. Absorbance was read at 570 nm with a Multiskan microplate reader (ThermoFisher). Crystal violet absorbance directly correlates with the number of living cells that remain attached to the plate. For day 0, one extra plate was seeded at the same time than the others but no treatments were added. This plate was fixed after 7 h following the same protocol to assess the initial number of cells per condition. Absorbance at 570 nm at each time point was normalized to the values from day 0 in order to calculate the proliferation rate.

Telomere length

It was measured by PCR after end labeling with terminal transferase (Forstemann *et al*, 2000; Teixeira *et al*, 2004). End-labeling reactions (40 μ l) contained 120 ng genomic DNA, x1 New England Biolabs™ Terminal Transferase Buffer, 1 mM dCTP, 4 units Terminal Transferase (New England Biolabs™) and were carried out at 37°C for 30 min followed by heat inactivation at 75°C for 10 min. 1/5th volume of 5 M NaCl, 1/80th volume of 1 M MgCl₂ and 1 volume of isopropanol were added to the reaction and DNA was precipitated by centrifugation at 17,000 g during 15 min. Precipitated DNA was resuspended in 40 μ l of ddH₂O. The end-labeled molecules were amplified by PCR using the primer 5'-GCGGATCCGGGGGGGGGGGGGGGGGG-3' and 5'-TGTGCTGGTGGGATTA-GAGTGGTAG-3' (X) and 5'-TTAGGGCTATGTAGAAGTGCTG-3' (Y'), respectively. PCR reactions (50 μ l) contained between 40 ng and 80 ng of DNA, 1 \times myTaq buffer, and primers 0.4 μ M each. Amplification was carried out with 5 U of MyTaq polymerase (BIO-21105, Meridian Biosciences). The conditions were 95°C, 5 min; followed by 35 cycles of 95°C, 1 min; 56°C (Y reaction)/60°C (X reaction), 20 s; and 72°C, 5 min. Reaction was ended with 5 min at 72°C. Samples were visualized in a 2% agarose gel containing 1 \times GelRed (BTM41003, Ozyme).

Immunofluorescence of human cells

Cells fixed on coverslips were washed once with PBS and permeabilized with 0.2% Triton/1 \times PBS for 10 min at room temperature and then saturated with 3% BSA/1 \times PBS for 30 min. Coverslips were incubated with primary antibodies diluted in 3% BSA/1 \times PBS for 90 min and then washed 3 times \times 10 min with 1 \times PBS under gentle shaking. Coverslips were further incubated with secondary antibodies diluted (1:500) in 3% BSA/1 \times PBS for 45 min while protecting them from light from this point on, then washed 3 \times 10 min with 1 \times PBS under gentle shaking, then incubated for 5 min with Hoechst (20 μ g/ml) diluted in H₂O, and washed three times with H₂O. Finally, coverslips were allowed to dry and mounted using ProLong and then left to dry overnight at room temperature in the darkness. For anti-PI(4)P detection, cells were fixed on coverslips with 4% PFA/1 \times PBS for 20 min, then washed once with 1 \times PBS and permeabilized with 100 μ M Digitonin/1 \times PBS for 5 min at room temperature, and then blocked with 3% BSA/1 \times PBS for 30 min. Coverslips were incubated with primary anti-PI(4)P and anti-GOLPH3 antibodies, diluted in 3% BSA/1 \times PBS for 1 h, and then washed three times with 1 \times PBS. Coverslips were further incubated with secondary antibodies diluted (1:500) in 3% BSA/1 \times PBS for 1 h while protecting them from light from this point on, then washed 3 \times 10 min with 1 \times PBS, then incubated for 10 min with DAPI (1 μ g/ml,

diluted in H₂O), and washed three times with H₂O. Finally, coverslips were allowed to dry and mounted using ProLong Gold Antifade and then left to dry overnight at room temperature in the darkness.

Western blot from human cells

All the samples were lysed with high-salt buffer (50 mM Tris pH 7.5, 300 mM NaCl, 1% Triton X-100, protease inhibitors (Roche), and phosphatase inhibitors Halt cocktail; 400 μ l per p100) for 10 min on ice with frequent vortexing. Samples were centrifuged for 10 min at 17,000 g at 4°C, and supernatants quantified using the Pierce™ BCA kit (10741395, ThermoFisher). For western blot, 20–30 μ g of whole-cell extracts were loaded onto home-made 10% acrylamide gels (1.5-mm-thick) and migrated 70 min at 40 mA per gel (migration buffer: 25 mM Tris, 200 mM Glycine, 0.1% SDS). The proteins were transferred to a nitrocellulose membrane for 2 h at 100 V in transfer buffer (25 mM Tris, 200 mM Glycine, 20% ethanol). For detection of P-ATM, whole-cell extracts were loaded on 3–8% acrylamide gradient gels (1.5-mm-thick) and migrated 90 min at 40 mA (migration buffer: 50 mM Tris, 50 mM Tricine, 0.1% SDS). The proteins were transferred to a nitrocellulose membrane overnight at 30 V in transfer buffer (25 mM Tris, 200 mM Glycine, 20% methanol).

FLAG-Tel1 immunoprecipitation

A 250 ml culture of cells bearing the pGAL1p-FLAG-TEL1 vector reaching a density of 7 \times 10⁶ cells/ml in YEP + 2% galactose was treated for 2 h with 100 μ g/ml zeocin at 25°C. The culture was centrifuged at 4,000 g for 3 min, and the supernatant was discarded. The cell pellet was washed once with Disruption Buffer (20 mM Tris-HCl pH7.9, 10 mM MgCl₂, 1 mM EDTA, 10% glycerol, 0.3 M ammonium sulfate, and protease inhibitor). The pellet was subsequently resuspended in 1 volume of Disruption Buffer and 2 volumes of precooled Glass Beads (0.4 mm diameter) and then subjected to 10 cycles of 30 s Cellbreaker/30 s on ice. Each sample was centrifuged briefly, and supernatants were retrieved and further centrifuged for 1 h at 12,000 g at 4°C. Supernatants were collected again and protein concentration estimated by the Bradford method. Next, 40 μ l of M2-agarose beads was centrifuged at 5,000 g during 30 s, supernatant was discarded, and then M2-beads were washed two times with 500 μ l of 1 \times TBS. 300 μ g of protein extract was added to the beads and diluted up to 1 ml using 1 \times TBS + protease inhibitor cocktail. The mixture was incubated at 4°C overnight on a rotating wheel. Next morning, the mixture was centrifuged at 5,000 g during 30 s, supernatant was removed (and saved as the “flowthrough fraction”), and the beads were washed three times with 500 μ l 1 \times TBS. 250 μ l of 3XFLAG peptide (stock at 1 mg/ml) was added and incubated for 30 min at 4°C on a rotating wheel. The mixture was centrifuged for 30 s at 5,000 g, and the supernatant recovered and used for lipid strip incubation and for western blot verification. The beads were boiled for 5 min using 30 μ l of 1 \times Laemmli buffer. These 30 μ l were used to evaluate by western blot the eventual, residual presence of FLAG-Tel1 onto the beads. For silver staining of proteins, samples were migrated in a 7.5% acrylamide gel (Bio-Rad, 4568023, USA) at 150 V for 45 min. Then, the gel was treated with and according to SERVA Silver Staining kit for SDS-PAGE (SERVA Electrophoresis GmbH, 35077, Germany),

performing the fixation step overnight and the developing one for 5 min.

Western blot from *S. cerevisiae* cells

For the regular detection of Rad53, approximately 5×10^8 cells were collected at each relevant time point and washed with 20% trichloroacetic acid to prevent proteolysis and then resuspended in 200 μ l of 20% trichloroacetic acid at 4°C. The same volume of glass beads was added, and cells were disrupted by vortexing for 10 min. The resulting extract was spun for 10 min at 1,000 g also at room temperature and the resulting pellet resuspended in 200 μ l of Laemmli buffer. Whenever the resulting extract was yellow-colored, the minimum necessary volume of 1 M Tris base (noncorrected pH) was added till blue color was restored. Then, water was added till a final volume of 300 μ l was reached. These extracts were boiled for 10 min and clarified by centrifugation as before; 10–15 μ l of this supernatant was loaded onto a commercial 3–8% acrylamide gradient gel (Bio-Rad) and migrated 70 min at 150 V to separate Rad53 isoforms, and then proteins transferred to a nitrocellulose membrane. For improved phospho-isoform detection, home-made gels were casted using the following recipe (running gel 10%, per 10 ml: 2.5 ml 40% acrylamide; 0.65 ml 2% bis-acrylamide; 2.5 ml 1.5 M Tris–HCl pH8.8; 100 μ l 10% SDS; 75 μ l 10% APS; 7.5 μ l TEMED; stacking gel, per 5 ml: 0.625 ml 40% acrylamide; 0.35 ml 2% bis-acrylamide; 0.65 ml 1 M Tris–HCl pH6.8; 50 μ l 10% SDS; 50 μ l 10% APS; 5 μ l TEMED), and samples migrated in Tris–Glycine buffer at 90 V for 4 h. Detection by immunoblotting was performed with anti-Rad53 antibody, a kind gift from Dr. C. Santocanele, Galway, Ireland. To detect FLAG-Tel1, samples were loaded onto a commercial 7.5% acrylamide gradient gel (Bio-Rad) and migrated 60 min at 60 mA, and then proteins transferred to a nitrocellulose membrane overnight at 4°C.

Lipid membrane hybridization

A commercially available membrane on which 100 pmol of each of the lipids of interest had been spotted (P-6002 or P-6001, Echelon Biosciences) was blocked using TBS-Tween_{0.1%} supplemented with 3% fatty acid-free BSA during 1 h in the dark at room temperature. 5/6th of the M2-immunoprecipitated FLAG-Tel1 preparation were incubated on the lipid membrane in a final volume of up to 1 ml (TBS-Tween_{0.1%} supplemented with proteases inhibitor) sealed in a plastic bag and then incubated 4°C in the dark under soft shaking. The following day, the lipid membrane was washed three times in TBS-Tween_{0.1%} (10 min each wash) and the anti-FLAG antibody incubated during 3 h at 4°C in the dark. All subsequent steps were performed as for regular western blot except that all incubations were done in the dark.

Liposome assays

20 μ l of commercial liposomes (PI(4)P PolyPIPosome, 117Y-P004; and control PolyPIPosomes, Y-0000; Echelon Biosciences) was incubated with purified FLAG-Tel1 in floatation buffer (20 mM PIPES–NaOH pH6.5, 100 mM NaCl, 1 mM EDTA) for 10 min at room temperature. 60% sucrose prepared in floatation buffer was added to the emulsion to obtain a final sucrose concentration of 30%. 450 μ l

of this suspension was loaded at the bottom of an ultracentrifuge tube and overlaid with a discontinuous sucrose gradient consisting of 300 μ l 20% sucrose (in floatation buffer), 300 μ l of 10% sucrose (in floatation buffer), and 100 μ l of floatation buffer alone. Samples were centrifuged at 214,000 g in a Beckman swing-out rotor (TLS55) for 80 min at 8°C. Three fractions were carefully collected with a Hamilton syringe from the bottom with the following volumes: 450, 620, and 80 μ l. Every fraction was concentrated with 600 μ l of methanol and mixed, and then 150 μ l of chloroform was added and then vortexed. 450 μ l of water was added and then vortexed. Fractions were centrifuged at 13,000 g for 5 min. The upper phase was removed from samples, being careful to not remove the white disk. 600 μ l of methanol was added, mixed by inversion three times and then centrifuged at 13,000 g for 5 min. Supernatants were removed, samples dried, and then, 30 μ l of Laemmli buffer was added and used for electrophoresis and western blot.

Comet assays

Human cells in culture treated as specified were retrieved and rinsed with 1× PBS after quick trypsinization. 30 μ l from a 10⁵ cells/ml suspension was mixed with 270 μ l of molten 1% Low Melting Agarose, both in 1× PBS, and then 30 μ l of this mix poured onto 1% agarose precoated coverglass, and directly covered by a coverslip. After 10 min of polymerization at 4°C, the coverslip is removed and the coverglass is immersed 30 min at 4°C in Lysis Solution (2.5 M NaCl, 100 mM EDTA, 10 mM Tris–HCl, 1% [wt/vol] sodium lauryl sarcosine, 1% [vol/vol] Triton X-100, pH 10) and then immersed 20 min at RT in Unwinding Solution (200 mM NaOH, 1 mM EDTA pH 10). Electrophoresis is then run at 21 V 30 min in Alkaline Electrophoresis Buffer (200 mM NaOH, 1 mM EDTA pH8) in a CometAssay® Electrophoresis System. Slides are then rinsed 2 × 5 min with H₂O and 1 × 5 min with 70% EtOH, dried 30 min at 37°C, DNA dyed with SYBR® Gold 1:10,000 for 30 min, rinsed with H₂O, and completely dried at 37°C. Comets are visualized under the fluorescence microscope as indicated in the image acquisition section. Analysis is performed in a semiautomated manner, using TriTek CometScore 2.0.0.38 software. The resulting Olive moment data are plotted in GraphPad Prism and correspond to the percentage of in the tail multiplied by the distance between the intensity-weighted centroids of head and tail.

Synergy matrices

For evaluation of VE-821 and SWG synergy, RPE-1 cells were seeded in 96-well flat-bottom plates (1,000 cells per well in 100 μ l of DMEM +10% FBS + P/S). After 4 h, when cells were attached to the plate, increasing concentrations of each single drug were combined with all concentrations of the other drug so all possible combinations were evaluated, where VE-821: 0.098–25 μ M; SWG: 3.125–50 nM. Two identical plates were treated and analyzed per experiment. Four days after treatment, cell growth was evaluated with CellTiter-Glo (CTG) Luminescent Assay (G7573, Promega) according to the manufacturer's protocol and luminescence was measured using a Centro LB 960 luminometer (Berthold Technologies, Bad Wildbad, Germany). The effect of drug combination (synergy, antagonism or

addition) was calculated with Bliss equation using the R package “SynergyFinder.”

Cell fractionation assays

Exponentially growing RPE-1 cells were treated or not for 2 h with 10 µg/ml zeocin. Cells were collected and lysed directly with Laemmli buffer (1×) for whole-cell extract (WCE) preparation. For cytoplasm fractions preparation, cells were resuspended in cold sucrose buffer (10 mM HEPES pH 7.9, 0.34 M sucrose, 3 mM CaCl₂, 2 mM MgAc, 0.1 mM EDTA, 0.5% NP40, Halt Protease And Phosphatase Inhibitor Cocktail, EDTA-Free [ref. 1861282 Thermo Scientific]), passed at least five times through 200 µl tips, incubated under rotation for 10 min at 4°C, and centrifuged at 3,900 g for 20 min at 4°C, and the supernatants were collected as cytoplasmic fractions. The resulting pellets contained the nuclei, which were directly lysed with Laemmli buffer (1×).

Recombination analyses

The genome-integrated system *leu2-k::ADE2::URA3::leu2-k* (Aguilera & Klein, 1990) allows the analysis of the frequency of homologous recombination, mostly that occurring through single-strand annealing. The loss of the *URA3* marker, which can be selected for in plates containing 5-FOA (0.5 g/l), permits the calculation of the recombination frequency. For each recombination test, cells were streaked onto plates containing either 7.5 µg/ml zeocin or not, and either 0.05% oleate or not, as indicated, and incubated for 3 days at 26°C. From each plate, six isolated colonies were resuspended in 1 ml sterile water each, dilutions of each tube done and dilutions from 1/4th to 1/400th seeded on 5-FOA-containing plates in order to select for recombinants, and one dilution 1/40,000th seeded on YPD plates to count the total number of cells, finally allowing to calculate the recombination frequencies. For every six frequencies derived from six colonies, one median frequency was calculated (= 1 experiment). The displayed results for each condition represent the mean frequency out of the median of at least three independent experiments.

Pulsed-field gel electrophoresis

Human cells in culture treated as indicated were retrieved in 1× PBS and counted. Approximately 6 × 10⁵ cells were used per agarose plug. Typically, each plug was created by mixing very smoothly 50 µl of this cell suspension and 50 µl of low melting point agarose pre-prepared at 1% in 1× PBS, and pouring the mix into a disposable (yet re-used) plug mold (Bio-Rad Laboratories). Plugs were allowed to solidify for 30 min at room temperature and 30 min at 4°C. They were then incubated (typically 5 plugs of each condition in 2 ml of buffer) in lysis buffer (100 mM EDTA, 1% [wt/vol] sodium lauryl sarcosine, 0.2% [wt/vol] sodium deoxycholate, and 1 mg/ml proteinase K) at 37°C for 24 h. Plugs were then washed five times in 5 ml of 20 mM Tris-HCl, pH 8.0, 50 mM EDTA and were then ready to be loaded onto an agarose gel. Electrophoresis was performed for 21 h at 14°C in 0.9% (wt/vol) Pulse Field Certified Agarose (Bio-Rad Laboratories) in exactly 2.4 l of 0.5× Tris-borate/EDTA buffer in a Rotaphor apparatus (Biometra, Analytik Jena) with the following protocol: block I: 9 h, 120° included angle,

5.5 V/cm, 30 to 18-s switch; block II: 6 h, 117° included angle, 4.5 V/cm, 18 to 9-s switch; block III: 6 h, 112° included angle, 4.0 V/cm, 9 to 5-s switch. The gel was then stained with ethidium bromide, photographed and well and in-gel signals analyzed using ImageJ. Relative DSB levels were calculated by dividing the in-gel signal between the total lane signal and expressed as a percentage.

Analysis of DNA content by flow cytometry in *S. cerevisiae*

430 µl of culture samples at 10⁷ cells/ml were diluted in 1 ml of 100% ethanol. Cells were centrifuged for 1 min at 16,000 g and resuspended in 50 mM Na-Citrate buffer containing 5 µl of RNase A (10 mg/ml, Euromedex, RB0474) for 2 h at 50°C. 6 µl of Proteinase K (Euromedex, EU0090-C) was added for 1 h at 50°C. Cell aggregates of cells were dissociated by sonication (one 3 s-pulse at 50% potency in a Vibracell 72405 Sonicator). 20 µl of this cell suspension was incubated with 200 µl of 50 mM Na-Citrate buffer containing 4 µg/ml Propidium Iodide (Fisher Scientific). Data were acquired and analyzed using a Novocyte Express (Novocyte). At least three independent biological replicates, each counting at least 10,000 cells per sample and condition, were analyzed.

Cytometry for human cells

RPE-1 and Huh-7 cells were mock-treated (30 µM BSA) or treated with oleate (60 µM) for 2 h, followed by addition or not of zeocin (10 µg/ml) for 2 extra hours. BrdU (10 µg/ml) was added to all samples during the last 2 h of treatment. One extra well of mock-treated cells without BrdU was added and processed as the rest of the samples to be used as negative control for FACS analysis. BrdU detection was performed using the BD Pharmingen™ BrdU Flow Kit (Cat. No. 552598) according to the manufacturer's instructions. More in detail, cells were trypsinized and counted, and 0.5 million cells per condition were washed once with 1 ml PBD, subsequently fixed and permeabilized with 100 µl BD Cytofix/Cytoperm Buffer for 15 min at 4°C, then washed with 1 ml of 1× BD Perm/Wash Buffer, further permeabilized with 100 µl of BD Cytoperm Permeabilization Buffer Plus for 10 min at 4°C, washed with 1 ml of 1× BD Perm/Wash Buffer, refixed again with 100 µl BD Cytofix/Cytoperm Buffer for 10 min at 4°C, washed with 1 ml of 1× BD Perm/Wash Buffer, resuspended in 100 µl of DNase (diluted to 300 µg/ml in PBS) for 1 h at 37°C, washed with 1 ml of 1× BD Perm/Wash Buffer, incubated with APC tagged anti-BrdU diluted in BD Perm/Wash buffer (1:50) for 20 min at RT, washed with 1 ml of 1× BD Perm/Wash Buffer, DNA was stained with DAPI (20 µg/ml diluted in BD Perm/Wash Buffer) for 10 min at 4°C, washed with 1 ml of 1× BD Perm/Wash Buffer, and resuspended in 250 µl of PBS. Cells were then analyzed by cytometry and assigned to each phase of the cell cycle (subG1: less than 1C DNA content, G1: 1C DNA content and BrdU–, S: BrdU+, G2: 2C DNA content and BrdU–). Graphs show the mean of two independent experiments.

DSB end resection assay

DSB end resection was analyzed in JKM139 (provided by J. Haber, Brandeis University, Waltham, USA)-derivative strains. Overnight mid-log cultures in YEP medium containing 2% raffinose at 1 × 10⁷ cells/ml were supplemented with 2% galactose to induce

HO-dependent cleavage. 50 ml of cells was recovered at each time point, and genomic DNA was extracted from cell pellets by vortexing with acid-washed glass beads in a solution containing 200 μ l of phenol:chloroform:isoamyl alcohol (25:24:1) and 200 μ l of the extraction buffer containing 2% Triton X-100, 1% SDS, 100 mM NaCl, 10 mM Tris pH 8.0, 1 mM EDTA. The DNA-containing aqueous phase was recovered and precipitated with ethanol. Purified DNA was treated with RNase A and digested with *SspI* restriction enzyme overnight at 37°C. DNA fragments were then separated by urea-agarose gel electrophoresis in denaturing conditions for 10 h at 150 V. The gel was subsequently transferred to a GeneScreen Plus membrane (Perkin Elmer), which was hybridized with a radioactive probe corresponding to the distal side of the HO cut. We generated the probe by PCR using the following primers HO_probe_JKM139_F 5'-CCCTGGTTTTGGTTTTGTAGAGTGG-3' and HO_probe_JKM139_R 5'-GAAACACCAAGGGAGAGAAGAC-3'. Radioactive signals were detected using a PhosphorImager (Typhoon IP, GE), and quantitative analysis of DSB resection was performed with the ImageJ software by calculating the ratio of band intensities for ssDNA relative to the HO-cut band. Three independent biological replicates were performed.

Microscopy analyses and image acquisition

Images of fixed human cells were acquired using an ApoTome-equipped microscope (Zeiss). ApoTome technology allows the acquisition of optical sections free of scattered light in order to analyze one focal plane, which allows higher resolution than wide-field microscopy. Filipin staining was achieved by incubating previously PFA-fixed cells in PBS with 25 μ g/ml filipin for 2 h, at room temperature and in the dark, followed by PBS washes. Detection was carried out in the UV range (360/460 nm). For *S. cerevisiae* cells, 1 ml of the culture of interest was centrifuged at each relevant time point of the experiment, the excess supernatant thrown away and the pellet resuspended in the remaining \approx 50 μ l. 3 μ l of this cell suspension was directly mounted on a coverslip for immediate imaging of the pertinent fluorescently tagged protein signals. For visualizing LD in human cells, Nile Red was added to the living cells at a final concentration of 0.5 μ g/ml during the last 10 min prior to fixation. To dye LD in *S. cerevisiae* cells using Nile Red, 1 μ l of a 1 mg/ml stock was added and mixed to the \approx 50 μ l centrifuged pellet (with residual medium) prior to mounting. 3 μ l of living *S. cerevisiae* cells was deposited between a coverslip and a slide and directly imaged. The imaging of living *S. cerevisiae* cells was achieved using a Zeiss Axioimager Z2 microscope controlled either by ZEN or by Metamorph softwares.

Quantifications, plots, and statistical analyses

Quantifications in this study were not subjected to blinding. However, different experimenters quantified similar data to limit bias. Quantification of the number of LD *per S. cerevisiae* cell, of repair foci per cell, of the percentage of cells in the population displaying foci, BrdU-positive cells, or deployed OSBP1 biosensor signals was achieved by visual inspection and counting by the experimenter. Quantification of the number of P-ATM-positive cells was achieved by a combined ImageJ macro-assisted detection of positive signals above a given threshold, and further validation and manual

counting of positive cells by the experimenter. Proximity Ligation Assay signals were detected using an ImageJ macro subtracting the background by rolling 30 pixels, setting the threshold level between 700 and 65,535, applying "Watershed" to the mask, and then analyzing particles whose size is between 0 and 30,000 pixels². The integrated density from those signals per image was retrieved and divided by the number of nuclei in the picture, thus yielding the mean integrated density per image. Each value obtained this way was used to plot a single dot in the graphs shown in the experiments. Raw signals from membranes (ssDNA, P-ATM, P-CHK2, Rad53, FLAG, and PFGE-derived ethidium bromide signals) were quantified for their raw intensity using nonsaturated tif images and the "Analyze > Gel" tool from the ImageJ software and directly plotted without any manipulation. To create the in-gel molecules signal plots presented in Fig 4C and D, a line was drawn through the signals in ImageJ, the pixel intensity along the line drawn with the command "k," and the associated values exported. GraphPad Prism (version 5 or version 9) was used to plot all the graphs and to statistically analyze the data. For statistical analyses, two-sided t-tests or one-way ANOVA tests were applied, depending on the nature of the comparison. These parametric tests were chosen since the concerned populations were means of means; thus, the central limit theorem applies.

Data availability

All figure source data can be found in BioStudies (Sarkans *et al*, 2018) under the S-BST1043 accession number. Reporting guidelines used to support this study follow the exigences of the Author Guidelines specified by EMBO Press.

Expanded View for this article is available [online](#).

Acknowledgments

We are very grateful to Vincent Géli for the Rfa1-CFP-tagged strain; Corrado Santocane for the anti-Rad53 antibody; Zvulun Elazar for *steΔ*, *tagΔ*, and *yeh2Δ* strains; Katsunori Sugimoto for the *pGAL1p-FLAG-TEL1* vector; Michael Lisby for the original Rad52-YFP strain; Christopher Beh for the *sac1Δ* strain and the vector to overexpress Osh4; Bruno Mesmin and Bruno Antony for the gift of *schweinfurthin G*; Symeon Siniosoglou for the Ylplac211-mcherry-Pus1 vector; Andrés Aguilera for the *leu2k::ADE2-URA3::leu2k*-bearing and *rad3-102* strains; Jim Haber for the JKM179 strain to study resection; Matteo Bonazzi for the OSBP1-detecting biosensor and Urszula Hibner and Krzysztof Rogowski for the gift of Huh-7 and RPE-1 cells, respectively. We are very thankful to Jérôme Moreaux for supporting S.O. during the execution of this project. We thank Simonetta Piatti for sharing with us the recipe for high-resolution gels of phosphorylated isoforms. We acknowledge the imaging facility MRI, a member of the national infrastructure France-BioImaging supported by the French National Research Agency (ANR-10-INBS-04, Investissements d'avenir). We also thank the joint IGMM-CRBM "yeast media and technologies service" for providing us with ready-to-use media. SO was supported by a postdoctoral grant from La Ligue contre le Cancer. SK was supported by a SIRIC Montpellier Cancer Grant INCa_Inserm_DGOS_12553. AC and PP were supported by the MSDAvenir fund. The work in MM-C's laboratory was supported by the ATIP-Avenir program, La Ligue contre le Cancer, l'Institut National du Cancer (PLBIO19-098 INCA_13832), and the Agence Nationale Recherche (ANR-21-CE12-0004-01), France.

Author contributions

Sara Ovejero: Conceptualization; formal analysis; validation; investigation; methodology; writing – review and editing. **Sylvain Kumanski:** Data curation; formal analysis; validation; investigation; visualization; methodology; writing – review and editing. **Caroline Soulet:** Data curation; formal analysis; validation; investigation; visualization; methodology; writing – review and editing. **Julie Azarli:** Investigation. **Benjamin Pardo:** Formal analysis; investigation; methodology; writing – original draft; writing – review and editing. **Olivier Santt:** Investigation; methodology; writing – review and editing. **Angelos Constantinou:** Funding acquisition; writing – review and editing. **Philippe Pasero:** Funding acquisition; writing – review and editing. **María Moriel-Carretero:** Conceptualization; data curation; formal analysis; supervision; funding acquisition; validation; investigation; visualization; methodology; writing – original draft; project administration; writing – review and editing.

Disclosure and competing interests statement

The authors declare they have no conflict of interest.

References

- Abramczyk H, Surmacki J, Kopeć M, Olejnik AK, Lubecka-Pietruszewska K, Fabianowska-Majewska K (2015) The role of lipid droplets and adipocytes in cancer. Raman imaging of cell cultures: MCF10A, MCF7, and MDA-MB-231 compared to adipocytes in cancerous human breast tissue. *Analyst* 140: 2224–2235
- Aguilera A, Klein HL (1990) HPR1, a novel yeast gene that prevents intrachromosomal excision recombination, shows carboxy-terminal homology to the *Saccharomyces cerevisiae* TOP1 gene. *Mol Cell Biol* 10: 1439–1451
- Ahmad F, Patrick S, Sheikh T, Sharma V, Pathak P, Malgulwar PB, Kumar A, Joshi SD, Sarkar C, Sen E (2017) Telomerase reverse transcriptase (TERT) – enhancer of zeste homolog 2 (EZH2) network regulates lipid metabolism and DNA damage responses in glioblastoma. *J Neurochem* 143: 671–683
- Alabert C, Bianco JN, Pasero P (2009) Differential regulation of homologous recombination at DNA breaks and replication forks by the Mrc1 branch of the S-phase checkpoint. *EMBO J* 28: 1131–1141
- Alvira D, Yeste-Velasco M, Folch J, Casadesus G, Smith MA, Palla M, Camins A (2007) Neuroprotective effects of Caffeine Against complex I inhibition–Induced Apoptosis are mediated by inhibition of the atm/PS3/E2F-1 path in Cerebellar Granule neurons. *J Neurosci Res* 3253: 3244–3253
- Antonny B, Bigay J, Mesmin B (2018) The oxysterol-binding protein cycle: burning off PI(4)P to transport cholesterol. *Annu Rev Biochem* 87: 809–837
- Aymard F, Aguirrebengoa M, Guillou E, Javierre BM, Bugler B, Arnould C, Rocher V, Iacovoni JS, Biernacka A, Skrzypczak M et al (2017) Genome-wide mapping of long-range contacts unveils clustering of DNA double-strand breaks at damaged active genes. *Nat Struct Mol Biol* 24: 353–361
- Bakkenist CJ, Kastan MB (2003) DNA damage activates ATM through intermolecular autophosphorylation and dimer dissociation. *Nature* 421: 499–506
- Beh CT, Rine J (2004) A role for yeast oxysterol-binding protein homologs in endocytosis and in the maintenance of intracellular sterol-lipid distribution. *J Cell Sci* 117: 2983–2996
- Beh CT, McMaster CR, Kozminski KG, Menon AK (2012) A detour for yeast oxysterol binding proteins. *J Biol Chem* 287: 11481–11488
- Beller M, Thiel K, Thul PJ, Jäckle H (2010) Lipid droplets: a dynamic organelle moves into focus. *FEBS Lett* 584: 2176–2182
- Beyer T, Weinert T (2014) Mec1 and Tel1: an arresting dance of resection. *EMBO J* 33: 176–178
- Bozza PT, Viola JPB (2010) Lipid droplets in inflammation and cancer. *Prostaglandins Leukot Essent Fatty Acids* 82: 243–250
- Chen M, Choi S, Wen T, Chen C, Thapa N, Lee JH, Cryns VL, Anderson RA (2022) A p53–phosphoinositide signalosome regulates nuclear AKT activation. *Nat Cell Biol* 24: 1099–1113
- Choi S, Chen M, Cryns VL, Anderson RA (2019) A nuclear phosphoinositide kinase complex regulates p53. *Nat Cell Biol* 21: 462–475
- Clémenson C, Marsolier-Kergoat MC (2009) DNA damage checkpoint inactivation: adaptation and recovery. *DNA Repair* 8: 1101–1109
- Clerici M, Mantiero D, Lucchini G, Longhese MP (2005) The *Saccharomyces cerevisiae* Sae2 protein promotes resection and bridging of double strand break ends. *J Biol Chem* 280: 38631–38638
- Clerici M, Trovesi C, Galbiati A, Lucchini G, Longhese MP (2014) Mec1/ATR regulates the generation of single-stranded DNA that attenuates Tel1/ATM signaling at DNA ends. *EMBO J* 33: 198–216
- Coiffard J, Santt O, Kumanski S, Pardo B, Moriel-Carretero M (2021) A CRISPR-Cas9-based system for the dose-dependent study of 4 DNA double strand breaks sensing and repair. *bioRxiv* <https://doi.org/10.1101/2021.10.21.465387> [PREPRINT]
- Connerth M, Czabany T, Wagner A, Zellnig G, Leitner E, Steyrer E, Daum G (2010) Oleate inhibits sterol ester synthesis and causes liposensitivity in yeast. *J Biol Chem* 285: 26832–26841
- Currie E, Schulze A, Zechner R, Walther TC, Farese RV (2013) Cellular fatty acid metabolism and cancer. *Cell Metab* 18: 153–161
- Donadille B, D'Anella P, Auclair M, Uhrhammer N, Sorel M, Grigorescu R, Ouzounian S, Cambonie G, Boulot P, Laforêt P et al (2013) Partial lipodystrophy with severe insulin resistance and adult progeria Werner syndrome. *Orphanet J Rare Dis* 8: 106
- Edifizi D, Nolte H, Babu V, Castells-Roca L, Mueller MM, Brodesser S, Krüger M, Schumacher B (2017) Multilayered reprogramming in response to persistent DNA damage in *C. elegans*. *Cell Rep* 20: 2026–2043
- Fáberová V, Kalasová I, Krausová A, Hozák P (2020) Super-resolution localisation of nuclear PI(4)P and identification of its interacting proteome. *Cell* 9: 1–17
- Ferrari E, Bruhn C, Peretti M, Cassani C, Carotenuto WV, Elgandy M, Shubassi G, Lucca C, Bermejo R, Varasi M et al (2017) PP2A controls genome integrity by integrating nutrient-sensing and metabolic pathways with the DNA damage response. *Mol Cell* 67: 266–281
- Forstemann K, Hoss M, Lingner J (2000) Telomerase-dependent repeat divergence at the 3' ends of yeast telomeres. *Nucleic Acids Res* 28: 2690–2694
- García M, Kumanski S, Elías-Villalobos A, Cazevielle C, Soulet C, Moriel-Carretero M (2022) Nuclear ingress of cytoplasmic bodies accompanies a boost in autophagy. *Life Sci Alliance* 5: e202101160
- Geuting V, Reul C, Löbrich M (2013) ATM release at resected double-strand breaks provides heterochromatin reconstitution to facilitate homologous recombination. *PLoS Genet* 9: 1–14
- Gobbini E, Cesena D, Galbiati A, Lockhart A, Longhese MP (2013) Interplays between ATM/Tel1 and ATR/Mec1 in sensing and signaling DNA double-strand breaks. *DNA Repair* 12: 791–799
- Gonzalo S, Krienkamp R, Askjaer P (2017) Hutchinson-Gilford progeria syndrome: a premature aging disease caused by LMNA gene mutations. *Ageing Res Rev* 33: 18–29
- de Gonzalo-Calvo D, López-Vilaró L, Nasarre L, Perez-Olabarria M, Vázquez T, Esquin D, Badimon L, Barnadas A, Lerma E, Llorente-Cortés V (2015) Intratumor cholesterol ester accumulation is associated with human

- breast cancer proliferation and aggressive potential: a molecular and clinicopathological study. *BMC Cancer* 15: 460
- Greenwell PW, Kronmal SL, Porter SE, Gassenhuber J, Obermaier B, Petes TD (1995) TEL1, a gene involved in controlling telomere length in *S. cerevisiae*, is homologous to the human ataxia telangiectasia gene. *Cell* 82: 823–829
- Halazonetis TD, Gorgoulis VG, Bartek J (2008) An oncogene-induced DNA damage model for cancer development. *Science* 319: 1352–1355
- Hammond GRV, Schiavo G, Irvine RF (2009) Immunocytochemical techniques reveal multiple, distinct cellular pools of PtdIns4P and PtdIns(4,5)P₂. *Biochem J* 422: 23–35
- Hirano Y, Fukunaga K, Sugimoto K (2009) Rif1 and Rif2 inhibit localization of Tel1 to DNA ends. *Mol Cell* 33: 312–322
- Hunter T (1995) When is a lipid kinase not a lipid kinase? When it is a protein kinase. *Cell* 83: 1–4
- Ivanova T, Maier M, Missarova A, Ziegler-Birling C, Dam M, Gomar-Alba M, Carey LB, Mendoza M (2020) Budding yeast complete DNA synthesis after chromosome segregation begins. *Nat Commun* 11: 1–13
- Kanagavijayan D, Rajasekharan R, Srinivasan M (2015) Yeast MRX deletions have short chronological life span and more triacylglycerols. *FEMS Yeast Res* 16: 1–14
- Karanasios E, Barbosa AD, Sembongi H, Mari M, Han GS, Reggiori F, Carman GM, Sinioglou S (2013) Regulation of lipid droplet and membrane biogenesis by the acidic tail of the phosphatidate phosphatase Pah1p. *Mol Biol Cell* 24: 2124–2133
- Klermund J, Bender K, Luke B (2014) High nutrient levels and torc1 activity reduce cell viability following prolonged telomere dysfunction and cell cycle arrest. *Cell Rep* 9: 324–335
- Köffel R, Tiwari R, Falquet L, Schneider R (2005) The *Saccharomyces cerevisiae* YLL012/YEH1, YLR020/YEH2, and TGL1 genes encode a novel family of membrane-anchored lipases that are required for sterol ester hydrolysis. *Mol Cell Biol* 25: 1655–1668
- Kousholt AN, Fugger K, Hoffmann S, Larsen BD, Menzel T, Sartori AA, Sørensen CS (2012) CtlP-dependent DNA resection is required for DNA damage checkpoint maintenance but not initiation. *J Cell Biol* 197: 869–876
- Krahmer N, Farese RV, Walther TC (2013) Balancing the fat: lipid droplets and human disease. *EMBO Mol Med* 5: 973–983
- Kruman II, Wersto RP, Cardozo-Pelaez F, Smilenov L, Chan SL, Chrest FJ, Emokpae R, Gorospe M, Mattson MP (2004) Cell cycle activation linked to neuronal cell death initiated by DNA damage. *Neuron* 41: 549–561
- Lahiri S, Toulmay A, Prinz WA (2015) Membrane contact sites, gateways for lipid homeostasis. *Curr Opin Cell Biol* 33: 82–87
- Leber R, Zinser E, Hrstnik C, Paltauf F, Daum G (1995) Export of sterol esters from lipid particles and release of free sterols in the yeast, *Saccharomyces cerevisiae*. *Biochim Biophys Acta Biomembranes* 1234: 119–126
- Lee Y, McKinnon PJ (2000) ATM dependent apoptosis in the nervous system. *Apoptosis* 5: 523–529
- Lee JH, Paull TT (2005) ATM activation by DNA double-strand breaks through the Mre11-Rad50-Nbs1 complex. *Science* 308: 551–554
- Lee SE, Pelliccioli A, Demeter J, Vaze MP, Gasch AP, Malkova A, Brown PO, Botstein D, Stearns T, Foiani M et al (2000) Arrest, adaptation, and recovery following a chromosome double-strand break in *Saccharomyces cerevisiae*. *Cold Spring Harb Symp Quant Biol* 65: 303–314
- Levine TP, Munro S (2002) Targeting of Golgi-specific pleckstrin homology domains involves both PtdIns 4-kinase-dependent and -independent components. *Curr Biol* 12: 695–704
- Lisby M, Rothstein R, Mortensen UH (2001) Rad52 forms DNA repair and recombination centers during S phase. *Proc Natl Acad Sci USA* 98: 8276–8282
- Lisby M, Barlow JH, Burgess RC, Rothstein R (2004) Choreography of the DNA damage response: spatiotemporal relationships among checkpoint and repair proteins. *Cell* 118: 699–713
- Lord SJ, Velle KB, Dyche Mullins R, Fritz-Laylin LK (2020) SuperPlots: communicating reproducibility and variability in cell biology. *J Cell Biol* 219: e202001064
- Lundin C, North M, Erixon K, Walters K, Jenssen D, Goldman ASH, Helleday T (2005) Methyl methanesulfonate (MMS) produces heat-labile DNA damage but no detectable in vivo DNA double-strand breaks. *Nucleic Acids Res* 33: 3799–3811
- Luo J, Yang H, Song BL (2020) Mechanisms and regulation of cholesterol homeostasis. *Nat Rev Mol Cell Biol* 21: 225–245
- Mesmin B, Antony B (2016) The counterflow transport of sterols and PI4P. *Biochim Biophys Acta – Mol Cell Biol Lipids* 1861: 940–951
- Mesmin B, Bigay J, Polidori J, Jamecna D, Lacas-Gervais S, Antony B (2017) Sterol transfer, PI 4P consumption, and control of membrane lipid order by endogenous OSBP. *EMBO J* 36: 3156–3174
- Moriel-Carretero M (2021) The many faces of lipids in genome stability (and how to unmask them). *Int J Mol Sci* 22: 12930
- Moriel-Carretero M, Aguilera A (2010) A Postincision-deficient TFIIF causes replication fork breakage and uncovers alternative Rad51- or Pol32-mediated restart mechanisms. *Mol Cell* 37: 690–701
- Mukherjee B, Tomimatsu N, Burma S (2015) Immunofluorescence-based methods to monitor DNA end resection. In *Stress responses: methods and protocols*, Osowski CM (ed), pp 67–75. New York, NY: Springer
- Müllner H, Deutsch G, Leitner E, Ingolic E, Daum G (2005) YEH2/YLR020c encodes a novel sterol ester hydrolase of the yeast *Saccharomyces cerevisiae*. *J Biol Chem* 280: 13321–13328
- Nakajima S, Gotoh M, Fukasawa K, Murakami-Murofushi K, Kunugi H (2019) Oleic acid is a potent inducer for lipid droplet accumulation through its esterification to glycerol by diacylglycerol acyltransferase in primary cortical astrocytes. *Brain Res* 1725: 146484
- Panier S, Durocher D (2013) Push back to respond better: regulatory inhibition of the DNA double-strand break response. *Nat Rev Mol Cell Biol* 14: 661–672
- Pascual G, Augustinova A, Mejetta S, Martín M, Castellanos A, Attolini CS-O, Berenguer A, Prats N, Toll A, Hueto JA et al (2017) Targeting metastasis-initiating cells through the fatty acid receptor CD36. *Nature* 541: 41–45
- Paull TT, Lee JH (2005) The Mre11/Rad50/Nbs1 complex and its role as a DNA double-strand break sensor for ATM. *Cell Cycle* 4: 737–740
- Payne F, Colnaghi R, Rocha N, Seth A, Harris J, Carpenter G, Bottomley WE, Wheeler E, Wong S, Saudek V et al (2014) Hypomorphism in human NSMCE2 linked to primordial dwarfism and insulin resistance. *J Clin Invest* 124: 4028–4038
- Pelliccioli A, Lee SE, Lucca C, Foiani M, Haber JE (2001) Regulation of *Saccharomyces* Rad53 checkpoint kinase during adaptation from DNA damage-induced G2/M arrest. *Mol Cell* 7: 293–300
- Péresse T, Kovacs D, Subra M, Bigay J, Tsai MC, Polidori J, Gautier R, Desrat S, Fleuriot L, Debayle D et al (2020) Molecular and cellular dissection of the oxysterol-binding protein cycle through a fluorescent inhibitor. *J Biol Chem* 295: 4277–4288
- Qiu B, Ackerman D, Sanchez DJ, Li B, Ochocki JD, Grazioli A, Bobrovnikova-Marjon E, Diehl JA, Keith B, Simon MC (2015) HIF2 α -dependent lipid storage promotes endoplasmic reticulum homeostasis in clear-cell renal cell carcinoma. *Cancer Discov* 5: 652–667
- Ramonatxo A, Moriel-Carretero M (2021) Microscopy analysis of the smallest subunit of the RPA complex, Rfa3p, prompts consideration of how RPA subunits gather at single-stranded DNA sites. *MicroPubl Biol* 2021: <https://doi.org/10.17912/micropub.biology.000493>

- Rana RA, Cataldi A, Di PR, Mazzotti G, Centurione L, Robuffo I, Vitale M, Miscia S (1994) Evidence for an early and transient involvement of nuclear inositol lipids in subcellular signalling events related to DNA repair processes. *Cell Signal* 6: 475–480
- Reaper PM, Griffiths MR, Long JM, Charrier JD, MacCormick S, Charlton PA, Golec JMC, Pollard JR (2011) Selective killing of ATM- or p53-deficient cancer cells through inhibition of ATR. *Nat Chem Biol* 7: 428–430
- Röhrig F, Schulze A (2016) The multifaceted roles of fatty acid synthesis in cancer. *Nat Rev Cancer* 16: 732–749
- Rohwedder A, Zhang Q, Rudge SA, Wakelam MJO (2014) Lipid droplet formation in response to oleic acid in Huh-7 cells is mediated by the fatty acid receptor FFAR4. *J Cell Sci* 127: 3104–3115
- Santiago-Tirado FH, Bretscher A (2011) Membrane-trafficking sorting hubs: cooperation between PI4P and small GTPases at the trans-Golgi network. *Trends Cell Biol* 21: 515–525
- Sarkans U, Gostev M, Athar A, Behrangi E, Melnichuk O, Ali A, Minguet J, Rada JC, Snow C, Tikhonov A et al (2018) The BioStudies database—one stop shop for all data supporting a life sciences study. *Nucleic Acids Res* 46: D1266–D1270
- Shi L, Tan X, Liu X, Yu J, Bota-rabassedas N, Niu Y, Luo J, Xi Y (2021) Addiction to Golgi-resident PI4P synthesis in chromosome 1q21.3–amplified lung adenocarcinoma cells. *Proc Natl Acad Sci USA* 118: e2023537118
- Shpilka T, Welter E, Borovsky N, Amar N, Mari M, Reggiori F, Elazar Z (2015) Lipid droplets and their component triglycerides and steryl esters regulate autophagosome biogenesis. *EMBO J* 34: 2117–2131
- Sordet O, Redon CE, Guirouilh-Barbat J, Smith S, Solier S, Douarre C, Conti C, Nakamura AJ, Das BB, Nicolas E et al (2009) Ataxia telangiectasia mutated activation by transcription- and topoisomerase I-induced DNA double-strand breaks. *EMBO Rep* 10: 887–893
- Teixeira MT, Arneric M, Sperisen P, Lingner J (2004) Telomere length homeostasis is achieved via a switch between telomerase- extendible and -nonextendible states. *Cell* 117: 323–335
- Tomashevski A, Webster DR, Grammas P, Gorospe M, Kruman II (2010) Cyclin-C-dependent cell-cycle entry is required for activation of non-homologous end joining DNA repair in postmitotic neurons. *Cell Death Differ* 17: 1189–1198
- Von Filseck JM, Čopić A, Delfosse V, Vanni S, Jackson CL, Bourguet W, Drin G (2015) Phosphatidylserine transport by ORP/Osh proteins is driven by phosphatidylinositol 4-phosphate. *Science* 349: 432–436
- Wang Y-H, Sheetz MP (2022) When PIP2 meets p53: nuclear phosphoinositide signaling in the DNA damage response. *Front Cell Dev Biol* 10: 903994
- Wang YH, Hariharan A, Bastianello G, Toyama Y, Shivashankar GV, Foiani M, Sheetz MP (2017) DNA damage causes rapid accumulation of phosphoinositides for ATR signaling. *Nat Commun* 8: 2118
- Wang Y-H, Ho TLF, Hariharan A, Goh HC, Wong YL, Verkaik NS, Lee MY, Tam WL, van Gent DC, Venkitaraman AR et al (2022) Rapid recruitment of p53 to DNA damage sites directs DNA repair choice and integrity. *Proc Natl Acad Sci USA* 119: e2113233119
- Weinert TA, Hartwell LH (1988) The RAD9 gene controls the cell cycle response to DNA damage in *Saccharomyces cerevisiae*. *Science* 241: 317–322
- Yang Y, Geldmacher DS, Herrup K (2001) DNA replication precedes neuronal cell death in Alzheimer's disease. *J Neurosci* 21: 2661–2668
- Yue S, Li J, Lee SY, Lee HJ, Shao T, Song B, Cheng L, Masterson TA, Liu X, Ratliff TL et al (2014) Cholesteryl ester accumulation induced by PTEN loss and PI3K/AKT activation underlies human prostate cancer aggressiveness. *Cell Metab* 19: 393–406
- Zeng L, Wu GZ, Goh KJ, Lee YM, Ng CC, You AB, Wang J, Jia D, Hao A, Yu Q et al (2008) Saturated fatty acids modulate cell response to DNA damage: implication for their role in tumorigenesis. *PLoS One* 3: e2329
- Zhang Y, Liu Y, Duan J, Wang H, Zhang Y, Qiao K, Wang J (2019) Cholesterol depletion sensitizes gallbladder cancer to cisplatin by impairing DNA damage response. *Cell Cycle* 18: 3337–3350
- Ziv Y, Bielopolski D, Galanty Y, Lukas C, Taya Y, Schultz DC, Lukas J, Bekker-Jensen S, Bartek J, Shiloh Y (2006) Chromatin relaxation in response to DNA double-strand breaks is modulated by a novel ATM- and KAP-1 dependent pathway. *Nat Cell Biol* 8: 870–876



License: This is an open access article under the terms of the [Creative Commons Attribution-NonCommercial-NoDerivs](https://creativecommons.org/licenses/by-nc-nd/4.0/) License, which permits use and distribution in any medium, provided the original work is properly cited, the use is non-commercial and no modifications or adaptations are made.

Expanded View Figures

Figure EV1. Additional effects of inhibiting sterol esterification (related to Fig 2).

- A Identical experiment as that reported in Fig 2B but in response to 20 mM hydroxyurea (HU). Western blot is shown on the left, cytometry profiles at the same time points on the right.
- B Nonconfluent RPE-1 and Huh-7 human cell lines were either left untreated, or treated during 2 h with zeocin (10 $\mu\text{g/ml}$), prior to what cells were preloaded with oleate (4 h at 60 μM) to inhibit sterol esterification or treated with 30 μM BSA (mock) as a control. The downstream effector kinase of the DDR CHK1 was monitored by western blot for its activation using two specific antibodies directed against its phosphorylation at Ser317 or Ser345 (P-CHK1). The western blot signal for total CHK1 is used as a loading control. The bar heights in the graph show the mean values of the P-CHK1 to CHK1 signals ratio, with individual dots correspond to values out of 3 independent experiments. The error bars indicate the associated SEM.
- C RPE-1 and Huh-7 cells were incubated with oleate (60 μM) or 30 μM BSA (mock) for 2 h, followed by the addition of zeocin (10 $\mu\text{g/ml}$) where indicated for 2 extra hours. BrdU (10 $\mu\text{g/ml}$) was added to all samples during the last 2 h of treatment. Cells were fixed and processed for BrdU detection using the BD Pharmingen™ BrdU Flow Kit (Cat. No. 552598) according to the manufacturer's instructions. DNA was stained with DAPI (20 $\mu\text{g/ml}$). Cells were analyzed by cytometry and assigned to each phase of the cell cycle (subG₁: less than 1C DNA content, G₁: 1C DNA content and BrdU–, S: BrdU+, G₂: 2C DNA content and BrdU–). Graphs show the mean and the variability of 2 independent experiments is represented by the SEM.
- D Cell viability in response to oleate (60 μM), zeocin (10 $\mu\text{g/ml}$) or combination of both treatments was assessed by crystal violet assay. 30 μM BSA (mock) was used as control for oleate incubation. Briefly, RPE-1 and Huh-7 cells were seeded in 96-well plates, one plate per time point (see [Materials and Methods](#) for more details). The indicated treatments were added at day 0 and renewed at day 3. Every 24 h, one plate was processed to read Crystal violet absorbance at 570 nm. The absorbance values are proportional to the number of cells and were normalized to day 0 to calculate the proliferation rate. Graphs show the mean and the standard deviation out of three independent experiments.

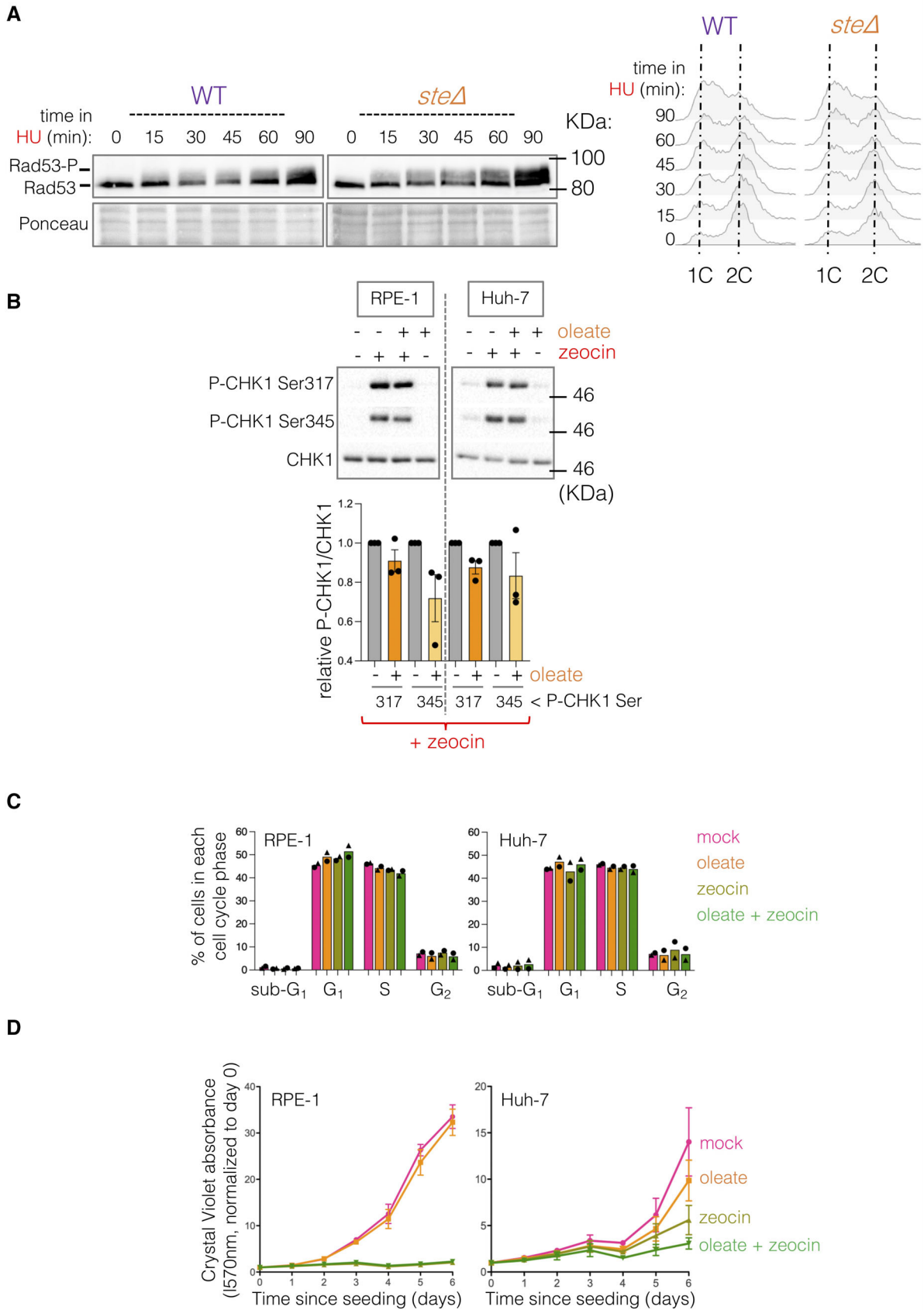


Figure EV1.

Figure EV2. Additional information related to Fig 3.

- A Cytometry profiles concerning the experiment presented in Fig 3A.
- B **Left:** identical experiment as that reported in Fig 3A but in response to 20 mM hydroxyurea (HU). **Right:** quantification of the percentage of Rad53 molecules being phosphorylated at each time point. The plotted values show 2 independent experiments.
- C Simplified scheme of the detection, signaling and repair of a DNA DSB: In response to a DSB, the MRX/MRN complex and Tel1/ATM bind the broken tips and allow the subsequent resection of 5' ends by nucleases. This leads to the formation of ssDNA that becomes coated by RPA, thus priming the recruitment of Mec1/ATR. This kinase phosphorylates on-chromatin targets, which serve to transiently limit the extent of resection, and also effector proteins, as Rad53 and CHK1-CHK2, which coordinate cell status with the need of repair. It is at this stage that Tel1/ATM acts again by triggering a transient arrest before the onset of long-range resection (Clerici et al, 2014). Eventually, Tel1/ATM disengages, which permits long-range resection. If a homologous sequence is found, productive repair by homologous recombination (HR) will follow. In the absence of a repair template, the cell can resume cycling even in the absence of repair, a phenomenon known as adaptation.
- D Exponentially growing *Saccharomyces cerevisiae* WT and *steΔ* cells were treated with 100 μg/ml zeocin and samples retrieved at the indicated time points for visualization by fluorescence microscopy. The establishment of DNA resection factories was assessed by counting the number of Rfa1-CFP foci per cell, which is plotted in this graph. The mean value of each time point is indicated by an orange bar and number. This is one illustrative experiment of the 3 that were carried out to build the graph presented in Fig 3C.
- E Percentage of cells of the indicated genotypes bearing Rad52-YFP foci at each time point after addition of 100 μg/ml zeocin. Each plotted value harbors the information referring to at least 3 independent experiments, each with at least 150 cells. The variation is indicated by the SEM. Asterisks indicate significant differences between the means of the two strains at the highlighted time points as derived from applying a t-test, where * $P < 0.05$; ** $P < 0.01$.
- F **Left** panel: (1) the double-stranded genomic DNA is represented by straight blue lines, where the restriction sites for a given restriction enzyme (RE) are indicated. (2) the addition of galactose to the cultures induces the expression of the HO nuclease, whose target site is cut. (3, 4) resection by nucleases progressively destroys RE sites in the genome. **Middle** panel: the use of a radioactive probe will reveal fragments of different sizes depending on the HO/RE/nuclease profile. **Right** panel: migration of these fragments in a denaturing electrophoresis followed by Southern blot with the indicated probe detects each resection intermediate.

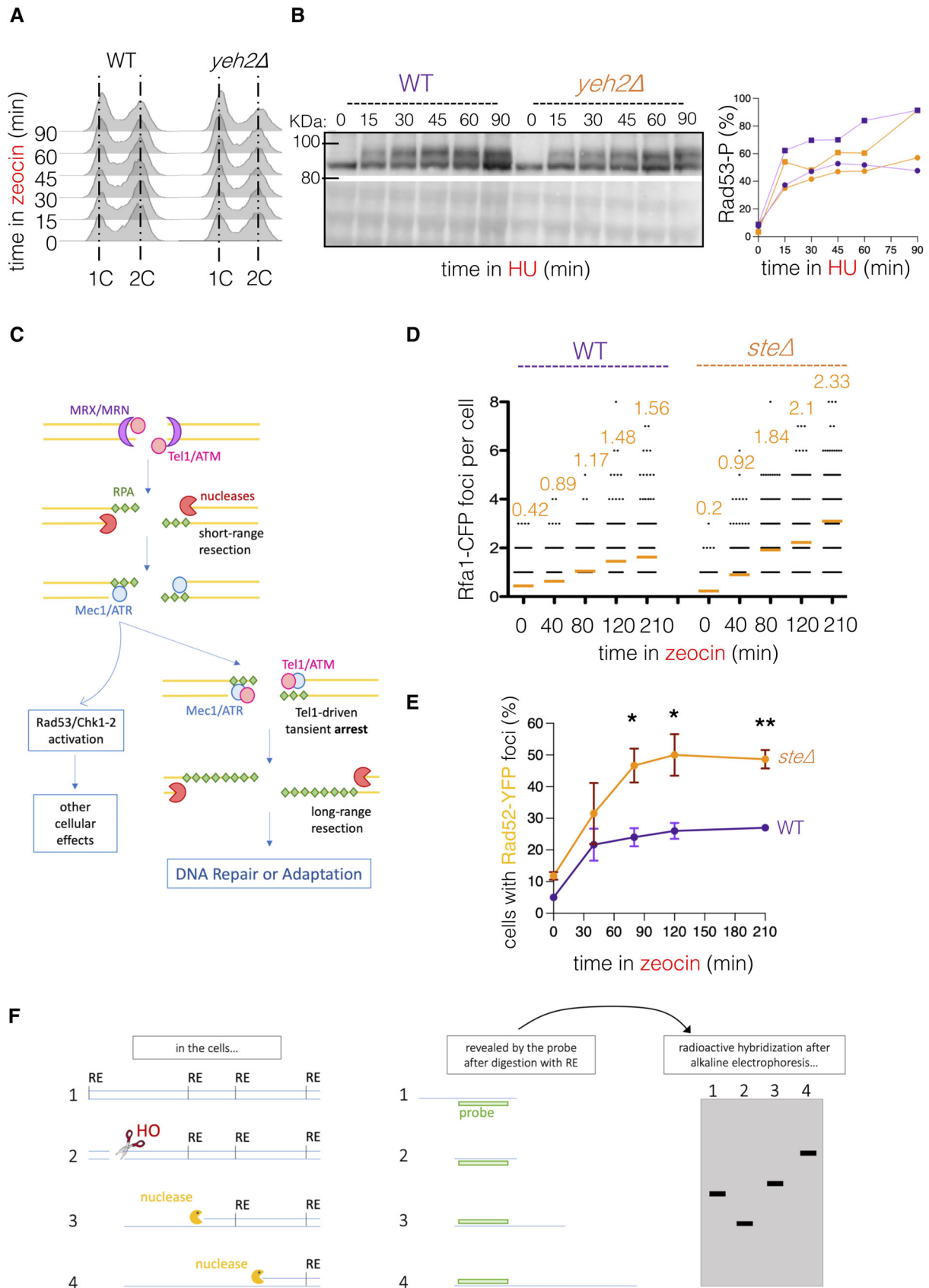


Figure EV2.

Figure EV3. Additional information related to Fig 7.

- A *Saccharomyces cerevisiae* cells transformed with a galactose-inducible FLAG-Tel1 construct were grown overnight in YPGal medium, treated for 2 h with 100 µg/ml zeocin under the assumption that this will promote the release of Tel1 from PI(4)P. FLAG-Tel1 was immunoprecipitated using M2-agarose anti-FLAG beads and retrieved by competitive elution using an excess of 3xFLAG peptide. The displayed western blot illustrates the extract preparation process. IN, input; FT, flow-through; IP, competitively eluted FLAG-Tel1; bd, Laemmli buffer + boiling-eluted remnants on the beads. One sixth of the eluted Flag-Tel1 was loaded as "IP." All the Laemmli buffer volume used to boil the beads was loaded.
- B Cells treated as in (A) were used to prepare GFP-Tel1. A sample of the total extract is loaded as the input (IN). FLAG-Tel1 was immunoprecipitated using M2-agarose anti-FLAG beads and released by boiling the beads in Laemmli buffer, the goal being to check as stringently as possible the purity of the preparation (IP). HC, heavy chain of IgG1, expected at 56 kDa; LC, light chain of IgG1, expected at 25 kDa.
- C A membrane on which 100 pmol of the indicated lipid species were spotted was incubated with immunopurified FLAG-Tel1 and further developed using an anti-FLAG antibody. The membrane shown is illustrative of one out of four independent experiments.
- D Liposome assay. Purified FLAG-Tel1 was incubated either with nothing or with liposomes containing embedded PI(4)P and washed extensively, and then remaining proteins (ideally only liposome-bound ones) were solubilized in Laemmli buffer. FT (flow-through) is a 20 µl sample from the first wash ml. The blot shows the retrieved anti-FLAG signals.
- E Western blot to detect total ATM levels (calnexin used as a loading control) for the experiments shown in Fig 7D, bottom right, in which cells were transfected with one siRNA control or three independent siRNAs against ATM, one at a time, prior to performing PLA. * indicates one unspecific band.
- F Proximity Ligation Assay of ATM and PI(4)P was combined with immunofluorescence against the trans-Golgi marker TGN46 to identify a potential co-localization of both signals. Scale bar is 10 µm.

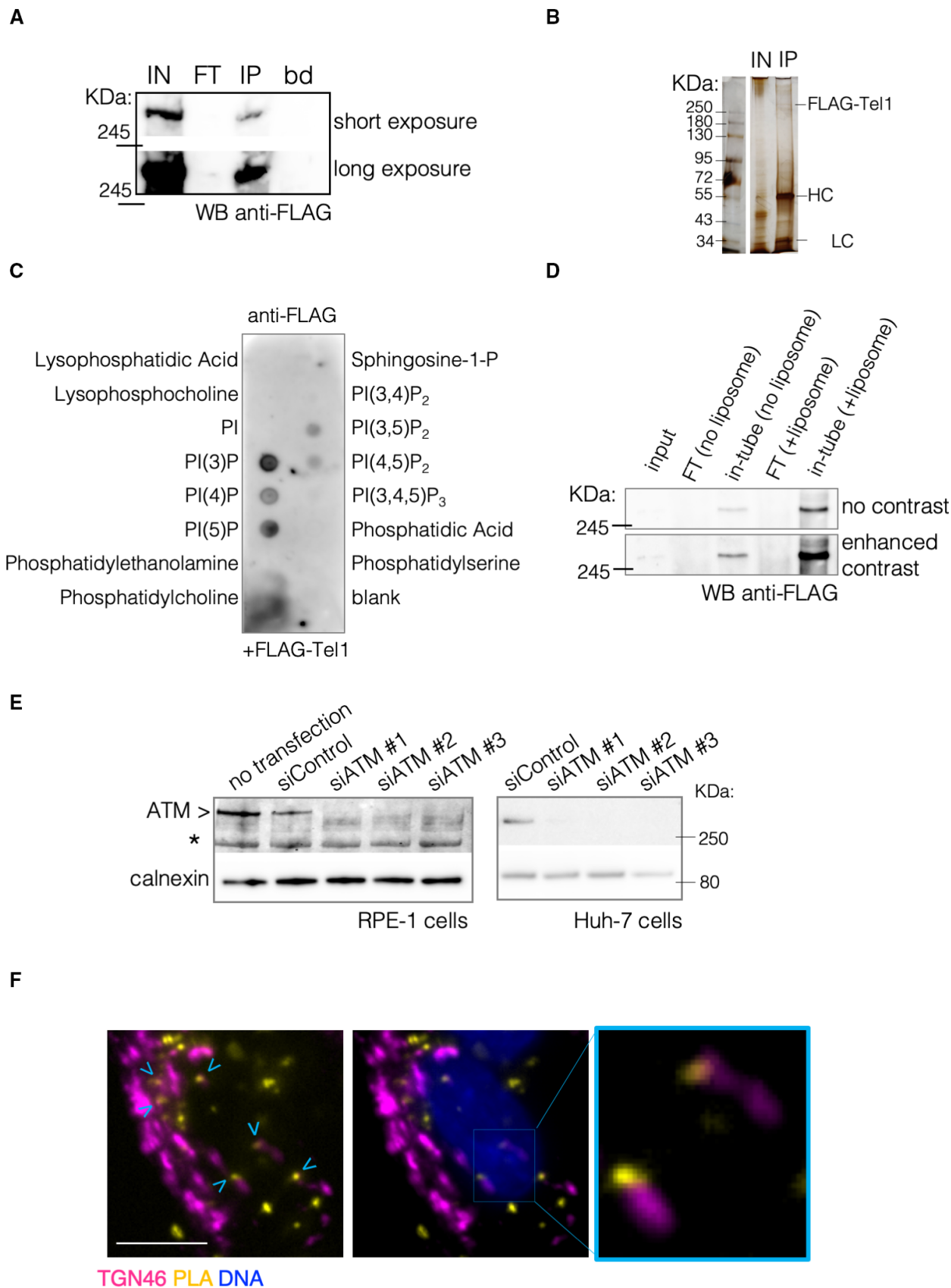


Figure EV3.

Figure EV4. Additional information for Fig 8.

- A Proximity ligation assay (PLA) to assess whether ATM and PI(4)P proximity is altered when cells are pretreated for 1 h with 500 nM of the ATM inhibitor (ATMi) AZD0156. Each point is the value of having measured all the PLA signals present in one photo (approximately 20–40 cells) and divided this value by the number of nuclei. Each independent experiment is plotted in a different color. Furthermore, the mean value of each independent experiment is highlighted by a more intense color than the individual values of that experiment, for which the color is more translucent. Last, the solid horizontal line marks the mean of the means. A one-way ANOVA for multiple comparisons was applied to evaluate whether there were significant differences between the means of the indicated conditions.
- B RPE-1 cells were transfected with a vector expressing a sensor capable of revealing PI(4)P. The sensor is composed by the domain from OSBP1 that binds PI(4)P followed by a GFP moiety (Levine & Munro, 2002). The cells were either left untreated or exposed to 0.005% MMS or to 10 µg/ml zeocin for 2 h. Upon fixation, DNA was stained using DAPI. The images shown were acquired on the GFP channel to observe PI(4)P signals. DAPI signals were used to draw the nuclei contour and impose it on the GFP ones (red dashed lines). The cell boundaries were revealed by forcing the contrast and underlined using blue dashed lines. Extended PI(4)P signals are indicated by pink arrowheads, while compact PI(4)P signals are marked by yellow ones. Scale bar is 15 µm. The graph on the right in which the percentage of cells displaying PI(4)P signals is quantified for three independent experiments. The median value of each violin plot is shown by a dashed red line.
- C **Left:** mCherry-Pus1 GFP-Tel1 *sac1Δ* cells were exposed to 100 µg/ml zeocin for 2 h or not and imaged to establish whether Tel1-associated signals emanated from the nucleus and/or the cytoplasm. Examples of cytoplasmic signals are highlighted by yellow arrowheads. Scale bar is 5 µm. **Right:** the percentage of cells displaying cytoplasmic GFP-Tel1 signals is plotted at each time point since zeocin addition in both WT and *sac1Δ* cells. Each value represents the mean percentage out of 3 independent experiments, and the error bars represent the SEM.
- D Example of an experiment as the one shown in Fig 9A that also includes the detection of total ATM. As observed, the overall stability of the protein also seems to be impacted by the treatments. This is why calnexin is used as a referent for the load.

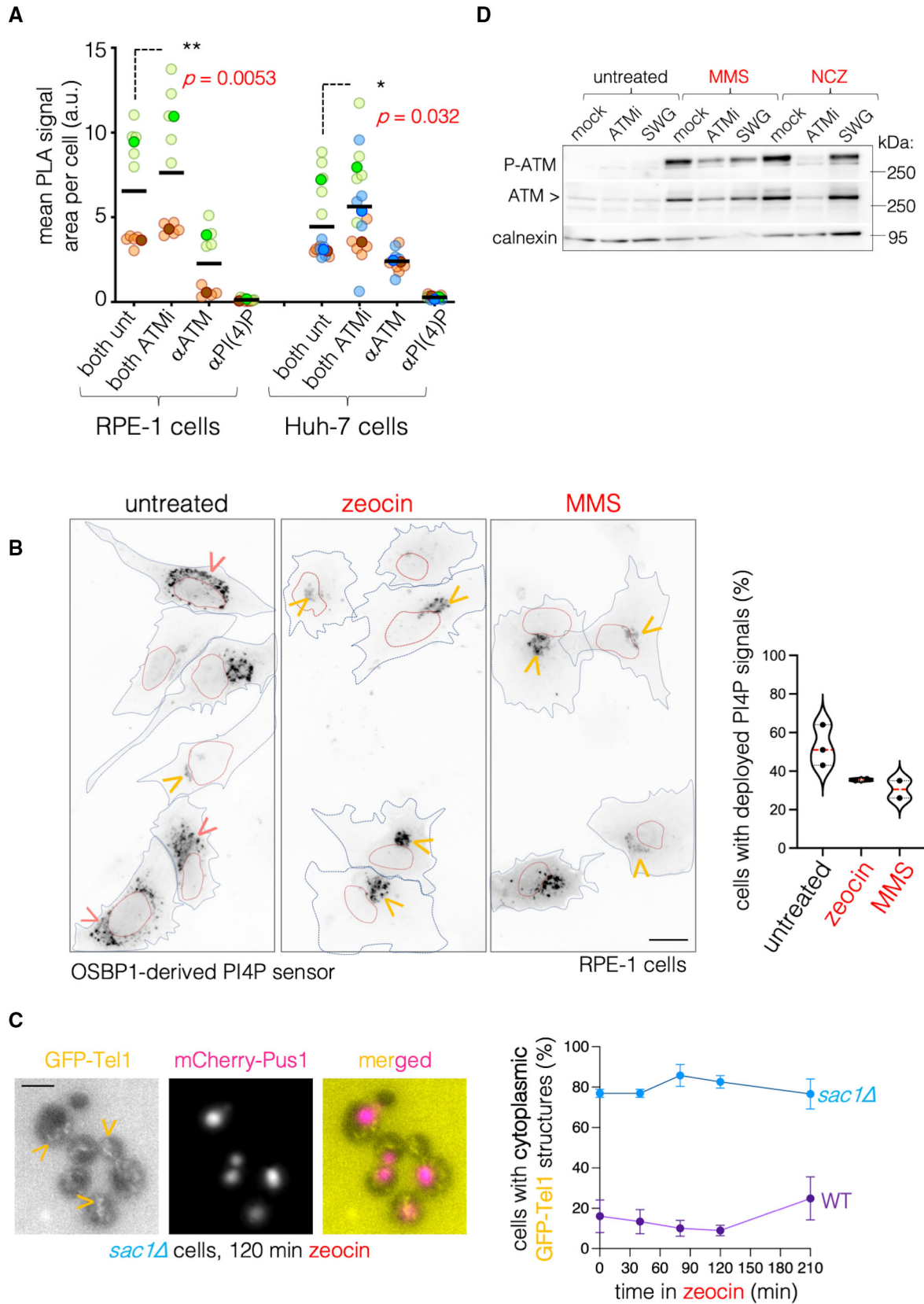


Figure EV4.

Appendix

“A Sterol-PI(4)P exchanger modulates the Tel1/ATM axis of the DNA Damage Response”

by Sara Ovejero*, Sylvain Kumanski*, Caroline Soulet, Julie Azarli, Benjamin Pardo,
Olivier Santt, Angelos Constantinou, Philippe Pasero and María Moriel-Carretero
(* equal contribution)

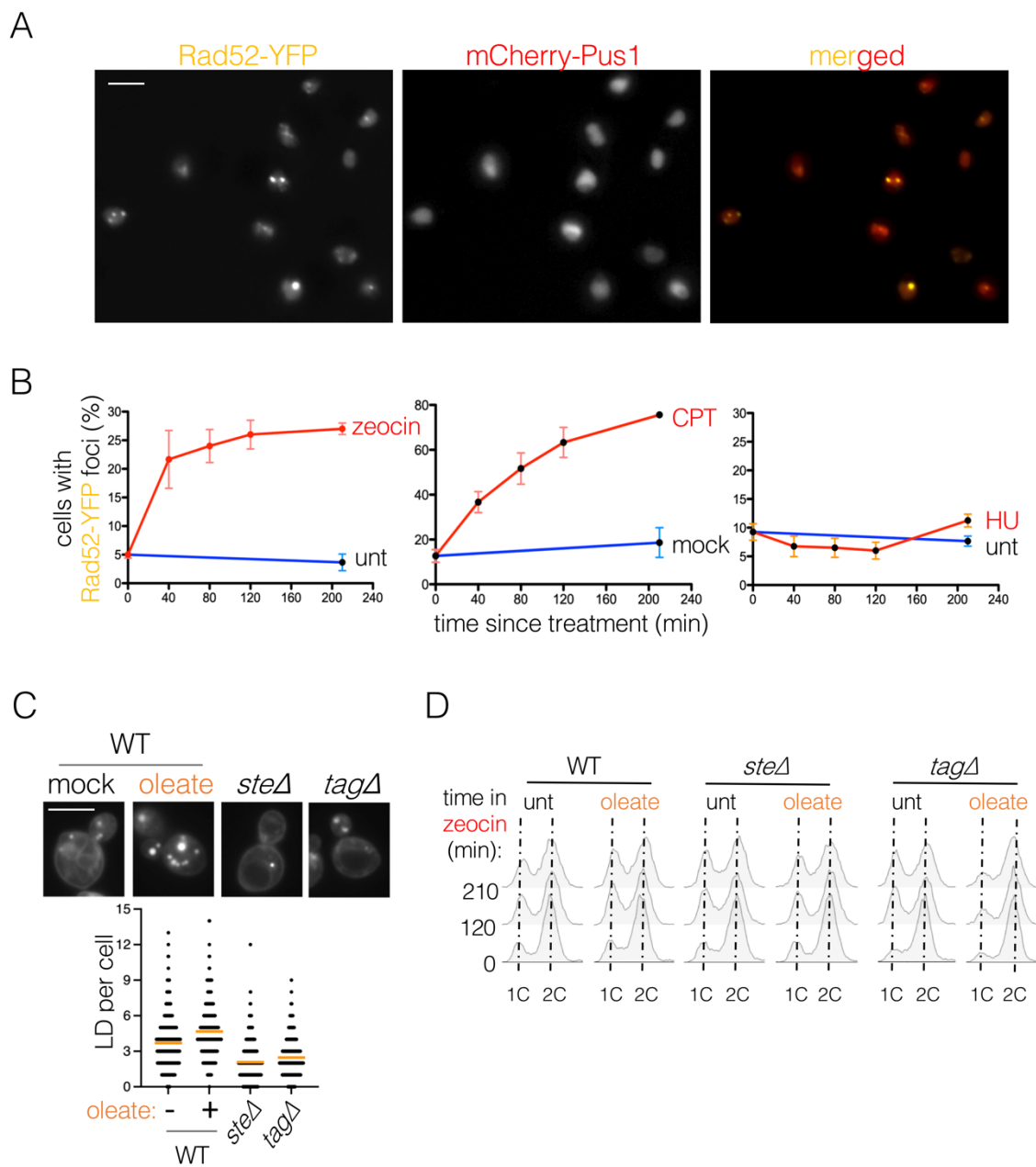
Table of contents:

Appendix Figure S1. Controls for Fig 1 and 2, pages 2-3

Appendix Figure S2. Additional controls for Fig 2, pages 4-5

Appendix Table S1. Strains used in this study, pages 6-7

Appendix Table S2. Plasmids used in this study, page 8



Appendix Fig S1

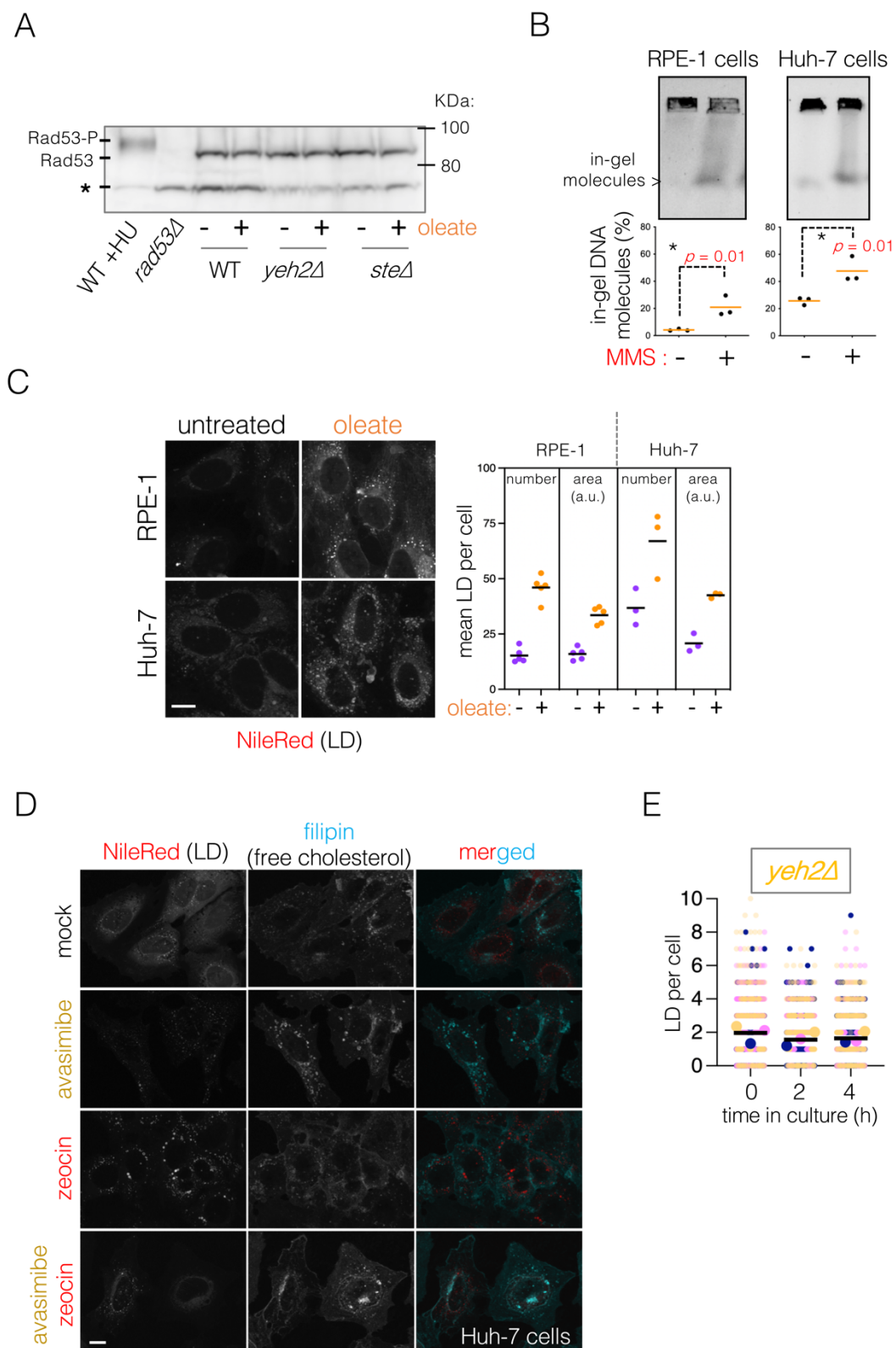
Appendix Fig S1. Controls for Fig 1 and 2

A. Representative image to illustrate the Rad52 foci (Rad52-YFP panel) in *S. cerevisiae* cells that were exposed to 100 µg/mL zeocin. mCherry-tagged Pus1 was used as a tool to precisely define the nucleus throughout all the experiments presented in panel 1B. Scale bar is 4 µm.

B. The percentage of cells bearing Rad52-YFP foci at each time point of the experiments described in Fig 1A-D was inspected visually. Each plotted value harbours the information referring to at least 3 independent experiments, each with at least 150 cells. The variation is indicated by the standard error of the mean (SEM). Red lines are used for drug-treated cultures, while blue lines are used for untreated ones.

C. Top: Nile Red staining of cells to verify that the *steΔ* and *tagΔ* strains bear less LD and of decreased intensity, as reported ⁷⁶, and that WT cells had indeed incorporated the provided oleate from the culture medium and stored it in the shape of LD. At least 150 cells were counted per condition. Scale bar is 5 µm. **Bottom:** Quantification of number of LD per cell in the same conditions.

D. Cytometry profiles concerning the experiment presented in Fig 2B,C.



Appendix Fig S2

Appendix Fig S2. Additional controls for Fig 2

A. Western blot of the indicated strains either in basal conditions, after 2 h pre-loading with 0.05% oleate, or with 100 mM HU. Rad53 and Rad53-P migration positions are indicated by lines. The asterisk denotes an unspecific band that can be used as a reference for total load control.

B. Pulsed Field Gel Electrophoresis (PFGE) performed on DNA samples prepared from RPE-1 or Huh-7 cells that had been treated (or not) with 0.005% MMS for 2 hours to evaluate whether this agent creates DSBs in these cells. Intact DNA molecules are retained in the well, while broken ones migrate into the gel (indicated as “in-gel molecules”). The bottom graphs provide the percentage of broken molecules per lane (with respect to all molecules in a given lane). Plugs were prepared at 37°C to prevent artefactual breaking of DNA molecules⁷⁷. Three independent experiments are plotted, and their mean value is indicated by an orange bar. The statistical significance upon a *t*-test is indicated by the *p*-value.

C. Left: Representative images of fixed Huh-7 and RPE-1 cells dyed with Nile Red during the systematic verification of the experiments presented in Fig 2D, to ensure that the cells had incorporated the provided oleate from the culture medium and stored it in the shape of LD. Scale bar is 10 μm. **Right:** quantification of the mean number or mean area of LD per cell out of multiple independent experiments (individual dots).

D. Representative images of fixed Huh-7 cells dyed with Nile Red and filipin during the systematic verification prior to the experiments presented in Figure 2E to ensure that sterol esterification has been effectively prevented by avasimibe. In more detail, Nile Red dyes LD, Filipin dyes free cholesterol. Scale bar is 10 μm.

E. Superplot graph showing the quantification of the number of LD per cell displayed by the *yeh2Δ* mutant. Exponentially growing cultures were scored for this parameter at a given time 0, then 2 and 4 h later. Small dots refer to individual cells, while each of the three colours represents an independent experiment. Big dots are the mean value of each experiment.

Appendix Table S1: Strains used in this study

Name	Genotype	Simplified Genotype	Origin
MM-03	<i>W303, MAT α, RAD52-YFP, RFA1-CFP, mCherry-PUS1::URA3</i>	Rad52-YFP Rfa1-CFP mCherry-Pus1	Benjamin Pardo
MM-67	<i>W303, MAT α, are1ΔHIS3, are2ΔLEU2, RAD52-YFP, RFA1-CFP, mCherry-PUS1::URA3</i>	<i>steΔ</i> mCherry-Pus1 Rad52-YFP Rfa1-CFP	This study
MM-55	<i>BY4741, MAT α, his3Δ1, leu2Δ0, met15Δ0, ura3Δ0</i>	WT BY	EUROSCARF
MM-179	<i>BY4741, MAT α, his3Δ1, leu2Δ0, met15Δ0, ura3Δ0, sac1ΔkanMX</i>	<i>sac1Δ</i>	EUROSCARF, CBY1730, Christopher Beh
MM-186	<i>BY4741, MAT α, his3Δ1, leu2Δ0, met15Δ0, ura3Δ0, sac1ΔkanMX GFP-TEL1</i>	<i>sac1Δ</i> GFP-Tel1	This study
MM-56	<i>BY4741, MAT α, his3Δ1, leu2Δ0, met15Δ0, ura3Δ0, yeh2ΔKAN^R</i>	<i>yeh2Δ</i>	Zvulum Elazar
SCY62	<i>MATα, ade2, can1-100, his3-11,15, leu2-3,112, trp1-1, ura3-1</i>	WT	Zvulun Elazar
H1226	<i>MAT α, ade2, can1-100, met, his3, ura3, leu2, dga1Δ::KAN^R, lro1Δ::TRP1</i>	<i>tagΔ</i>	Zvulun Elazar
H1112	<i>MAT α, ade2, can1-100, ura3-1, trp1, are1Δ::HIS3, are2Δ::LEU2</i>	<i>steΔ</i>	Zvulun Elazar
A3Y3A	<i>MAT α, his3D200, ade2, ura3, leu2k::ADE2-URA3::leu2k</i>	WT LAUL	Andrés Aguilera
MM-13	<i>W303, MAT α, RAD5?, BAR1?, are1ΔHIS3, are2ΔLEU2, leu2k::ADE2-URA3::leu2k</i>	<i>steΔ</i> LAUL	This study
MM-23	<i>W303, MAT α, RAD5?, are1ΔHIS3, are2ΔLEU2, rad3-102::HYGR, leu2k::ADE2-URA3::leu2k</i>	<i>steΔ</i> <i>rad3-102</i> LAUL	This study

MM-35	<i>W303, MAT α, RAD5, ade2, can1-100, his3-11,15, leu2-3,112, trp1-1, ura3-1</i>	WT (W303, RAD5)	PP870 (Philippe Pasero)
YREC57-44	<i>W303, MAT α, RAD5, rad3-102::HYG^R</i>	<i>rad3-102</i>	Andrés Aguilera (Moriel-Carretero & Aguilera, 2010)
MM-40	<i>W303, MAT α, WT, RAD5, mCherry-PUS1::URA3, yEGFP-TEL1</i>	mCherry-Pus1 yGFP-Tel1	This laboratory (Coiffard et al, 2021)
MM-61	<i>MAT α, his3, leu2, yeh2ΔKAN^R, mCherry-PUS1:: URA3, yGFP-TEL1</i>	<i>yeh2Δ</i> mCherry-Pus1 GFP-Tel1	This study
MM-51	<i>W303, MAT α, are1ΔHIS3, are2ΔLEU2, mCherry-PUS1::URA3, yGFP-TEL1</i>	<i>steΔ</i> mCherry-Pus1 GFP-Tel1	This study
MM-38	<i>W303, MAT α, RAD5, yGFP-TEL1</i>	WT yGFP-Tel1	This laboratory (Coiffard et al, 2021)
MM-75	<i>MAT α, yeh2ΔKAN^R, yGFP-TEL1</i>	<i>yeh2Δ</i> yGFP-Tel1	This study
MM-76	<i>MAT α, are1ΔHIS3, are2ΔLEU2, yGFP-TEL1</i>	<i>steΔ</i> yGFP-Tel1	This study
MM-58	<i>W303, MAT α, ura3-52, leu2-3,112, his3-i200, trp1-1, trp1-1, lys2-801, tel1ΔKAN^R</i>	<i>tel1Δ</i>	PP1217 (Philippe Pasero)
JKM179	<i>W303, MAT α, ade1-100, leu2-3,112, lys5, trp1::G', ura3-52, hoΔ, hml1ΔADE1, hmrΔADE1, ade3::GALp-HO</i>	<i>GAL1p-HO</i>	PP648 (Philippe Pasero)(Lee et al, 2000)
MM-480	<i>W303, Mat α, WT, Rad5+, yEGFP-Tel1, mCherry-PUS1::URA3, sae2Δ::LEU2</i>	<i>sae2Δ</i> yGFP-Tel1 mCherry-Pus1	This study
PP945	<i>W303, Mat α, RAD5+, rad53ΔG418^R, sml1ΔHIS3</i>	<i>rad53Δ</i>	Philippe Pasero
MM-483	<i>Mat α, his3, leu2, yeh2ΔG418^R, mCherry-PUS1::URA3, yEGFP-Tel1, sae2Δ::LEU2</i>	<i>sae2Δ yeh2Δ</i> yGFP-Tel1	This study
MM-134	<i>Mat α, Rad5+ Gal1p-Cas9-CYct::LEU2ΔCAN1</i>	<i>GAL1p-Cas9</i>	This study

Appendix Table S2: Plasmids used in this study

Plasmid	Reference
pRS316 control for <i>OSH4</i> and for Fig 1K	Benjamin Pardo
YIplac211-mCherry-Pus1	Symeon Siniosoglou
pCB231 (pRS316- <i>OSH4</i>)	Christopher Beh (Beh & Rine, 2004)
pBGPα-CMV-GFP-PH_domain ^{OSBP1}	Matteo Bonazzi (Levine & Munro, 2002)
p-gRNA(x 59 cuts)	pMM-110, (Coiffard et al, 2021)